

**LQG/LTR Optimal Attitude Control
of Small Flexible Spacecraft Using
Free-Free Boundary Conditions**

by

Joseph M. Fulton, Major, USAF

B.S., Michigan State University, 1991

M.B.A., City University, WA, 1998

M.S., Air Force Institute of Technology, 2000

A thesis submitted to the
Faculty of the Graduate School of the
University of Colorado in partial fulfillment
of the requirements for the degree of
Doctor of Philosophy
Department of Aerospace Engineering Sciences

2006

Report Documentation Page

Form Approved
OMB No. 0704-0188

Public reporting burden for the collection of information is estimated to average 1 hour per response, including the time for reviewing instructions, searching existing data sources, gathering and maintaining the data needed, and completing and reviewing the collection of information. Send comments regarding this burden estimate or any other aspect of this collection of information, including suggestions for reducing this burden, to Washington Headquarters Services, Directorate for Information Operations and Reports, 1215 Jefferson Davis Highway, Suite 1204, Arlington VA 22202-4302. Respondents should be aware that notwithstanding any other provision of law, no person shall be subject to a penalty for failing to comply with a collection of information if it does not display a currently valid OMB control number.

1. REPORT DATE 03 AUG 2006	2. REPORT TYPE N/A	3. DATES COVERED -	
4. TITLE AND SUBTITLE LQG/LTR Optimal Attitude Control of Small Flexible Spacecraft Using Free-Free Boundary Conditions		5a. CONTRACT NUMBER	
		5b. GRANT NUMBER	
		5c. PROGRAM ELEMENT NUMBER	
6. AUTHOR(S)		5d. PROJECT NUMBER	
		5e. TASK NUMBER	
		5f. WORK UNIT NUMBER	
7. PERFORMING ORGANIZATION NAME(S) AND ADDRESS(ES) University of Colorado		8. PERFORMING ORGANIZATION REPORT NUMBER	
9. SPONSORING/MONITORING AGENCY NAME(S) AND ADDRESS(ES) AFIT/CIA		10. SPONSOR/MONITOR'S ACRONYM(S)	
		11. SPONSOR/MONITOR'S REPORT NUMBER(S)	
12. DISTRIBUTION/AVAILABILITY STATEMENT Approved for public release, distribution unlimited			
13. SUPPLEMENTARY NOTES , The original document contains color images.			
14. ABSTRACT			
15. SUBJECT TERMS			
16. SECURITY CLASSIFICATION OF:			17. LIMITATION OF ABSTRACT
a. REPORT unclassified	b. ABSTRACT unclassified	c. THIS PAGE unclassified	UU
			18. NUMBER OF PAGES 219
			19a. NAME OF RESPONSIBLE PERSON

This thesis entitled:
LQG/LTR Optimal Attitude Control
of Small Flexible Spacecraft Using
Free-Free Boundary Conditions
written by Joseph M. Fulton, Major, USAF
has been approved for the Department of Aerospace Engineering Sciences

Dr. Scott E. Palo

Dr. Donald L. Mackison

Dr. Dale A. Lawrence

Dr. James P. Avery

Dr. Scott R. Dahlke

Date _____

The views expressed in this article are those of the author and do not reflect the official policy or position of the United States Air Force, Department of Defense, or the U.S. Government.

Major, USAF, Joseph M. Fulton, (Ph.D., Astronautical Engineering)

LQG/LTR Optimal Attitude Control

of Small Flexible Spacecraft Using

Free-Free Boundary Conditions

Thesis directed by Dr. Scott E. Palo

Due to the volume and power limitations of a small satellite, careful consideration must be taken while designing an attitude control system for 3-axis stabilization. Placing redundancy in the system proves difficult and utilizing power hungry, high accuracy, active actuators is not a viable option. Thus, it is customary to find dependable, passive actuators used in conjunction with small scale active control components. This document describes the application of Elastic Memory Composite materials in the construction of a flexible spacecraft appendage, such as a gravity gradient boom. Assumed modes methods are used with Finite Element Modeling information to obtain the equations of motion for the system while assuming free-free boundary conditions. A discussion is provided to illustrate how cantilever mode shapes are not always the best assumption when modeling small flexible spacecraft. A key point of interest is first resonant modes may be needed in the system design plant in spite of these modes being greater than one order of magnitude in frequency when compared to the crossover frequency of the controller. LQG/LTR optimal control techniques are implemented to compute attitude control gains while controller robustness considerations determine appropriate reduced order controllers and which flexible modes to include in the design model. Key satellite designer concerns in the areas of computer processor sizing, material uncertainty impacts on the system model, and system performance variations resulting from appendage length modifications are addressed.

Dedication

This effort is dedicated to my parents. They taught me how to dream and to critically think my way to realizing those dreams. I would also like to dedicate this work to all those who dream of space – past, present, and future.

Contents

Chapter	
1 Introduction	1
1.1 Small Satellites	1
1.2 Gravity Gradient Stabilization	8
1.3 Elastic Memory Composites	16
1.4 Flexible Spacecraft Control	20
1.5 Problem Formulation	25
1.6 Research Importance	28
1.6.1 Innovative	28
1.6.2 Significance	29
2 Equations of Motion	32
2.1 Flexible Spacecraft Modeling	32
2.1.1 Rigid Body Dynamics	33
2.1.2 Flexible Dynamics	37
2.1.3 The Coupling Equation	40
2.2 Finite Element Model	45
2.2.1 Model Parameters	45
2.2.2 Free-Free Boundary Conditions	51
2.3 State Space Form of Nominal System Model	66

3	Attitude Control of Small Flexible Structures	72
3.1	Control Bandwidth	72
3.2	LQG/LTR	75
3.2.1	Linear Quadratic Regulator (LQR)	75
3.2.2	Optimal Estimation (Kalman Filter)	79
3.2.3	Linear Quadratic Gaussian (LQG)	80
3.2.4	Loop Transfer Recovery (LTR)	81
3.3	Reduced-Order Controllers	83
3.3.1	Controller Robustness	83
3.3.2	Pole-Zero Cancelation	88
3.4	Base-Line Response	89
4	Variation of Appendage Parameters	108
4.1	Satellite Design Concerns	108
4.2	Control Complexity	109
4.3	Material Uncertainty	118
4.4	Appendage Length	131
5	Research Summary and Recommendations	139
5.1	Research Summary	139
5.2	Future Research Recommendations	141
	Bibliography	144
	Appendix	
A	Assumed Modes Method	162
A.1	Assumed Modes Model	162

A.2	Lagrangian Equations of Motion	169
B	Gravity Gradient Stabilization	177
B.1	Gravitational Field	177
B.2	Inertial Gradient Field	180
B.3	Gravity Gradient Torque	181
B.4	Equations of Motion	183
B.5	Stability Considerations	186
C	Rotational Dynamics	189
C.1	Rotational Kinematics	189
C.1.1	Direction Cosines	189
C.1.2	Euler Angles	191
C.1.3	Quaternions	195
C.2	Rigid Body Dynamics	196
C.2.1	Kinetics	197
C.2.2	Stability	199
D	FalconSAT-3	201

Tables

Table

1.1	Mass Classification of Small Satellites	4
1.2	Attitude Control Actuator Accuracies[69]	9
2.1	Material Properties of Beryllium Copper and EMC	45
2.2	Lumped Mass Properties Used in FEM Analysis	46
2.3	Beam Properties Used in FEM Analysis	47
2.4	Cantilever Resonant Frequencies From FEM Analysis	48
2.5	Free-Free System Eigenvalues Using Unmodified HCEs	55
2.6	Free-Free Resonant Frequencies From FEM Analysis	63
2.7	Free-Free Resonant Frequencies for Nominal Model	71
3.1	Typical Disturbance Torques for LEO Small Satellites	74
3.2	Initial Values for Design Parameters	91
3.3	Final Values for Design Parameters	94
3.4	Baseline System Performance	107
4.1	Performance Comparison Between Baseline and Truth Model	118
4.2	Performance Characteristics as a Function of Material Uncertainty	121
4.3	Performance Comparison Between Full and Reduced Controller	131
4.4	Simulation Results When Only Appendage Length is Varied	133
4.5	Norm of Residuals for Appendage Length Variation	135

4.6 Simulation Results When Control Effort Limit is Maintained 136

4.7 Comparison of Design Models for the 8.2m Appendage 138

D.1 Moments of Inertia with Deployed Boom Configuration 206

Figures

Figure

1.1	Sputnik I	2
1.2	Milstar Satellite Communications System	3
1.3	Number of Small Satellites Successfully Launched	4
1.4	The Globalstar Configuration	5
1.5	Distribution of Small Satellite Users[235]	6
1.6	Program Costs for a Typical Conventional Program	6
1.7	Typical Small Satellite Program Timeline	7
1.8	Structural Drawing of UoSAT-1	10
1.9	Gravity Gradient Stabilization with a Momentum Wheel	11
1.10	Illustration of the STACER Telescopic Section Boom	13
1.11	Example of a STEM Boom [67]	13
1.12	AEC-Able Engineering's CoilAble Boom [49]	14
2.1	Rotational-Vibrational Constraint Illustration	42
2.2	First Bending Mode For Cantilever Conditions	48
2.3	Second Bending Mode For Cantilever Conditions	49
2.4	Third Bending Mode For Cantilever Conditions	49
2.5	First Torsional Mode For Cantilever Conditions	50
2.6	Cantilever Beam with Applied Point Load	51

2.7	Cantilever Beam with Applied Distributed Load	52
2.8	Three-Axis-Stabilized Geosynchronous Communications Satellite[237]	53
2.9	Example of a Symmetrical Appendage Configuration	53
2.10	Open Loop Response of Unmodified HCEs	56
2.11	Pole-Zero Map for $\frac{1}{s^2-1}$	57
2.12	Pole-Zero Map for $\frac{1}{s^2+1}$	58
2.13	First Bending Mode For Free-Free Conditions	63
2.14	Second Bending Mode For Free-Free Conditions	64
2.15	Third Bending Mode For Free-Free Conditions	64
2.16	First Torsional Mode For Free-Free Conditions	65
2.17	Nondimensionalized Resonant Transmission Forces	70
3.1	Defining Uncertainty in a Model	86
3.2	Simulink Block Diagram For Closed Loop Response	92
3.3	Control Effort with Initial Design Parameters	94
3.4	Control Effort with Final Design Parameters	95
3.5	Baseline SR Test for Initial Design Model	96
3.6	Baseline SR Test with First Bending and Torsional Modes	97
3.7	Pole-Zero Map of Each Element of the 3×3 Controller Transfer Function	98
3.8	Bode Plots of Each Element of the 3×3 Controller Transfer Function	99
3.9	Comparison of Reduced and Full Order Controller (default tol)	99
3.10	RMS of Bode Magnitude for Gc(1,1)	100
3.11	RMS of Bode Phase for Gc(1,1)	101
3.12	Comparison of Reduced and Full Order Controller (tol=1e-6)	101
3.13	Comparison of Reduced and Full Order Controller (tol=1e-5)	102
3.14	RMS of Full/Reduced Order Control Effort	103
3.15	RMS of Full/Reduced Order Dynamic Response	103

3.16	Stability Robustness Test Using Reduced Controller	104
3.17	Control Effort of Full and Reduced Order Controller	105
3.18	Dynamic Response of Full and Reduced Order Controller	105
3.19	Singular Values of Recovered Loop Transfer Matrix, $G_c G_p$	106
4.1	Smooth CPU Usage History	111
4.2	Non-Linear CPU Usage History	112
4.3	Elapsed Time vs Number of Operations	114
4.4	Implementation Costs of Various Order Design Models	115
4.5	Pole-Zero Cancellation Effects on Number of Operations	116
4.6	Dynamic Performance and Implementation Difficulty	117
4.7	Linear Fitting of Peak Control Effort Data	122
4.8	Error Bounds for Peak Control Effort Data	122
4.9	Linear Fitting of Stability Robustness Data	123
4.10	Error Bounds for Stability Robustness Data	123
4.11	Linear Fitting of Crossover Frequency Data	124
4.12	Error Bounds for Crossover Frequency Data	124
4.13	Linear Fitting of Delay Time Data	125
4.14	Error Bounds for Delay Time Data	125
4.15	Linear Fitting of Rise Time Data	126
4.16	Error Bounds for Rise Time Data	126
4.17	Linear Fitting of Settling Time Data	127
4.18	Error Bounds for Settling Time Data	127
4.19	Linear Fitting of Peak Overshoot Data	128
4.20	Error Bounds for Peak Overshoot Data	128
4.21	Full/Reduced Order Control Effort for Material Uncertainty Ratio 1.17	130

4.22 Full/Reduced Order Dynamic Response for Material Uncertainty Ratio	
1.17	130
4.23 Curve Fitting of Stability Robustness Data for Length Variation	134
4.24 LQG/LTR Design Ratio, q/r , as Appendage Length is Varied	136
4.25 SR Plot for 8.2m Appendage with 1st Bending Modes in Design Model .	137
4.26 SR Plot for 8.2m Appendage with 2nd Bending Modes in Design Model	137
A.1 Flexible Satellite Dynamic Model	162
A.2 Illustration of Spacecraft Yaw Producing Torsional Torque	168
A.3 Displacement of the Flexible Appendage	170
B.1 Gravity Gradient Torques on a Near-Earth Satellite[240]	178
B.2 Gravity Gradient Spacecraft Stability Regions	188
C.1 Classical Euler rotations of a rigid body [44]	191
C.2 Sequential orthogonal rotations of the \hat{e} reference frame about the \hat{E} reference frame [44]	192
D.1 A Solid Model Drawing of FalconSAT-3	202
D.2 3-Axis MPACS Cluster	204
D.3 Four MPACS Clusters on the Nadir Plate of FalconSAT-3	205
D.4 A 2-Axis MPACS Cluster Attached to the EMC Boom	205

Chapter 1

Introduction

1.1 Small Satellites

The world entered a new stage in its technological advancement on October 4th, 1957. On this day, Russians launched the first man made satellite into orbit. Sputnik was shaped like a basketball with a diameter of 2 meters and weighed only 84 kg (see Figure 1.1). A month later, Sputnik II, weighing a total of 511 kg, placed a dog named Laika in an orbit about the Earth. The mission was declared a failure when the satellite experienced difficulty separating from its booster and overheated[123]. Seventeen months after the launch of Sputnik I, the United States launched Explorer 1. This light satellite, weighing only 14 kg, measured charged particles in the upper atmosphere and discovered the Van Allen radiation belts[5].

These satellites were small for two reasons. First, the launch capability of existing rockets had only been evolving for a few decades prior to the launch of Sputnik. In fact, American scientists were surprised with how well the Russians could put heavy payloads (1,500 kg) into orbit[186]. Program risk is the other reason for the use of small satellites. The first launch attempt by the United States failed on December 6, 1957 when a Navy Vanguard rocket exploded before leaving the launch pad. The failure may have been catastrophic to the American's race for space had they dedicated a majority of their program funds to launching a larger version of Explorer 1.

Since the end of the 1950s, satellites have grown in mass and expense as larger

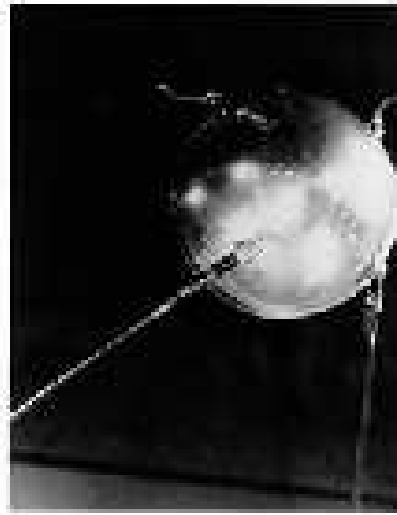


Figure 1.1: Sputnik I

missions were attempted. Businesses emerged to take advantage of the remote sensing and communication capabilities orbiting satellites offered. These businesses could offset the added risk of launching larger satellites by adding advanced instruments capable of producing better results than cheaper, smaller scale versions of the payloads. However, advanced instruments consume additional power and the battery and solar array mass increased accordingly. Primary structures, which carry most of the loads of the satellite, also grew in mass and complexity to support the additional components. The Milstar Satellite Communications System (shown in Figure 1.2) is an example of a large satellite currently in use. This system provides secure, worldwide communications to high priority military users to meet essential wartime requirements. Each Lockheed Martin designed satellite weighs 4,536 kg and costs approximately \$800 million[47].

A 45 year trend in small satellites is shown in Figure 1.3. This figure illustrates the number of successful launches of small satellites with the mini, micro, and nano classifications (see Table 1.1). Data is compiled from various sources presented by Surrey Satellite Technology Ltd. (SSTL) and does not include nonfunctioning satellites (e.g. orbital debris radar calibration spheres released by the Shuttle intended to provide

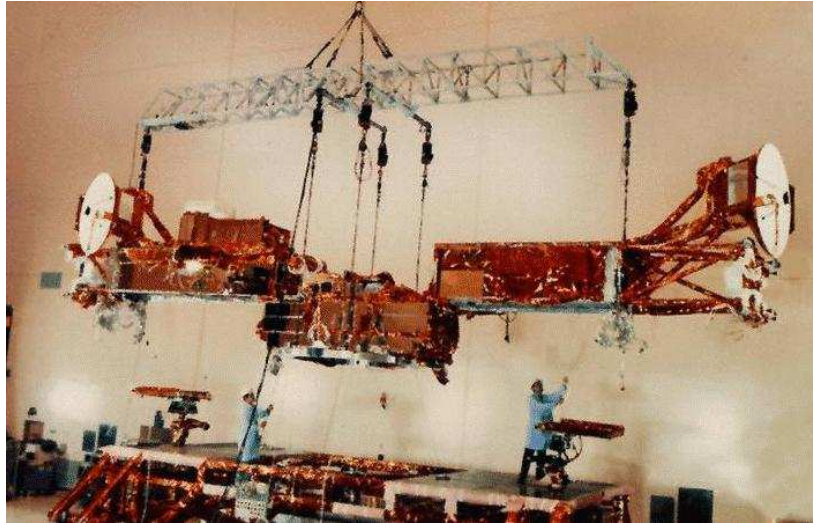


Figure 1.2: Milstar Satellite Communications System

calibration for radar echoes).

Figure 1.3 begins with two Sputnik satellites launched in 1957. The following decade comprises a combination of US and Russian satellite and launch technological advances. The decline during the 1970s results from efforts in launching heavy payloads during the Apollo era and the race to the Moon. The increase in small satellite launches during the 1980s and early 1990s stemmed from the communication industries taking advantage of the global perspective benefits space offered. The Kosmos satellites formed the Commonwealth of Independent States' (CIS) military tactical communications constellation. The Kosmos program contributed greatly to role small satellites played in the communication industry during those two decades. However, the size of communication satellites grew as companies wanted larger systems to meet increasing customer needs. The construction of massive satellites continued until several high profile failures occurred in the early 1990s. The loss of the Mars Observer and the flaw in the Hubble Space Telescope's primary mirror forced government programs to start thinking "faster, better, cheaper"[96]. The multibillion dollar failures triggered the recent boom in small satellites, such as the Globalstar constellation shown in Figure 1.4. The large increase

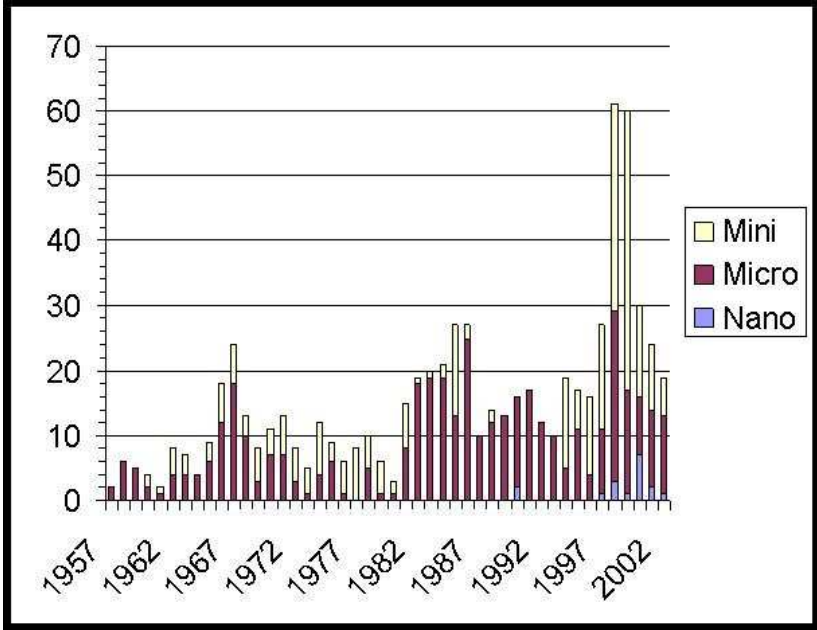


Figure 1.3: Number of Small Satellites Successfully Launched

Table 1.1: Mass Classification of Small Satellites

Classification	Wet Mass
Mini	100-500 kg
Micro	10-100 kg
Nano	1-10 kg
Pico	< 1 kg

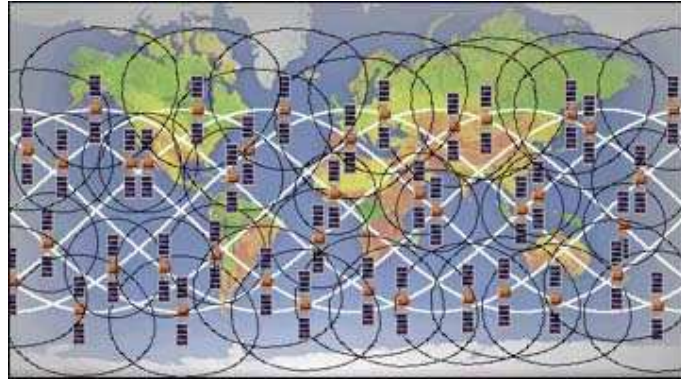


Figure 1.4: The Globalstar Configuration

in small satellite usage also reflects businesses' and universities' growing contributions to the utilization of space[135].

Today, the satellite industry is no longer exclusive to businesses and government agencies. Universities are now using satellites as educational tools and platforms for conducting advancements in research (see Figure 1.5). The decreased cost and complexity of small satellites when compared with conventional satellites are what make small satellites more appealing to academic institutions. Figure 1.6 shows how program costs for a conventional satellite add up[235]. Component selection and traceability, formal design review costs, infrastructure, and corporate overhead contribute to inflating the costs of the conventional program.

Another benefit to university programs is the reduced development timeline of small satellites. The schedule of a conventional program (3-5 years) is cumbersome in an academic environment. A two-year schedule appeals to an undergraduate institution where students complete the bulk of the advanced courses in the final two years of the degree. In addition, the two-year schedule is beneficial to graduate programs. The course work is completed in the first year and research credits are earned in the following two or three years. Figure 1.7 illustrates a typical program timeline for a small satellite with a pre-existing infrastructure, supporting faculty numbering 12, and approximately

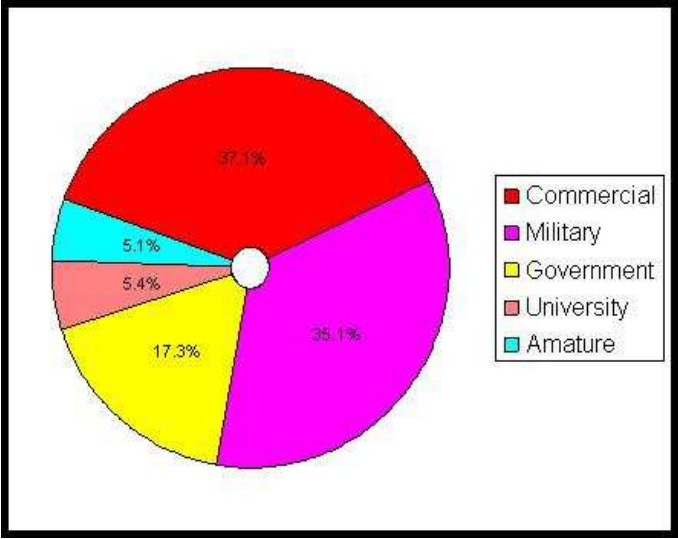


Figure 1.5: Distribution of Small Satellite Users[235]

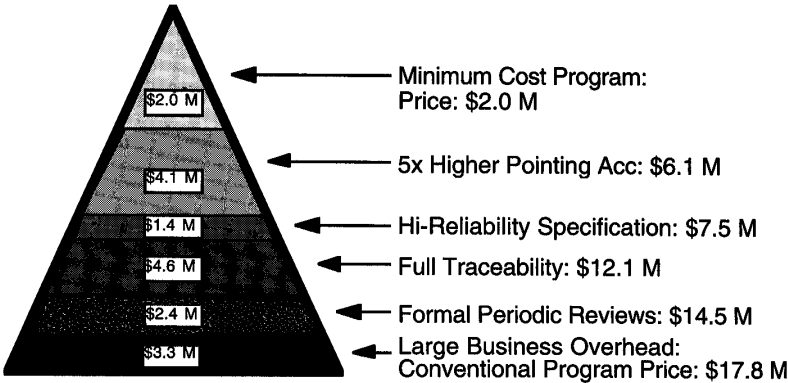


Figure 1.6: Program Costs for a Typical Conventional Program

40 students using similar designs from past successes[235].

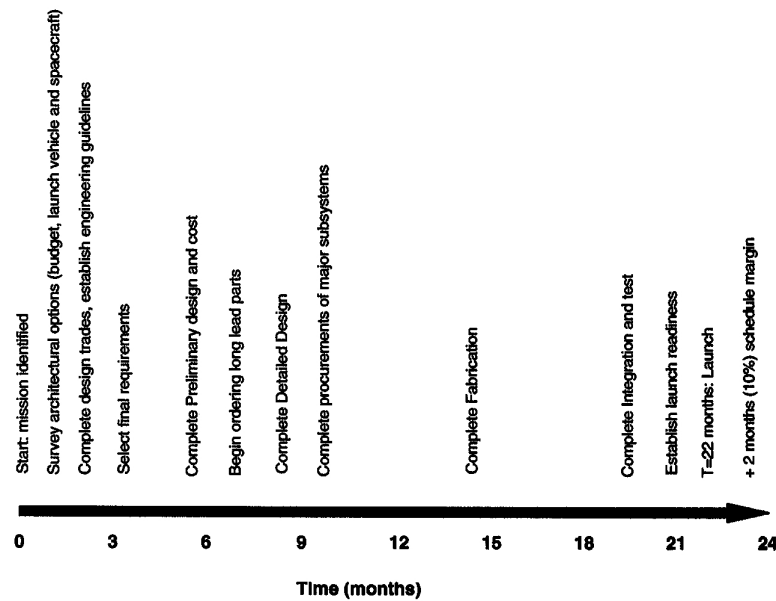


Figure 1.7: Typical Small Satellite Program Timeline

Reduced budget costs and compact schedules are not the only two aspects of small satellites which are desirable by academic institutions. Universities will assess mission failure differently than how a commercial operation will. A business will experience a loss of investment and time with each failed operation. While experiencing the same loss, albeit on a smaller scale, a university gains the practical experience of designing, building, testing, launching and operating a satellite. Experience is an effective educational tool for students. An orbital failure of a satellite still results in an academic success for students. One of the mission statements from the United States Air Force Academy's (USAFA) Department of Astronautics, located in Colorado Springs, CO, is to "teach space by doing space." Cadets that work in the Space Systems Research Center (SSRC) are engaged in each phase of a small satellite's evolution. A corporate engineer designing a similar satellite may only participate in a single phase of satellite development, such as the testing or operational phase.

Although small satellites provide the aforementioned advantages over their larger

counterparts, several disadvantages exist as well. The compactness of a small satellite limits the mass and volume of usable components. Reduced availability of space may exclude the use of more sophisticated components. Compactness may also greatly increase the acquisition costs of miniaturized devices to produce similar results. In addition, the assembly of miniature components in a confined space presents difficulties with arranging and connecting components. Smaller exterior surface area of the satellite reduces the size of solar arrays. Thus, power supplied to components is limited. Power budgets, as well as efficient power usage, are becoming increasingly important. Certain aspects of operations, such as payload functionality or attitude maneuver sequences, may become impaired if component power consumption is greater than expected. Another strong disadvantage of a small satellite is the difficulty in providing redundant systems within the satellite. While redundancy may be provided for mission critical items such as CPU memory or communication systems, it is often difficult to incorporate back up systems for attitude control of the spacecraft. If a component ceases to perform as expected, it may impair the mission or cause it to fail all together. Therefore, a small satellite must rely on systems that are not 'power hungry', do not occupy too much space, or are fairly simplistic and reliable to mitigate risk.

1.2 Gravity Gradient Stabilization

The Attitude Determination and Control Subsystem (ADCS) has traditionally been too large and expensive for use in small satellites. Key aspects of payload requirements depend upon strict pointing requirements and attitude knowledge. The payload mission may be jeopardized if the ADCS subsystem fails in meeting pointing and attitude knowledge requirements. To reduce the probability of a satellite failing its mission, redundant and sophisticated components are utilized to ensure the ADCS is not a single point of failure for the satellite. This poses a problem for small satellites requiring attitude control. In fact, a common approach with early small satellites was to provide

Table 1.2: Attitude Control Actuator Accuracies[69]

Actuator	Classification	Accuracy
Spin	Passive	$\pm 0.1^\circ$
Magnetic Rods	Passive	$\pm 5^\circ$
Gravity Gradient	Passive	$\pm 5^\circ$
Nutation Damper	Passive	$\pm 3^\circ$
Magnetic Torquers	Active	$\pm 0.1^\circ$
Thrusters	Active	$\pm 0.1^\circ$
Reaction/Momentum Wheels	Active	$\pm 0.01^\circ$
Control Moment Gyros	Active	$\pm 0.001^\circ$

no stabilization at all.

Passive stabilization techniques offered a way of providing some control while staying in compliance with the satellite's power and mass requirements. Spin, magnetic rods, and gravity gradient fall into the passive category since no energy or control actuators are required for operation (although some stored energy is required during the initial spin-up phase or deployment of the boom). These systems operate in open loop (i.e. no control feedback information is provided from attitude sensors). Once the satellite is in the desired attitude, it will exhibit typical pointing performance of $\pm 10^\circ$. Active control systems, (i.e. magnetorquers, reaction wheels, momentum wheels, thrusters), employ actuators to generate a control torque to the satellite. Active systems require attitude sensors to provide position and rate information to close the loop of the control system. By using feedback information to fine tune the control system, performance values of active control will be at least an order of magnitude smaller than passive systems. Table 1.2 lists various attitude control actuators, their classification as passive or active, and typical accuracy values.

While passive systems were used in the early prototypes of small satellites (between 1957 and 1980), active systems are seeing more use in supplementing passive

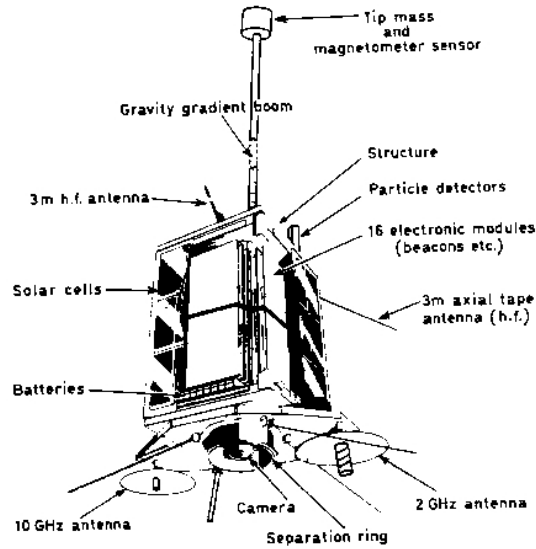


Figure 1.8: Structural Drawing of UoSAT-1

components. When a gravity gradient boom is carried, a pitch wheel can be used in momentum bias mode or a yaw wheel in zero-momentum bias. The most common control system for current small satellites is a combination of gravity gradient boom and magnetorquers. This control scheme allows the satellite to have yaw pointing control while remaining nadir pointing. The first small satellite to use this control configuration was UoSAT-1 (OSCAR-9), an amateur satellite built and operated by the University of Surrey in the early 1980s (see Figure 1.8)[218].

Gravity gradient stabilization is not a new concept. D'Alembert and Euler's celestial mechanics work in 1749 first discussed gravitational gradient effects of an axially symmetric ellipsoid in an inverse square field. 30 years later Lagrange used this information to explain the librations of the Moon[159]. Uneven mass distribution within the Moon's crust results in a gravity gradient stabilized attitude with respect to the Earth. Astronomers have observed this gravity gradient stabilized attitude for many years and have termed the unseen 50% as the 'dark side' of the Moon. Actually, due to the longitudinal, latitudinal, and diurnal components of the Moon's apparent libration, over a

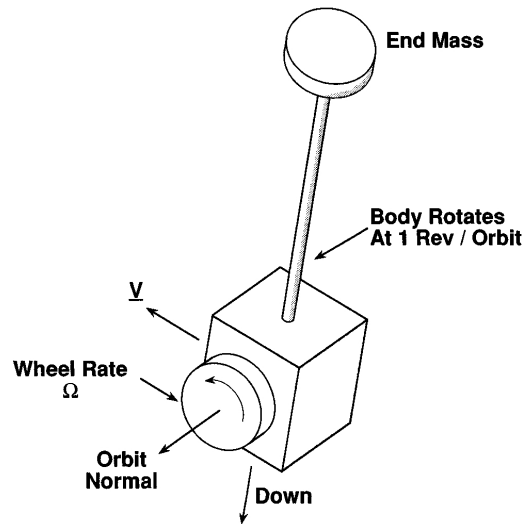


Figure 1.9: Gravity Gradient Stabilization with a Momentum Wheel

period of time an Earth based observer is able to view 59% of the Moon's surface[176].

Gravity gradient stabilization of a satellite occurs when the minimum-inertia axis locks in a vertical orientation with the orbiting body. This orientation is conventionally accomplished through the use of a deployable boom with a tip mass at the end. Once the boom is deployed, the tip mass will increase the moment of inertia in the directions transverse to the boom[240]. This boom configuration allows passive control in both the roll and pitch directions; therefore a communication or remote sensing payload may remain nadir pointing. This boom configuration does not, however, provide yaw control since the satellite is free to rotate about the vertical axis. Early research efforts illustrated how a stable orientation is created when a momentum wheel with its angular momentum is aligned along the positive orbit normal (shown in Figure 1.9)[223]. A detailed discussion of the theoretical development for gravity gradient stabilization is provided in Appendix A of this document.

Fairing limitations of launch vehicles requires the containment of boom systems prior to launch. The basic idea of deploying gravity gradient booms while in orbit

was initially developed and demonstrated in space as early as the 1960's[160]. The deployment process involves storing strain energy within a compact structure prior to fitting the satellite to the launch vehicle. Once the satellite is on-orbit, an initiation command is given by either ground based operators or an autonomous control system contained within the satellite's data handling system. This initiation command signals the gravity gradient component to release the stored strain energy which deploys the boom element to obtain its final, desired shape or configuration. Conventional boom systems use telescopic sections (shown in Figure 1.10) or furlable overlapped tubing, often referred to as Storable Tubular Extendible Member (STEM), as shown in Figure 1.11. The telescopic boom built by SSTL, known as STACER, has a heritage of over 25 years. During this time, spacecraft and sounding rockets have utilized more than 600 STACER units[135]. Small satellite designers find STACER's compact dimensions while stowed (102 x 115 x 264 mm) and lightweight design (2.2 kg without tip mass) very appealing. STACER's telescopic section is spring loaded. Deployment is initiated with dual redundant pyrotechnic bolt cutters. The "pyro-cutters", classified as "Class C" explosives, cut through a shear bolt to release the stored strain energy.

STEM booms use heat treated steel to deploy a rigidizable antenna. The boom element is fabricated to a specified length and rolled like a sleeping bag. For longer lengths, it is divided into segments that are joined by a thin lap joint. More recently, AEC-Able Engineering developed the CoilAble boom (shown in Figure 1.12). The CoilAble boom is fabricated as a helix and stored in a collapsed configuration inside the deployment canister[116]. However, STEM's tend to be heavy due to the use of either beryllium copper or stainless steel.

Although these conventional booms do have significant flight heritage, they possess several unfavorable characteristics. The high amount of stored energy in springs and the use of pyrotechnic bolt cutters generate survivability concerns for a launch vehicle. Elaborate inhibit measures need to be applied during launch to ensure an early release

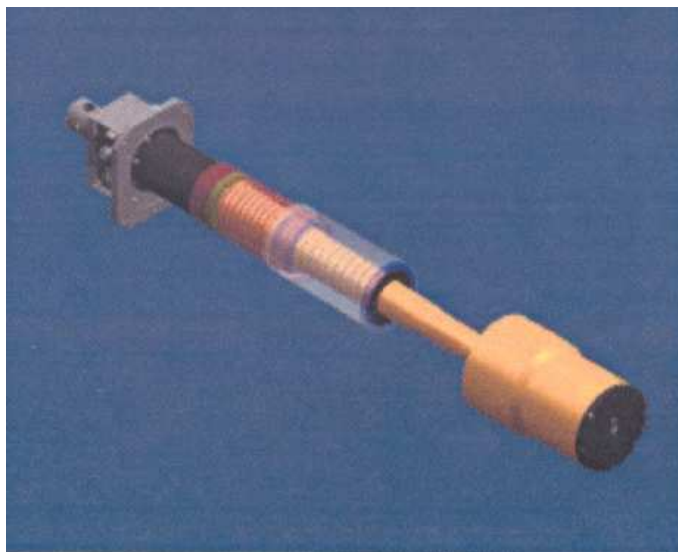


Figure 1.10: Illustration of the STACER Telescopic Section Boom

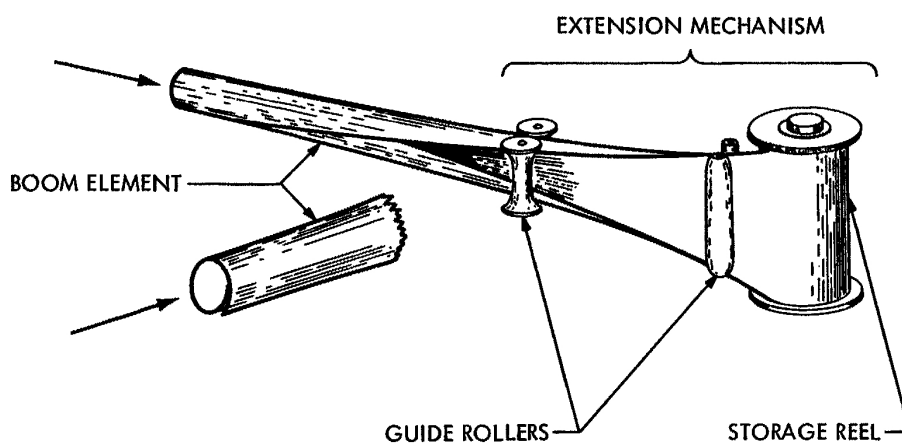


Figure 1.11: Example of a STEM Boom [67]

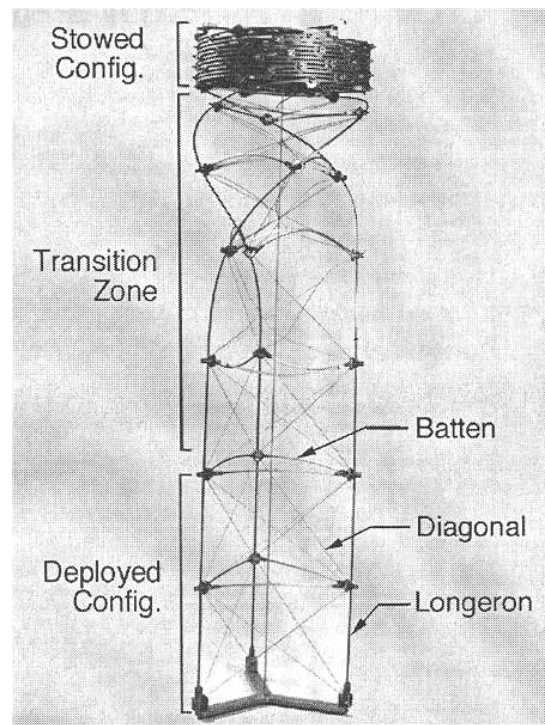


Figure 1.12: AEC-Able Engineering's CoilAble Boom [49]

does not occur. An early release could prove fatal not only to the satellite and launch vehicle, but to other satellites sharing a ride on the same launch vehicle as well. Also, human life may be at risk if the Space Shuttle is used to launch a satellite that utilizes conventional type boom deployment systems. The STACER boom design suffers from high packaged strain energy. This packaged strain energy limits the size of the boom to a maximum diameter of 2" and produces low deployed stiffness and strength[36]. In addition, pyrotechnic release devices produce high shock and contamination, are hazardous and costly to handle, and are not re-setable.

One alternative to using a traditional boom is to inflate a structure while on orbit. Deployment tests of inflatable booms have been extensively conducted during the last fifteen years. Haug and colleagues[85] utilized finite element methods to simulate the deployment process of an inflatable antenna in 1991. Six years later, Tsoi's thesis[226] used these equations to simulate the deployment of inflatable booms which were both folded and rolled up. Clem and his associates[46] conducted deployment tests in 2001 while a year later Campbell and her coworkers[35] experimentally investigated gravitational effects during the deployment of inflatable tubes. Also during 2002, Miyazaki and Uchiki[153] and Wang and Johnson[232] tested and analyzed the deployment process of inflatable structures. All of these studies focused on pressure stabilized inflatable booms where constant pressure is required to maintain the rigidity of the structures.

While the mentioned studies on inflatable structures were thorough, they only focused on the deployment dynamics with minimal consideration given to the control authority impact on the spacecraft. In addition, the use of inflatable structures were never shown to be a feasible system for small satellites. The complexity of the plumbing system for the pressurized air as well as the added mass and volume requirements for storage tanks would quickly exceed the constraints placed upon small satellites. Therefore, the support structure needed for inflatable structures would be scaled down to fit within the confines of a small satellite and greatly reduce the length of such a

structure.

1.3 Elastic Memory Composites

A recent innovation which has the potential to revolutionize the design of deployable booms is the development of shape memory materials and their introduction into the design of deployment mechanisms. Shape memory "mechanisms" can eliminate the need for traditional highly complex mechanical deployment devices, massive launch canisters, and independent deployment control systems. In addition, these shape memory mechanisms can lead to dramatically simpler boom designs that include fewer "parasitic" (i.e. non-structural) parts and are therefore much lighter in weight.

A shape-memory alloy (SMA) is a mixture of two or more metals that has the special property of being able to "memorize" a certain shape, and return to that shape even after being deformed. Usually the return to a memorized shape is triggered by heating the material. The change can happen very fast, often within seconds. The key to a SMA's ability to shape-change is that its structure differs depending on the temperature. At high temperatures, the atoms in an SMA possess a very stiff, rigid structure, called the "austenitic" structure (named after British metallurgist Sir William Chandler Roberts-Austen). The shape of an SMA is linked to its austenitic structure[225]. Any change in the shape of the metal while it is in the austenitic phase causes the structure to change, and vice versa.

As the metal cools and reaches a critical temperature range, the atoms begin to realign themselves into a different structure, called the "martensitic" structure (named after German metallurgist Adolf Martens). This structure is also linked to the austenitic structure, but is flexible and allows the metal to be visibly bent, stretched, and manipulated without changing the underlying atomic structure. When the metal is heated again to its critical temperature range, the metal transforms back into the rigid austenitic structure which, being linked to the shape of the metal, causes it to regain its original,

”memorized” or ”programmed” shape[73]. If the metal is cooled once again to the flexible martensitic phase, it will retain the memorized shape until otherwise changed by an outside influence.

The austenitic and martensitic structures that cause shape memory also possess several other exceptional properties: superelasticity, damping, and high, controllable recovery force. The superelasticity of an SMA enables the SMA to stretch more than other metals and then spring back to original size. SMAs can be stretched up to 8% more than their original length without permanently stretching or damaging the material (other metals stretch less than 1%).

Damping, another property of shape memory composites, is the ability to stop oscillations or vibrations quickly. For example, when a rubber ball is dropped onto a firm surface, it will bounce several times, but each successive bounce will get lower and lower, until eventually the ball stops bouncing. On a concrete surface the ball may bounce many times, whereas the ball might only bounce once or twice on a carpeted surface. The carpeted surface, then, would have high damping (it stops the ball quickly), and the concrete surface has lower damping. The same idea applies to damping in a mechanical system. An automotive’s engine produces numerous vibrational frequencies. The amplitude of these vibrations experienced by the occupants depends upon the damping capability of the car’s materials and structure. Since SMAs have high damping, a person sitting in an operating SMA car might not feel the engine vibrating.

A high recovery force from an SMA can be compared to the stretching or compression of a spring, such as one found in a mattress or a trampoline. When a person jumps onto a trampoline, the springs are compressed. When the springs return to their normal state, the restoring force sends the person flying into the air. Changing the shape of an SMA in its martensitic phase is like compressing the springs on a trampoline. The stored strain energy is released when the SMA returns to its memorized austenitic shape.

Other shape-memory materials also have these properties (damping, superelasticity, etc). Shape-memory polymers (SMPs) are a type of shape-memory material that is also triggered by temperature change, but is composed of plastic, instead of metal. The most familiar example of an SMP is shrink-wrap[11]. SMPs possess greater levels of superelasticity than SMAs. SMPs can stretch up to 400% more than their original length. However, SMPs produce a lower recovery force. This means SMPs are more favorable for purposes where major shape changing needs to occur while generating little resistance to the change. An example usage of SMPs which is currently being marketed is "smart" cold-weather clothing. The clothing is impermeable to wind and rain at lower temperatures but porous at higher temperatures for "breathability." Another difference between SMPs and SMAs is that SMPs can be manufactured from biodegradable materials. This is advantageous for surgical purposes. It is not necessary to remove temporary implants or sutures created from SMP materials since they will intentionally disintegrate over time[122].

The first use of SMAs occurred in various fields of engineering, especially in the military. The first SMAs were developed by the Navy. A nickel-titanium alloy was developed at the US Naval Ordnance Laboratory in 1961. The shape-memory properties were discovered accidentally. The Navy named the new substance "Nitinol" – Ni for nickel, Ti for titanium, and NOL for Naval Ordnance Lab[105]. Nitinol has been the most prominently used SMA in engineering applications.

The first application of SMAs was for pipe joining. For this purpose, the SMA is programmed into the shape of a short tube slightly smaller than the two pipes being joined. Then, in its malleable phase, the metal is stretched into a tube slightly larger than the two pipes. The SMA is set with the two pipe ends inside, and then warmed. As warming occurs, the pipes are squeezed together and secured. This method has been used quite successfully to join various types of pipes, from hydraulic pipes in F-14 fighter planes[73] and naval ships, to transport pipes in the chemical and petroleum industries.

Pipes of up to 80 inches in diameter have been joined utilizing SMAs.

Due to the controlled force exerted when an SMA regains its programmed shape, SMAs can be used in robotics to provide smooth motions. Robotics engineers in Japan have developed "devices to grasp delicate paper cups filled with water"[178]. SMAs have also been used as replacements for explosives in building demolitions. When a large force stored in an SMA is recovered in fractions of a second, the yield is comparable to an explosion. These two examples of the practical uses of SMAs demonstrate these materials' astonishing range of capabilities.

SMAs are frequently utilized in the aerospace industry. The high damping capability of SMAs provides a spacecraft insulation from vibration, a major concern during launch. In addition, SMAs can be utilized for deploying instruments and payloads once the spacecraft reaches orbit. Many tasks, from the simple uncovering of a camera lens, to the complete deployment of a solar panel, can be activated by an SMA. These actions can be programmed to trigger automatically once the alloy reaches a predetermined low temperature as it cools off in the space environment. SMAs can also be activated through heating from an electrical current. The heating process can be easily commanded from ground control at the appropriate time.

Elastic Memory Composite (EMC) materials are a relatively new addition to the family of SMAs and have been under development by Composite Technology Development, Inc. (CTD) since 1999 [227]. CTD has been able to dramatically improve both the stiffness and the recovery force of a shape memory polymer by incorporating it into a fiber-reinforced composite[125]. This results in substantially lower densities and higher elastic strain capacities. A specific thermo-mechanical cycle is used to store and release the strain within the material. The strains are induced by elevating the temperature of the material above the glass transition temperature (T_g) of the resin and then applying a mechanical load to deform the material. Venturing above this critical temperature results in a 'rubbery' composite structure which allows high levels of

strain to be achieved without damaging the composite fibers or the resin system. While maintaining the mechanical load, the material is cooled below T_g . This 'freezes' the strain within the material. Now, the mechanical load can be removed and the EMC will remain deformed until it is once again heated above T_g . The heated material will release the strain energy stored within and will return to its original shape[71].

A study was conducted in 2002 by members of CTD and ABLE Engineering[115]. The purpose of the study was to determine the impact of using EMC longerons in the CoilAble™ boom design for NASA's Space Solar Panel System. The study determined that the longeron mass of the boom could be reduced up to a factor of ten while easily achieving effective strains of 2%. Repeated stowage and deployment cycles showed no substantial mechanical degradation.

1.4 Flexible Spacecraft Control

With the conclusion of the Apollo space program in the 1970s, NASA researchers turned their attention to the design of flexible space structures. This generated an increasing interest in the dynamics and control of such structures within various research communities. Several survey papers exist which provide a listing of published efforts in the area of controlling flexible structures. Robinson's survey[177] lists a small number of papers on structural control, and in particular on attitude control of flexible space structures. Croopnick et al.[50] present a literature survey in the areas of attitude control, vibration control and shape control as they apply to space structures. Meirovitch[149] assesses various methods for the active control of space structures with a view to the problems of high dimensionality and modeling. Balas[15] presents a mathematical framework for the discussion of large space structure (LSS) control theory and provides a look at trends in LSS control theory in the early 1980s. A comprehensive survey of problems in dynamic modeling and control of space structures is compiled by Nurre et al.[161]. One important thing to note from the surveys listed above is the

focus on the control of large flexible space structures; a focus which has predominately driven the field of study.

Flexible structures on small satellites are becoming increasingly popular. Actively controlling flexible structures is an important area of research[117]. The increased usage of flexible structures is related to the growing number of small satellites being launched, the use of lightweight materials, and the desire to meet tighter packaging requirements inside a launch vehicle's fairing[133]. Tethering spacecraft, deployable solar arrays, communication antennas, and extending scientific payloads away from the spacecraft bus are only a few examples where pointing accuracies, attitude information, and active control are required. The excitation of these appendages is highly probable while the spacecraft performs attitude control maneuvers. Reorientation of the spacecraft during these maneuvers is a critical part of the ADCS process so that the induced vibrations are kept to minimum levels[77].

Maghami, Sparks, and Lim (1998) identified four dynamic characteristics of flexible structures which complicate control system design[142].

- large number of structural modes in controller bandwidth
- low and closely spaced modal frequencies
- very small inherent damping
- insufficient knowledge of parameters

Even if the underlying physical model of the spacecraft could be accurately modeled at one point in time, parameter variations during system operation will eventually result in an inaccurate model[236]. The distributed parameter models often used to describe flexible structures are essentially infinitely dimensional and need to be truncated. This leads to complications of destabilizing one or more of the poorly damped modes since only some of the lower frequency modes are approximated and kept[130].

Research in the area of solid-state physics originally revealed how modal distortion may impede the propagation of vibrational energy[9]. Anderson's efforts led to improved predictions on the effects defects have in lattice vibrations. Almost five decades later, the theories derived from solid-state physics are being applied to flexible spacecraft structures[246]. When modal distortions occur, they tend to be localized in the region in which they were created. Most spacecraft flexible appendages are unactuated or unsensed. Slight structural asymmetries may complicate control design as the potential for large modal errors compared to modeled results will push for an overly conservative control design[150].

Another technique sensitive to modeling errors was the wave cancelation technique[203]. This technique drove a second-order system to its final position in finite time. In the early 1990s, researchers furthered this technique using a pulsed sequence expansion to desensitize their models[197]. Input shaping relies on the fact that a spectrum of a convolution of two signals is a product of each signal's spectra. Thus, a zero excitation frequency results when one or the other spectra is zero. By designing a sequence of input pulses, Singer and Seering (1990) forced the magnitude of the residual energy to zero. A time delay filter designed to cancel the poles of the system produced similar results while remaining insensitive to errors in modeled damping and frequency[199]. Multiple zeros of the time delay filter could also be placed at the estimated locations of the system poles to produce robust time-optimal control[131].

The general problem with frequency-based input shaping is they are designed for linear systems. A small satellite with extended flexible appendages is subjected to many disturbance torques, several of which are unmodeled. If the input shaping method accounts for nonlinearities by making robustness assumptions, the spacecraft bus may experience significant levels of residual vibration[107]. Time-domain representations and optimization of control inputs are usually easier to generalize. Non frequency-based input shaping techniques use either some type of inverse dynamics computation with a

known endpoint trajectory or an optimization technique to find a feedforward function to meet final conditions[170]. Some additional types of input shaping techniques either increase the range of uncertain parameters in regions where residual vibration is below a specified level[200] or include probability distributions of the uncertain parameters to weight the nominal value of the parameter the most[166].

Input shapes are designed to result in an exact time-optimal control algorithm. To do this, a "bang-bang" method of actuation is used. This method is an initial firing of the control actuators and is used to begin a maneuver; then the spacecraft is placed into a 'coast' mode. When the attitude sensors detect the system approaching the opposite threshold, the actuators fire in the opposite direction to stop the momentum from the initial maneuver. This attitude maneuver process continues, while the actuator inputs decrease in magnitude, until a narrow band of motion is achieved about the desired final position. The ADCS then monitors the satellite's motion until once again the sensors determine an attitude threshold is about to be breached.

The "bang-bang" method attempts to maximize the number of zero excitation frequencies in the input spectra. However, higher-order frequencies of the system can easily be excited with this method. A smoother control input is achieved by using an approximation function to eliminate the sudden change of control magnitudes[102]. The smoother control input is less likely to excite the structural modes and is calculated by solving an optimal control problem with the objective of minimizing the maneuver time. The solution utilizes the state equations describing the rigid-body mode, boundary conditions, and an additional constraint which limits the derivative of the control input[7]. Numerical solutions of Albassam's (2002) technique show the residual energy of the flexible appendages is greatly reduced while slightly increasing the maneuver time.

Accounting for modeling errors and uncertainties in control methods have been studied by several researchers[98][99][108][109][146][187][188][189][190][201][202][243][244]. However, one paper is of particular interest. Doyle and Stein[58] investigated the is-

sue of feedback control design in the face of uncertainties and generalized single-input, single-output statements and constraints of the design problem to multi-input, multi-output cases. They developed the procedure known as linear-quadratic-Gaussian/loop transfer recovery (LQG/LTR). Stein and Athans[213] provide a tutorial overview of the LQG/LTR procedure for linear multivariable feedback control design. This method is applied to robust controller synthesis for a large flexible space antenna by Joshi[98] and Sundararajan[216] while a modified version is presented by Belloch and Mingori[21].

The linear-quadratic-regulator (LQR) is a special optimal controller whose cost function, measure of performance, is a quadratic function of states and controls. Two desirable properties of the LQR are good stability margins and sensitivity properties. One limitation is that it is a full state feedback type of controller. In several practical applications, access to all of the states is difficult to achieve and state estimation will be required. The LQG problem combines the LQR controller with an estimation filter (i.e. Kalman filter). However, the LQG controller will often have lower stability margins and lower gain crossover frequency than the LQR controller. The LQG will pass more noise into the system and have a slower response when compared to the LQR.

The main problem with the LQG solution is its lack of robustness which has resulted in a failure to work effectively in real environments[212]. As more realism is added to the plant of the system, the LQG became unstable in the presence of model uncertainties. The loop transfer recovery technique (LQG/LTR) addresses some of the shortcomings of the LQG approach. The process begins with selecting the LQR parameters until a desired open-loop transfer function is obtained. The filter design parameters are iterated until the desired loop transfer function shape has been obtained. This allows the LQG technique to become a flexible frequency domain design technique. It is still based on state-space design techniques, but is more of a classical approach to controller design.

Usage of LQG/LTR techniques is applicable to current research efforts. In par-

ticular, Mackison[139][140][141] has used these techniques to develop controllers which retain the characteristics of full state feedback without requiring all of the states to be measurable. This work has demonstrated full state feedback, LQG/LTR feedback, and reduced order compensators derived from the LQG/LTR controller all produced identical dynamic responses for 3-axis attitude control problems. Smaller initial control torques were required for the LQG/LTR and reduced order controllers when compared to that required by full state feedback controllers. This result occurs because a low order transfer function for the controller is found through pole-zero cancellation techniques.

1.5 Problem Formulation

The support structure size of satellites are limited to the dimensions of the launch vehicle payload fairing being used to deliver the satellite to orbit. An exception to this occurs when the spacecraft is constructed in orbit. The International Space Station is one example of an operational space structure which was assembled after launch. However, the dimensions of the space station sections were limited by the size of the Space Shuttle delivery bay. A popular method used to alter the support structure size of a satellite is to package components prior to launch and then deploy these structures once the spacecraft is in orbit.

Deployable spacecraft structures are often used for communication antennas, creating larger surface areas for solar arrays, moving scientific payloads away from the satellite, and providing passive gravity gradient stabilization. These structures extend out from their stowed configuration using various forms of deployment mechanisms and energy sources. Reliability, low mass, packaged volume, and energy consumption are design concerns for deployable appendages. Since it is ideal to make these structures mechanically simple and light weight, they are susceptible to vibrations; either induced by attitude maneuvers of the spacecraft or external disturbance torques. These vibrations may prove detrimental to mission completion and become more of a concern as

the inertial properties of the satellite reduces.

The review of current literature in the areas of deployable structures and small satellites identifies a need to further relevant research. High levels of stored energy in mechanical deployment systems, as well as the use of pyrotechnic cutting bolts, require additional levels of inhibit measures to prevent premature release during launch environments. High packaged strain energy of traditional booms will limit the diameter of the boom while also producing low deployed stiffness and strength. In addition, the hazardous pyrotechnic release devices will produce high shock and contamination.

Mass limitations of small satellites may make redundant safety measures difficult to use. Reduced usable mass will also impact the sizing options of deployable structures available for small satellites. As the length of the appendage increases, so will its mass. This would lead to ruling out the use of small satellites to accomplish certain missions which would require longer deployed structures. Some examples of missions using long booms are interferometry, generating power along the boom length, determining plasma variations local to the satellite, conducting wake studies to predict spacecraft charging, and there are probably many more that we have not yet considered.

Shape memory materials show promise in minimizing the shortcomings in traditional booms. Although shape memory technology has been studied over the last 50 years (e.g. US Naval Ordnance Laboratory research in 1961), Elastic Memory Composites (EMC) are an emerging field of study. These composites will result in substantially lower densities and higher elastic strain capacities. By constructing a deployable structure from EMC materials, it is possible to eliminate the need for traditional highly complex mechanical deployment devices. These structures contain fewer non-structural components and are lighter in weight. A recent study completed by Composite Technology Development, Inc (CTD) determined longeron mass of a deployed structure could be reduced by an order of magnitude while achieving effective strains of 2%[115].

Constructing flexible structures from 'soft' materials will introduce more flexible

modes into the system dynamic equations of motion. Control designers will need to concern themselves not only with the additional flexible modes, but also the lower frequencies at which they occur. Research over the last three decades mainly focused on attitude control of large space structures with flexible appendages because a limited number of bending modes would form close to the control bandwidth. The large inertia values of these spacecraft helped to keep the control bandwidth low enough in frequency so that typically only the first bending mode was included in the analysis.

Attitude control authority of small satellites will be limited more from both increased resonant modes at lower frequencies as well as lower inertia values of the central body. Because of the added risk, small satellite engineers are more likely to select flexible appendages which have extensive flight heritage. The traditional response is to design around the flexible nature of the system by making the appendages stiffer, the spacecraft inertia larger, or lowering the attitude controller's closed loop bandwidth. Engineers from Surrey, a leading designer of small satellites, use only traditional booms and would not entertain the thought of appendages made from 'soft' materials. This directly results from the uncertainties involved and a perceived view of the high risks surrounding non-traditional booms. A concern arises when mission requirements call for the use of a small satellite as well as a flexible non-traditional structure.

To address this concern, this research will continue following the path defined by Mackison[139][140][141]. While the LQG/LTR technique was shown effective in generating reduced order controllers for 3-axis attitude control of spacecraft, Mackison only modeled the rigid body dynamics of the spacecraft. This research will examine the unique characteristics of controllers for a satellite with a flexible appendage constructed from EMC materials. In particular, this research will address the following basic question:

Will the LQG/LTR technique of controller design produce an effective controller for a small satellite using a non-traditional elastic memory

composite flexible appendage and how robust is the system in the face of material uncertainties, high frequency modeling errors, and appendage length modifications?

1.6 Research Importance

This research is both innovative and significant. A brief summary of the literature search in the area of flexible spacecraft modeling is provided here while a detailed literature study is provided in earlier sections within this chapter. This brief summary is given to set the stage for the reader on what researchers have done in the area of flexible spacecraft modeling. References are provided in author, year format while specific reference numbering is provided in the detailed literature search discussion.

1.6.1 Innovative

Modeling flexible spacecraft is not a new area of study. 60 years ago, structural analysis studies were first applied to spacecraft at the beginning of the "space race" between the United States and the former Soviet Union. Likins developed hybrid coordinate equations using cantilever boundary conditions in 1970, which was incorporated into NASA's Space Vehicle Design Criteria documents in 1971. Cantilever boundary conditions were continued to be utilized in the papers surveyed by Croopnick et al. in 1979, by Meirovitch in 1979, Balas in 1982, and Nurre et al. in 1984. The focus of the papers included in all of the surveys focused on the control of large flexible space structures and used cantilever boundary conditions in the formulation of the system's equations of motion. Some researchers mentioned that a similar process can be done for free-free boundary conditions, but none of them demonstrated or implemented equations of motion using free-free mode shapes; Canavin 1977, Sundararajan 1987, Junkins 1993, and Izzo 2004.

Over the years, spacecraft have become smaller in design. Even though several small flexible spacecraft would best be characterized as free-free systems, cantilever

assumptions are still being used (Gorinevsky 1998, Maghami 1998, Wie 1998, Lomas 2001, Bodineau 2004, Calise 2004, Gili 2004, Izzu 2004, Tafazoli 2004, Takahito 2004, Wilson 2004, and Ledesma 2005). This researcher is not stating these well informed people are making large errors in modeling. In some of the cases presented, assuming cantilever mode shapes is a valid assumption, but this assumption cannot be used on the formulation of the equations of motion for all small flexible spacecraft (see Section 2.2.2).

This research applies free-free boundary conditions to a small flexible spacecraft using a non-traditional gravity gradient boom constructed from Elastic Memory Composite material, demonstrates the development of the equations of motion using these conditions, and implements the equations in an attitude control scenario using LQG/LTR techniques. A key finding is the historical assumption of considering the spacecraft as a rigid body if the first resonant modes are greater than an order of magnitude when compared to the controller bandwidth may no longer be a valid assumption when a small flexible spacecraft is taken into consideration.

Two methods are described and compared for reducing the order of the controllers. Reducing the order of the controllers leads to fewer coefficients needed to be coded onto the satellite's on-board processor. Comparisons of the number of operations per computing cycle are discussed to aid a satellite designer during the on-board processor sizing task. In addition, several tools are provided for small satellite designers to determine the affects uncertainties in the material as well as varying the length of a gravity gradient boom will have on the satellite's performance parameters (such as settling time and stability robustness values).

1.6.2 Significance

The intention of this research is to provide an understanding of how attitude control of small satellites is impacted when attached flexible appendages are constructed from materials which are more elastic than traditional structures. A better under-

standing of how variations in elasticity and length of these appendages impact attitude control authority will aid designers in reducing some of the risks involved in using soft materials.

Although the 2002 CTD study makes EMC materials look promising, there are concerns. To date, only deployment hinges have been tested by CTD. In 2004, CTD developed a few test longerons constructed from EMC materials. However, only thermal cycling tests of small lengths (approximately 12 inches) in a vacuum chamber were conducted to determine battery sizing requirements to heat the material prior to deployment. Initial dynamic analysis of an EMC appendage offers preliminary data; however, a system test of an engineering model of the deployable structure has not been conducted. This analysis indicates a deployable structure made from EMC materials will have a bending frequency of 1.5 Hz and a torsional frequency of 1.7 Hz.

Constructing a deployable appendage from EMC material is a novel idea. The deployment mechanism is contained within the stored stress energy of the material itself and does not require mechanically complicated motors or added inhibit precautions needed on currently used traditional style booms. Small satellites will take advantage of the lighter mass systems and will begin to utilize missions requiring longer boom lengths.

The proposed research will support both commercial and governmental areas of research and development. Demonstrating the feasibility of space structures constructed from EMC materials is the next step in CTD's current design and implementation efforts in the area of EMC space structures. The Space Vehicles Directorate of the Air Force Research Labs is interested in CTD's technological advancements. In particular, the Power Sail program is considering the use of EMC deployment systems in their conceptual design. This study will identify the key areas of effectiveness in controlling such flexible space structures which will prove vital in allowing AFRL to pursue advanced designs in their Power Sail structure.

The United States Air Force Academy will use the findings of this research to complete risk assessments in the area of attitude determination and control of an EMC gravity gradient boom providing passive control to a small satellite. A successful integration of the boom into the next FalconSat spacecraft may provide an opportunity to generate flight heritage with the system before the end of 2010. This will offer a new way of deploying flexible space structures without the disadvantages of traditional systems.

Chapter 2

Equations of Motion

2.1 Flexible Spacecraft Modeling

The attitude motion of a flexible spacecraft is properly described by coupled sets of partial and ordinary differential equations. The rotational motion of the undeformed system, called the rigid body motion, is described by ordinary differential equations while the flexures are described by partial differential equations. The rigid body dynamics are derived from Euler's rotational equations of motion and include gravity gradient torques. Numerical finite element models are used to determine the mode shapes and natural frequencies as well as the mass, damping, and stiffness matrices of the flexible system[30]. The assumed modes method is used to couple the rigid body and flexible dynamics by using the spatial solutions of the partial differential equations as assumed mode shapes and letting the modal coefficients serve as the generalized coordinates describing the flexures.

This research considers the impact a flexible appendage has on the attitude control system of a small satellite. Topics such as meeting pointing requirements and attitude maneuvers are concerned with the rotational motion of the spacecraft while station keeping and changes in orbital parameters deal with the translation of the spacecraft. Eq. A.62 from Appendix A illustrates how the translational effects can be removed from the vibrational equations to leave a coupled set of rotation-vibration equations.

2.1.1 Rigid Body Dynamics

To begin the formulation of the equations of motion for a small satellite with a flexible appendage, consider Euler's rotational equations of motion shown as Eq. C.34 in Appendix C.

$$\begin{aligned}
 J_1 \dot{\omega}_1 - (J_2 - J_3) \omega_2 \omega_3 &= T_{c1} \\
 J_2 \dot{\omega}_2 - (J_3 - J_1) \omega_1 \omega_3 &= T_{c2} \\
 J_3 \dot{\omega}_3 - (J_1 - J_2) \omega_1 \omega_2 &= T_{c3}
 \end{aligned} \tag{2.1}$$

where J_1, J_2 , and J_3 are the principal moments of inertia of the undeformed system, ω_1, ω_2 , and ω_3 are the angular rates of motion about the principal axes (yaw, pitch, and roll respectively), and T_{c1}, T_{c2} , and T_{c3} are the attitude control torques of the spacecraft about these axes.

Expanding out the coupled terms, $\omega_i \omega_j$, and writing Eq. 2.1 in matrix notation produces

$$\begin{pmatrix} J_1 & 0 & 0 \\ 0 & J_2 & 0 \\ 0 & 0 & J_3 \end{pmatrix} \begin{pmatrix} \dot{\omega}_1 \\ \dot{\omega}_2 \\ \dot{\omega}_3 \end{pmatrix} + \begin{pmatrix} 0 & -\omega_3 & \omega_2 \\ \omega_3 & 0 & -\omega_1 \\ -\omega_2 & \omega_1 & 0 \end{pmatrix} \begin{pmatrix} J_1 & 0 & 0 \\ 0 & J_2 & 0 \\ 0 & 0 & J_3 \end{pmatrix} \begin{pmatrix} \omega_1 \\ \omega_2 \\ \omega_3 \end{pmatrix} = \begin{pmatrix} T_{c1} \\ T_{c2} \\ T_{c3} \end{pmatrix} \tag{2.2}$$

Since the spacecraft being modeled is on orbit and the flexible appendage is providing passive gravity gradient stabilization, gravitational forces need to be included. Using the local vertical and local horizontal (LVLH) reference frame to describe the orientation of the spacecraft places the 1st axis along the orbit direction (velocity or ram direction), the 2nd axis perpendicular to the orbital plane (orbit normal direction), and the 3rd axis pointing towards the Earth (nadir pointing).

Using the gravity gradient derivations included in Appendix B and the rotational

kinematics shown in Appendix C, the right hand side of Eq. 2.2 become

$$\begin{aligned}
&= \begin{pmatrix} T_{c1} \\ T_{c2} \\ T_{c3} \end{pmatrix} + 3n^2 \begin{pmatrix} 0 & -C_{33} & C_{23} \\ C_{33} & 0 & -C_{13} \\ -C_{23} & C_{13} & 0 \end{pmatrix} \begin{pmatrix} J_1 & 0 & 0 \\ 0 & J_2 & 0 \\ 0 & 0 & J_3 \end{pmatrix} \begin{pmatrix} C_{13} \\ C_{23} \\ C_{33} \end{pmatrix} \\
&= \begin{pmatrix} T_{c1} \\ T_{c2} \\ T_{c3} \end{pmatrix} + 3n^2 \begin{pmatrix} (-J_2 + J_3)C_{23}C_{33} \\ (J_1 - J_3)C_{13}C_{33} \\ (-J_1 + J_2)C_{13}C_{23} \end{pmatrix} \tag{2.3}
\end{aligned}$$

where $n = \sqrt{\frac{\mu}{R_o^3}}$ is the orbital rate, $\mu = 3.9860x10^{14}m^3/sec^2$ is the gravitational parameter for Earth, and R_o is the orbital radius of the spacecraft measured from the center of the Earth to the center of mass of the spacecraft. C_{13}, C_{23} and C_{33} are elements of the transformation matrix used to go from the LVLH frame to the body fixed frame.

Writing the equations of motion in differential form and moving the gravity gradient torques to the left hand side yields:

$$\begin{aligned}
J_1\dot{\omega}_1 - (J_2 - J_3)\omega_2\omega_3 + 3n^2(J_2 - J_3)C_{23}C_{33} &= T_{c1} \\
J_2\dot{\omega}_2 - (J_3 - J_1)\omega_1\omega_3 + 3n^2(J_3 - J_1)C_{13}C_{33} &= T_{c2} \\
J_3\dot{\omega}_3 - (J_1 - J_2)\omega_1\omega_2 + 3n^2(J_1 - J_2)C_{13}C_{23} &= T_{c3} \tag{2.4}
\end{aligned}$$

As shown in Appendix C.1.2, a singularity occurs in the kinematic equations. For a gravity gradient stabilized satellite, it is assumed the boom will be either zenith or nadir pointing. The only way the pitch or roll angles can equal 90° is if the boom is perpendicular to the gravitational force vector.

Consider the rotational sequence of $C_1(\theta_1) \leftarrow C_2(\theta_2) \leftarrow C_3(\theta_3)$ to the body frame from the LVLH frame:

$$\begin{pmatrix} \vec{b}_1 \\ \vec{b}_2 \\ \vec{b}_3 \end{pmatrix} = \begin{pmatrix} C_{11} & C_{12} & C_{13} \\ C_{21} & C_{22} & C_{23} \\ C_{31} & C_{32} & C_{33} \end{pmatrix} \begin{pmatrix} \vec{a}_1 \\ \vec{a}_2 \\ \vec{a}_3 \end{pmatrix}$$

$$\begin{pmatrix} \vec{b}_1 \\ \vec{b}_2 \\ \vec{b}_3 \end{pmatrix} = \begin{pmatrix} c\theta_2 c\theta_3 & c\theta_2 s\theta_3 & -s\theta_2 \\ s\theta_1 s\theta_2 c\theta_3 - c\theta_1 s\theta_3 & s\theta_1 s\theta_2 s\theta_3 + c\theta_1 c\theta_3 & s\theta_1 c\theta_2 \\ c\theta_1 s\theta_2 c\theta_3 + s\theta_1 s\theta_3 & c\theta_1 s\theta_2 s\theta_3 - s\theta_1 c\theta_3 & c\theta_1 c\theta_2 \end{pmatrix} \begin{pmatrix} \vec{a}_1 \\ \vec{a}_2 \\ \vec{a}_3 \end{pmatrix} \quad (2.5)$$

The angular velocity for this rotational sequence is

$$\vec{\omega}^{B/A} = \omega'_1 \vec{b}_1 + \omega'_2 \vec{b}_2 + \omega'_3 \vec{b}_3 \quad (2.6)$$

and

$$\begin{pmatrix} \omega'_1 \\ \omega'_2 \\ \omega'_3 \end{pmatrix} = \begin{pmatrix} \dot{\theta}_1 \\ 0 \\ 0 \end{pmatrix} + C_1(\theta_1) \begin{pmatrix} 0 \\ \dot{\theta}_2 \\ 0 \end{pmatrix} + C_1(\theta_1)C_2(\theta_2) \begin{pmatrix} 0 \\ 0 \\ \dot{\theta}_3 \end{pmatrix} \quad (2.7)$$

with

$$\begin{pmatrix} \omega'_1 \\ \omega'_2 \\ \omega'_3 \end{pmatrix} = \begin{pmatrix} 1 & 0 & -s\theta_2 \\ 0 & c\theta_1 & s\theta_1 c\theta_2 \\ 0 & -s\theta_1 & c\theta_1 c\theta_2 \end{pmatrix} \begin{pmatrix} \dot{\theta}_1 \\ \dot{\theta}_2 \\ \dot{\theta}_3 \end{pmatrix} \quad (2.8)$$

Now,

$$\vec{\omega} \equiv \vec{\omega}^{B/N} = \vec{\omega}^{B/A} + \vec{\omega}^{A/N} = \vec{\omega}^{B/A} - n\vec{a}_2 \quad (2.9)$$

and

$$\begin{aligned} \vec{a}_2 &= C_{12}\vec{b}_1 + C_{22}\vec{b}_2 + C_{32}\vec{b}_3 \\ &= (c\theta_2 s\theta_3)\vec{b}_1 + (s\theta_1 s\theta_2 s\theta_3 + c\theta_1 c\theta_3)\vec{b}_2 + (c\theta_1 s\theta_2 s\theta_3 - s\theta_1 c\theta_3)\vec{b}_3 \end{aligned} \quad (2.10)$$

produce

$$\begin{pmatrix} \omega_1 \\ \omega_2 \\ \omega_3 \end{pmatrix} = \begin{pmatrix} 1 & 0 & -s\theta_2 \\ 0 & c\theta_1 & s\theta_1 c\theta_2 \\ 0 & -s\theta_1 & c\theta_1 c\theta_2 \end{pmatrix} \begin{pmatrix} \dot{\theta}_1 \\ \dot{\theta}_2 \\ \dot{\theta}_3 \end{pmatrix} - n \begin{pmatrix} c\theta_2 s\theta_3 \\ s\theta_1 s\theta_2 s\theta_3 + c\theta_1 c\theta_3 \\ c\theta_1 s\theta_2 s\theta_3 - s\theta_1 c\theta_3 \end{pmatrix} \quad (2.11)$$

To solve for the kinematic differential equations, the 3x3 non-orthogonal matrix

above is inverted to finally yield:

$$\begin{pmatrix} \dot{\theta}_1 \\ \dot{\theta}_2 \\ \dot{\theta}_3 \end{pmatrix} = \frac{1}{c\theta_2} \begin{pmatrix} c\theta_2 & s\theta_1 s\theta_2 & c\theta_1 s\theta_2 \\ 0 & c\theta_1 c\theta_2 & -s\theta_1 c\theta_2 \\ 0 & s\theta_1 & c\theta_1 \end{pmatrix} \begin{pmatrix} \omega_1 \\ \omega_2 \\ \omega_3 \end{pmatrix} + \frac{n}{c\theta_2} \begin{pmatrix} s\theta_3 \\ c\theta_2 c\theta_3 \\ s\theta_2 s\theta_3 \end{pmatrix} \quad (2.12)$$

where the singularity now occurs with a pitch value of 90° .

Going back to the equations of motion in Eq. 2.4 and inserting the values $C_{13} = -s\theta_2$, $C_{23} = s\theta_1c\theta_2$, and $C_{33} = c\theta_1c\theta_2$ from Eq. 2.5, the equations of motion become

$$\begin{aligned} J_1\dot{\omega}_1 - (J_2 - J_3)\omega_2\omega_3 + 3n^2(J_2 - J_3)s\theta_1c\theta_2c\theta_1c\theta_2 &= T_{c1} \\ J_2\dot{\omega}_2 - (J_3 - J_1)\omega_1\omega_3 - 3n^2(J_3 - J_1)s\theta_2c\theta_1c\theta_2 &= T_{c2} \\ J_3\dot{\omega}_3 - (J_1 - J_2)\omega_1\omega_2 - 3n^2(J_1 - J_2)s\theta_2s\theta_1c\theta_2 &= T_{c3} \end{aligned} \quad (2.13)$$

Recall that the intention of this research is to determine the effect the flexible appendage has on the attitude control authority of a small satellite. Large slewing maneuvers of the satellite are not considered while certain pointing requirements are maintained. Therefore, it is safe to assume the satellite is moving through small angular displacements.

$$s\theta \approx \theta$$

$$c\theta \approx 1$$

$$\theta_1\theta_2 \approx 0$$

Applying small angle approximation to Eq. 2.13 yield:

$$\begin{aligned} J_1\dot{\omega}_1 - (J_2 - J_3)\omega_2\omega_3 + 3n^2(J_2 - J_3)\theta_1 &= T_{c1} \\ J_2\dot{\omega}_2 - (J_3 - J_1)\omega_1\omega_3 - 3n^2(J_3 - J_1)\theta_2 &= T_{c2} \\ J_3\dot{\omega}_3 - (J_1 - J_2)\omega_1\omega_2 &= T_{c3} \end{aligned} \quad (2.14)$$

Applying small angle approximation to the kinematic equations, Eq. 2.11, yield:

$$\begin{pmatrix} \omega_1 \\ \omega_2 \\ \omega_3 \end{pmatrix} = \begin{pmatrix} 1 & 0 & -\theta_2 \\ 0 & 1 & \theta_1 \\ 0 & -\theta_1 & 1 \end{pmatrix} \begin{pmatrix} \dot{\theta}_1 \\ \dot{\theta}_2 \\ \dot{\theta}_3 \end{pmatrix} - n \begin{pmatrix} \theta_3 \\ 1 \\ -\theta_1 \end{pmatrix} \quad (2.15)$$

Eq. 2.15 in differential form is

$$\omega_1 = \dot{\theta}_1 - \theta_2\dot{\theta}_3 - n\theta_3$$

$$\begin{aligned}
\omega_2 &= \dot{\theta}_2 + \theta_1 \dot{\theta}_3 - n \\
\omega_3 &= -\theta_1 \dot{\theta}_2 + \dot{\theta}_3 + n\theta_1
\end{aligned} \tag{2.16}$$

but $\theta_i \dot{\theta}_j \approx 0$, so

$$\begin{aligned}
\omega_1 &= \dot{\theta}_1 - n\theta_3 \\
\omega_2 &= \dot{\theta}_2 - n \\
\omega_3 &= \dot{\theta}_3 + n\theta_1
\end{aligned} \tag{2.17}$$

If orbital motion is assumed to be constant (i.e. no eccentricity in orbit), the time differential of Eq. 2.17 is

$$\begin{aligned}
\dot{\omega}_1 &= \ddot{\theta}_1 - n\dot{\theta}_3 \\
\dot{\omega}_2 &= \ddot{\theta}_2 \\
\dot{\omega}_3 &= \ddot{\theta}_3 + n\dot{\theta}_1
\end{aligned} \tag{2.18}$$

Inserting Eq. 2.17 and Eq. 2.18 into Eq. 2.14, applying small angle approximation, and collecting like terms results in

$$\begin{aligned}
J_1 \ddot{\theta}_1 + n(-J_1 + J_2 - J_3) \dot{\theta}_3 + 4n^2(J_2 - J_3)\theta_1 &= T_{c1} \\
J_2 \ddot{\theta}_2 - 3n^2(J_3 - J_1)\theta_2 &= T_{c2} \\
J_3 \ddot{\theta}_3 + n(J_1 - J_2 + J_3) \dot{\theta}_1 - n^2(J_1 - J_2)\theta_3 &= T_{c3}
\end{aligned} \tag{2.19}$$

Eq. 2.19 is the rigid body dynamics of a satellite in a circular orbit with gravity torques included. The dynamics of the flexible appendage still need to be included.

2.1.2 Flexible Dynamics

The method used to include the flexible dynamics of the appendage with the rigid body of motion of the satellite transforms the equations of motion in physical coordinates to decoupled vibrational equations (also known as modal equations but renamed here to

prevent confusion with the modal form of the state space equations). This is done using a linear coordinate transformation known as the modal transformation. In Appendix A, the displacement of the flexible system, $u(r, t)$, is expressed as

$$u(r, t) = \sum_{m=0}^{\infty} \phi_m(r) \eta_m(t) \quad (2.20)$$

where $\eta_m(t)$ is the m th vibrational coordinate and $\phi_m(r)$ is the m th normal mode shape of the mode shape matrix, $[\phi]$, whose columns are the eigenvectors of the system.

The differential equations of motion for an undamped free vibration system are of the form

$$[m]\ddot{u} + [k]u = 0 \quad (2.21)$$

where the matrices $[m]$ and $[k]$ are arbitrary mass and stiffness matrices of the system with symmetric and constant elements. Since $[\phi]$ is a spatial variable and η is a temporal variable, we can insert Eq. 2.20 into Eq. 2.21 and get

$$[m][\phi]\ddot{\eta} + [k][\phi]\eta = 0 \quad (2.22)$$

Premultiplying by $[\phi]^T$ yields

$$[M]\ddot{\eta} + [K]\eta = 0 \quad (2.23)$$

where

$$\begin{aligned} [M] &= [\phi]^T [m] [\phi] = [M]^T \\ [K] &= [\phi]^T [k] [\phi] = [K]^T \end{aligned}$$

If $[\phi]$ is orthonormal, then the generalized mass matrix, $[M]$, is the identity matrix ($[M] = \text{diag}(1, \dots, 1)$) and the generalized stiffness matrix, $[K]$, is a diagonal matrix whose elements are equal to the natural frequencies squared ($[K] = \text{diag}(\omega_0^2, \omega_1^2, \dots, \omega_n^2)$). Since both generalized matrices are diagonal, it makes the vibrational equations both inertially uncoupled and elastically uncoupled. This results in independent equations

of flexible motion. If there are m mode shapes included in the analysis, these equations look like the following:

$$\begin{aligned}
 \ddot{\eta}_1 + \omega_1^2 \eta_1 &= 0 \\
 \ddot{\eta}_2 + \omega_2^2 \eta_2 &= 0 \\
 &\vdots \\
 \ddot{\eta}_m + \omega_m^2 \eta_m &= 0
 \end{aligned} \tag{2.24}$$

where η_m is the m th vibrational coordinate associated with the m th mode shape and ω_m is the m th natural frequency. Therefore, η has dimensions of $(1 \times m)$. The mode shape matrix, $[\phi]$ will have dimensions of $(6n \times m)$ where n is the number of nodes used in the finite element analysis and each node has six degrees of freedom (three translation and three rotation for each node). The number of nodal points used in the FEM analysis is up to the discretion of the researcher. However, a more accurate estimate of the deformation of the flexible system is found by using more nodal points to reduce approximation errors in the displacement of each element.

The vibrational equations of motion are propagated along with the rigid body equations. If the movement of certain points along the flexible appendage are of interest, then inserting the updated vibrational coordinates into Eq. 2.20 will generate the displacement function $u(r, t)$ in physical coordinates. To illustrate this, consider a simple example of a flexible appendage in which three nodes are selected for the FEM analysis.

Each node is free to translate in three directions (T1, T2, T3) but for now we will disregard rotation in three directions (R1, R2, R3). Also, let's assume three mode shapes are used in the analysis. Then the physical coordinates of the appendage are

found as follows:

$$u(r, t) = \begin{pmatrix} \text{Node1T1MS1} & \text{Node1T1MS2} & \text{Node1T1MS3} \\ \text{Node1T2MS1} & \text{Node1T2MS2} & \text{Node1T2MS3} \\ \text{Node1T3MS1} & \text{Node1T3MS2} & \text{Node1T3MS3} \\ \text{Node2T1MS1} & \text{Node2T1MS2} & \text{Node2T1MS3} \\ \text{Node2T2MS1} & \text{Node2T2MS2} & \text{Node2T2MS3} \\ \text{Node2T3MS1} & \text{Node2T3MS2} & \text{Node2T3MS3} \\ \text{Node3T1MS1} & \text{Node3T1MS2} & \text{Node3T1MS3} \\ \text{Node3T2MS1} & \text{Node3T2MS2} & \text{Node3T2MS3} \\ \text{Node3T3MS1} & \text{Node3T3MS2} & \text{Node3T3MS3} \end{pmatrix} \begin{pmatrix} \eta_1 \\ \eta_2 \\ \eta_3 \end{pmatrix} \quad (2.25)$$

where, for example, Node3T1MS2 is the eigenvector value describing the displacement of the third node in the first direction in response to the second mode shape. If the total displacement of the third node in the first direction is required, it would be

$$u = \phi_{7,1}\eta_1 + \phi_{7,2}\eta_2 + \phi_{7,3}\eta_3 \quad (2.26)$$

This can be done for each of the three nodes in the three translational directions. More complicated models which contain a greater number of nodes will produce better estimates of the displacement shape of the flexible system, but will require more nodes as well as rotation in three directions along with translational motion.

2.1.3 The Coupling Equation

The rigid body equations need to be coupled with the vibrational equations. The hybrid coordinate approach[129] presents the rigid body equations and appendage deformation in the form

$$\begin{aligned} I\ddot{\theta} - \delta^T \ddot{\eta} &= T_c \\ \ddot{\eta} + 2\zeta\omega_n \dot{\eta} + \omega_n^2 \eta - \delta \ddot{\theta} &= 0 \end{aligned} \quad (2.27)$$

where δ is called the coupling matrix[127]. Solving the Lagrange equations in Appendix A yields the following definition for the coupling matrix:

$$\delta = X_1^T \tilde{R} - X_3^T \quad (2.28)$$

where

$$\begin{aligned} X_1 &= \int_{app} [\phi] dm \quad (3 \times m) \\ X_3 &= \int_{app} r[\phi] dm \quad (3 \times m) \end{aligned} \quad (2.29)$$

Closed form solutions can be found for the mass and inertia integrals in Eq. 2.29 and the coupling matrix is rewritten as

$$\delta = -\bar{\phi}^T M_c (\Sigma_{OE} - \Sigma_{EO} \tilde{R} - \tilde{r} \Sigma_{EO}) \quad (2.30)$$

where $\bar{\phi}$ is the truncated mode shape matrix, M_c is the generalized ($6N \times 6N$) inertia matrix of N cantilevered appendages, Σ_{OE} and Σ_{EO} are summation matrices consisting of ones and zeros, and \tilde{R} and \tilde{r} are skew symmetric matrices of position vectors. Each variable is explained in further detail below to aid in the application of Eq. 2.30.

A concern arises when looking at the dimensions of $[\phi]$ used in Eq. 2.29. As shown, the coupling matrix has dimensions ($m \times 3$). However, the mode shape matrix takes the form ($6n \times m$). The coupling matrix couples the rotational motion of the satellite with the flexible motion of the appendage and there is a constraint relationship between the two as illustrated in Figure 2.1.

$U_{S/C}$ is a point located on the spacecraft while U_{app1} is the location of the first node used in the FEM analysis. Notice that both of these points are located at the connection point between the spacecraft and the flexible appendage. As a result, the displacement and rotation of $U_{S/C}$ is the same as those of U_{app1} . It is at this location where rotational (and translational) energy is passed between the spacecraft and the flexible appendage. Therefore, while the mode shape matrix may take the form of

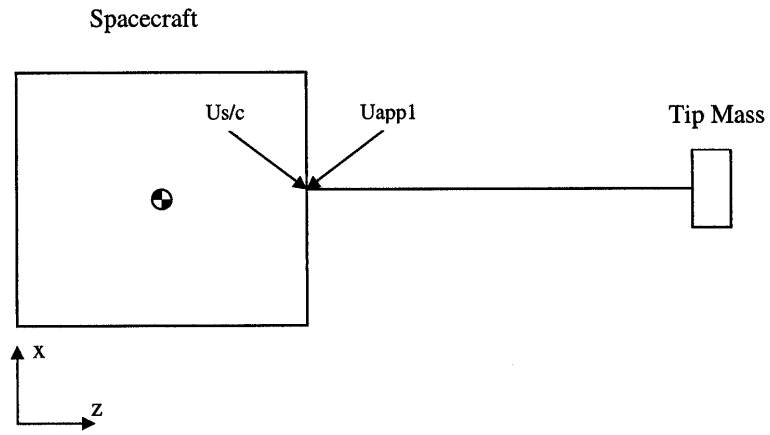


Figure 2.1: Rotational-Vibrational Constraint Illustration

$$[\phi] = \begin{pmatrix} N1T1MS1 & \cdots & N1T1MSm \\ N1T2MS1 \\ N1T3MS1 \\ N1R1MS1 \\ N1R2MS1 \\ N1R3MS1 \\ N2T1MS1 \\ \vdots \\ NnR3MS1 & \cdots & NnR3MSm \end{pmatrix} \quad (2.31)$$

the coupling matrix only relies on the translations and rotations of the first node.

$$\bar{\phi} = \begin{pmatrix} N1T1MS1 & \cdots & N1T1MSm \\ N1T2MS1 & \cdots & N1T2MSm \\ N1T3MS1 & \cdots & N1T3MSm \\ N1R1MS1 & \cdots & N1R1MSm \\ N1R2MS1 & \cdots & N1R2MSm \\ N1R3MS1 & \cdots & N1R3MSm \end{pmatrix} \quad (2.32)$$

which now puts the mode shape matrix in a truncated form with dimensions $(6 \times m)$. Note, Eq. 2.32 contains information for only one appendage. If N additional flexible appendages are considered, append the rows of the truncated mode shape matrix with the nodal information for the connection points to each flexible structure. Thus, the dimensions become $(6N \times m)$.

The generalized inertia matrix of cantilevered appendages, M_c , is comprised of the masses and inertias of each connected appendage and takes the form

$$M_c = \begin{pmatrix} m1 & 0 & 0 & 0 & 0 & 0 & 0 \\ 0 & I1 & 0 & 0 & 0 & 0 & 0 \\ 0 & 0 & m2 & 0 & 0 & 0 & 0 \\ 0 & 0 & 0 & I2 & 0 & 0 & 0 \\ 0 & 0 & 0 & 0 & \ddots & 0 & 0 \\ 0 & 0 & 0 & 0 & 0 & mN & 0 \\ 0 & 0 & 0 & 0 & 0 & 0 & IN \end{pmatrix} \quad (2.33)$$

where $m1$ is the (3×3) mass matrix of the first appendage such that

$$m1 = \begin{pmatrix} m_{app1} & 0 & 0 \\ 0 & m_{app1} & 0 \\ 0 & 0 & m_{app1} \end{pmatrix} \quad (2.34)$$

and I_1 is the (3×3) inertia matrix of the first appendage such that

$$I_1 = \begin{pmatrix} I_{appx} & 0 & 0 \\ 0 & I_{appy} & 0 \\ 0 & 0 & I_{appz} \end{pmatrix} \quad (2.35)$$

\tilde{R} and \tilde{r} are skew symmetric matrices of the position vectors which have the general form

$$\tilde{R}1 = \begin{pmatrix} 0 & -R1_3 & R1_2 \\ R1_3 & 0 & -R1_1 \\ -R1_2 & R1_1 & 0 \end{pmatrix} \quad (2.36)$$

where $\vec{R}1$ is the position vector from the system center of mass to the connection point of the first appendage and $\vec{r}1$ is the position vector from the connection point of the first appendage to the center of mass of the first appendage.

Multiple appendages are accounted for by utilizing the summation matrices Σ_{OE} and Σ_{EO} . These matrices are Boolean operator matrices of the form

$$\begin{aligned} \Sigma_{OE} &= \begin{pmatrix} O & E & O & E & \dots & O & E \end{pmatrix}^T \\ \Sigma_{EO} &= \begin{pmatrix} E & O & E & O & \dots & E & O \end{pmatrix}^T \end{aligned} \quad (2.37)$$

where O is a (3×3) zero matrix and E is a (3×3) identity matrix.

The coupling matrix is general enough that the same concept not only applies to a satellite with a flexible gravity gradient boom, but also works for solar arrays, multiple flexible appendages of various shapes and elasticity, etc. What changes from each of these instances is the mode shape matrix generated during FEM analysis. The coupling matrix contains all of the dynamics used in coupling the rigid body dynamics with each of the flexible appendages.

Table 2.1: Material Properties of Beryllium Copper and EMC

	Beryllium Copper	EMC
Young's Modulus, E [<i>GPa</i>]	138	40.06
Poisson Ratio, ν	0.30	0.31
Shear Modulus, G [<i>GPa</i>]	53.1	15.29
Density, ρ [$\frac{kg}{m^3}$]	8830	1384

2.2 Finite Element Model

Since the coupling matrix is dependent upon the properties of the satellite, the type and number of flexible appendages, and the materials used in the construction of the appendage, the illustration shown in Figure 2.1 will describe the set up of the system to be modeled. The spacecraft will be a typical small satellite based on the FalconSat system described in Appendix D. The flexible appendage is a non-traditional gravity gradient boom constructed from Elastic Memory Composite (EMC) materials with a cubic tip mass.

2.2.1 Model Parameters

As mentioned in Section 1.2, beryllium copper is a common alloy used in traditional beam elements. Table 2.1 lists the material properties for both beryllium copper[1] and EMC materials[206]. The composite material used in the finite element model (FEM) not only is more flexible but also has 15.7% the density of materials which traditional booms are constructed from.

The EMC material properties were entered in MSC.Patran 2004 r2 to create a FEM of a cantilevered beam with lumped masses at either end to represent the satellite and tip mass. The satellite lumped mass boundary conditions are fixed while the tip mass is allowed to move. The lumped masses were treated as cubic shapes with uniform

Table 2.2: Lumped Mass Properties Used in FEM Analysis

	Satellite	Tip Mass
Mass	40kg	7kg
Side Length	0.5m	0.25m
Inertia	1.667kgm ²	0.0729kgm ²

mass distribution. For a cubic shape with uniform mass distribution, the inertia about the object's center of mass is

$$I_{11} = I_{22} = I_{33} = \frac{ml^2}{6} \quad (2.38)$$

where m is the mass of the object, l is the length of a side and the products of inertia are equal to zero. Table 2.2 lists the properties entered into the FEM for the satellite and tip mass.

The beam representing the EMC flexible appendage is modeled as a hollow, cylindrical tube with properties shown in Table 2.3 to resemble the initial design characteristics of the EMC appendage[206]. One hundred node points were used in the analysis evenly spaced 4cm apart to minimize the approximation errors in the mode shapes.

A normal modes solution type was selected to complete a full run of the entire model. This solution will generate the eigenvectors for all available modes. The nominal (or truth) model used in the analysis includes the first eighteen resonant modes, regardless of their impact (as with the compression mode) or modes which are disregarded during order reduction methods of the controller.

The first eighteen mode shapes generated for the cantilevered appendage are listed in Table 2.4 while plots of the first three bending modes and the torsional mode are provided in Figures 2.2-2.5. One thing to consider is the compression mode places very minimal torque on the satellite if the center of mass of the appendage is placed on one of the principal axes of the system. This is validated by looking at the angular

Table 2.3: Beam Properties Used in FEM Analysis

Property	Value
Total Length	$4m$
Outer Diameter	$2.54cm$
Thickness	$0.46482mm$
Cross Sectional Area	$73.5mm^2$
$I_{11} = I_{22}$	$2.3 \times 10^{-8}kgm^2$

displacement eigenvector of the compression mode for the first node of the appendage connected to the satellite.

$$\begin{pmatrix} N1R1MS8 \\ N1R2MS8 \\ N1R3MS8 \end{pmatrix} = \begin{pmatrix} 2.446 \times 10^{-15} \\ 2.522 \times 10^{-13} \\ -2.765 \times 10^{-16} \end{pmatrix} \quad (2.39)$$

The compression mode is left in the nominal model, but will most likely not appear in the controller design model because of order reduction techniques.

Table 2.4: Cantilever Resonant Frequencies From FEM Analysis

Mode Shape	Frequency (Hz)
1 st Bending in Y direction	0.3947
1 st Bending in X direction	0.3947
1 st Torsional Mode	7.8585
2 nd Bending in Y direction	12.141
2 nd Bending in X direction	12.141
3 rd Bending in Y direction	29.322
3 rd Bending in X direction	29.322
1 st Compression Mode	51.116
4 th Bending in Y direction	61.567
4 th Bending in X direction	61.567
5 th Bending in Y direction	115.62
5 th Bending in X direction	115.62
6 th Bending in Y direction	188.56
6 th Bending in X direction	188.56
7 th Bending in Y direction	279.26
7 th Bending in X direction	279.26
8 th Bending in Y direction	386.96
8 th Bending in X direction	386.96

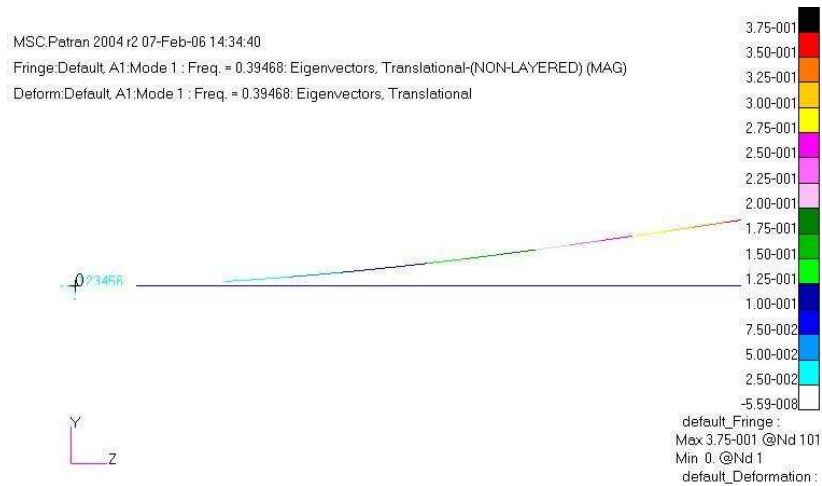


Figure 2.2: First Bending Mode For Cantilever Conditions

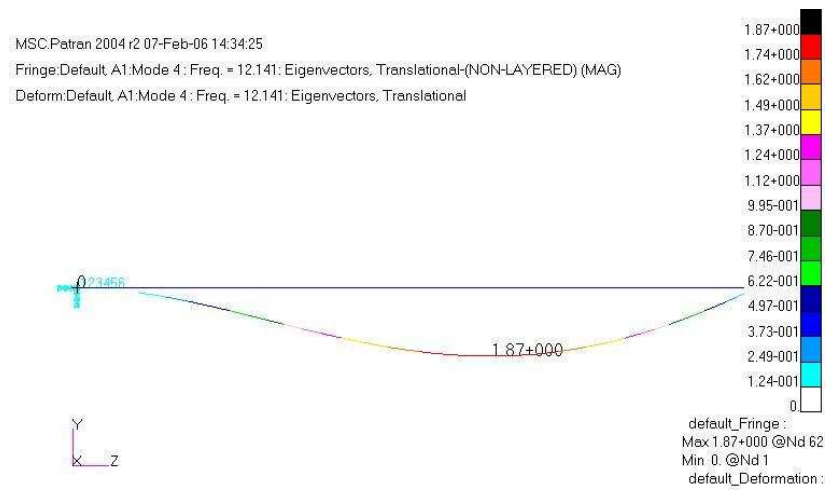


Figure 2.3: Second Bending Mode For Cantilever Conditions

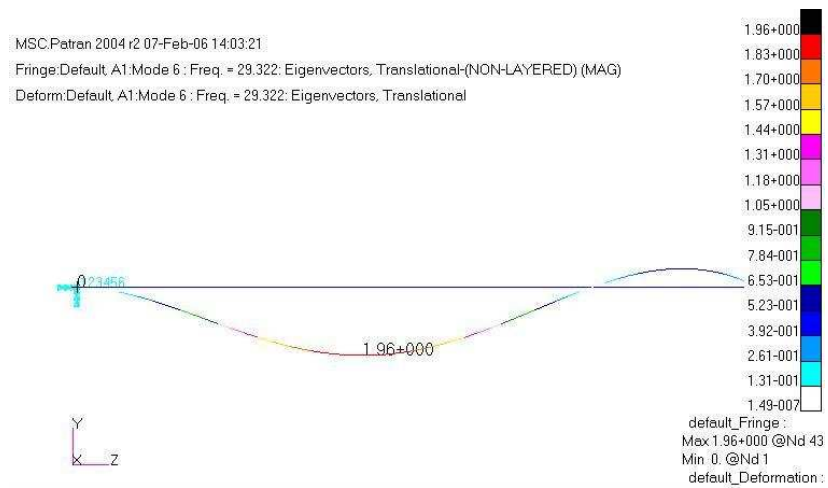


Figure 2.4: Third Bending Mode For Cantilever Conditions

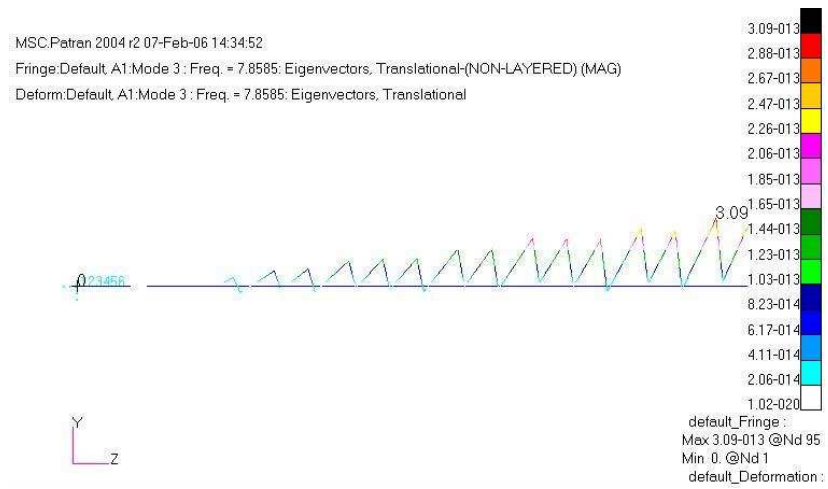


Figure 2.5: First Torsional Mode For Cantilever Conditions

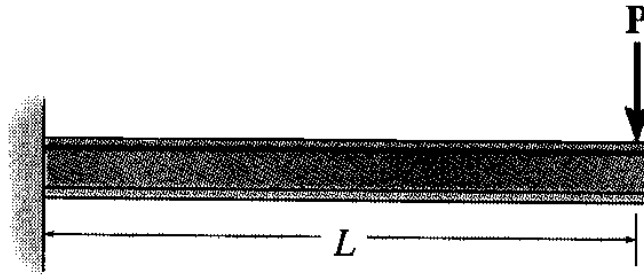


Figure 2.6: Cantilever Beam with Applied Point Load

2.2.2 Free-Free Boundary Conditions

The traditional hybrid coordinate equation model first presented by Likins in a 1970 Jet Propulsion Laboratory Technical Report[127] has strongly influenced the dynamical modeling of flexible spacecraft. The simplified rotational/vibrational coupled equations, Eq. 2.27, is found in one form or another in the works of several key researchers in the field of flexible dynamics. While the references are too numerous to list here, the survey papers presented in [177] [50] [149] [15] [161] provide a broad enough summary of the collection of work.

The literature considers cantilever modes when analyzing the flexible appendage (see Section 1.6.1). A common definition in the structures community for a cantilever beam is a slender member which is fixed at one end and free at the other that supports loadings that are applied perpendicular to their longitudinal axis[86]. The boundary conditions applied to the fixed end of the beam restrain both translational and rotational motion. During the generation of the equations of motion for the beam, either a point load is applied at some location along the appendage, Figure 2.6, or as a distributed load along the appendage length, Figure 2.7.

When a flexible appendage is attached to a symmetrical spacecraft, the root node, or connection point between the appendage and spacecraft bus, does both rotate and translate. If one looks at the system as a whole, cantilever modes doesn't

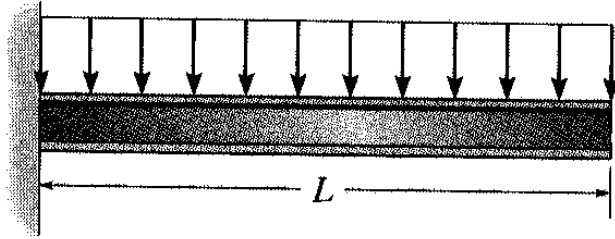


Figure 2.7: Cantilever Beam with Applied Distributed Load

make sense due to the motion of the root node. The literature assumes the flexible appendage is "cantilever like" when deriving the mode shape matrix and the accepted practice in flexible spacecraft modeling is to calculate the cantilever mode shapes of the attached appendage and couple the resulting mode shape matrix with the spacecraft non-vibrational equations of motion. This hybrid approach is valid if one looks at a body fixed reference frame located at the root node, since in this frame the connection point between the appendage and spacecraft bus does not appear to either rotate or translate.

Modeling the flexible appendage as a cantilevered beam is the correct approach when dealing with attitude control of large space structures. The boundary conditions at one end have the appendage fixed in translation and rotation. This is a valid assumption when the total system center of mass is located close to the center of mass of the controlling body. Two examples of when this occurs is large space structures when $m_{CB} \gg m_{app}$ and when flexible appendages are symmetrically orientated about the controlling body (as shown in Figure 2.8 and Figure 2.9). The torque generated by the displaced appendage is applied at the connection point between the controlling body and the appendage. The torque experienced by the controlling body is in the same direction as it is generated from the appendage.

For both the large flexible spacecraft and symmetrical appendage configuration examples, the position of the system center of mass experiences small displacements[31].

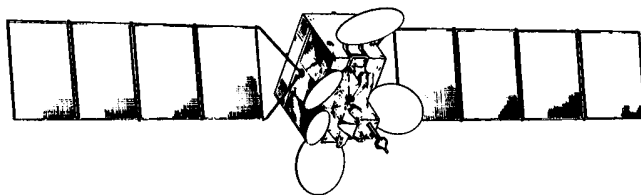


Figure 2.8: Three-Axis-Stabilized Geosynchronous Communications Satellite[237]

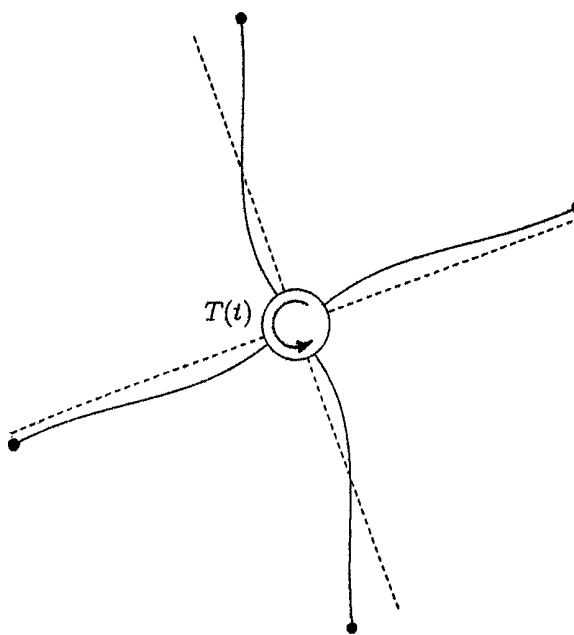


Figure 2.9: Example of a Symmetrical Appendage Configuration

As the system is deformed in asymmetrical modes, the velocity of the system center of mass, and therefore the time rate of change of the moments of inertia, are approximately zero[100]. This eliminates several terms from the Lagrangian equations and simplifies the resultant equations of motion. Likins' work retained asymmetric modes corresponding to known cantilever modes while showing that the symmetric modes contributed nothing and could be ignored[129].

For a gravity gradient stabilized small satellite, the assumption of a cantilever appendage is no longer as valid as it is for a large space structure. The flexible appendage is attached to both the spacecraft bus and the tip mass. To determine which end is free, one can argue that the end which does not generate loads perpendicular to the longitudinal axis would be free to move. Thus, the tip mass is merely considered as part of the appendage which is no longer uniform in mass distribution. Tethered spacecraft, however, confuse this definition if both masses tethered are identical each with their own attitude control systems. In these cases, it is no longer clear which end is fixed and which end is free. The conventional definition of cantilevered beams breaks down.

This is especially true as the mass of the satellite gets closer to the mass of the attached appendage and tip mass. As these two ends come closer to each other in mass, the system center of mass moves away from a location within the constrained boundary condition and is found at some point along the appendage itself. A better approach is to consider the appendage as a free-free beam with attached lumped masses at either end for the satellite and tip mass. Now, each end of the appendage is allowed to translate and rotate when determining the mode shapes used to couple the rigid body and flexible dynamics. This is a more realistic assumption when dealing with small satellites because the attitude of the satellite is directly impacted by the motion of the appendage. For a cantilever assumption, the satellite doesn't move as a result of appendage motion.

For the free-free assumption, the center of mass of the total system is not necessarily contained within the controlling body, nor along one of the principle axes. In

Table 2.5: Free-Free System Eigenvalues Using Unmodified HCEs

Eigenvalue	Coupled Pair
0	0
$-0.19803 + 19.8023j$	$-0.19803 - 19.8023j$
$0 + 0.00217j$	$0 - 0.00217j$
$0 + 0.00188j$	$0 - 0.00188j$
67.0388	-67.0388
9.08888	-9.08888

fact, as the satellite mass comes closer to that of the tip mass, the center of mass of the total system will move along the appendage length. One example, where the satellite mass and tip mass are equal, places the center of mass equidistant from the satellite and tip mass. In this situation, the position vector of the system center of mass in the body frame is time varying as well as the system's moments of inertia. Now, when a torque is generated at the tip mass, the controlling body will experience an equal torque in the opposite direction.

A concern arises when the hybrid coordinate equations (HCEs) (Eq. 2.27) are used for the free-free system without modification. The coupling term is the representation of how torque between the controlling body and the flexible appendage is transferred at the connection point. If the HCEs are unmodified when applied to the free-free boundary condition, the system plant demonstrates responses similar to that of an inverted pendulum where one or more open loop poles are placed on the real axis and mirrored in the left and right half parts of the plane. The eigenvalues for the system plant which includes the first three resonant modes are listed in Table 2.5.

A way to visualize the impact of not modifying the HCEs for the free-free condition is to look at the open loop response of the system. If a gravity gradient spacecraft orientation is initially roll= 5° , pitch= 0° , and yaw= 0° , the open loop response should

show the spacecraft oscillating between $\pm 5^\circ$ if no energy is lost from the system. However, this is not the case (see Figure 2.10).

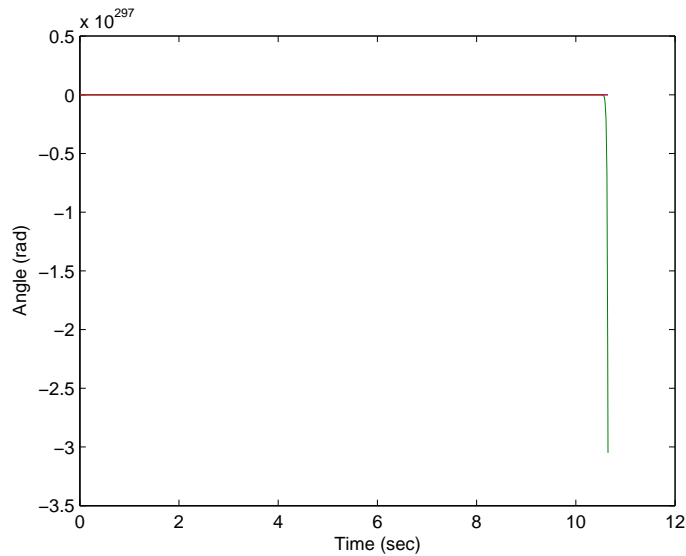


Figure 2.10: Open Loop Response of Unmodified HCEs

If a flexible system is modeled correctly, it should contain a combination of rigid body and flexible modes. The rigid body dynamics will generate $\frac{1}{s^2}$ terms while the flexible dynamics produce $\frac{1}{s^2+2\zeta\omega_n s+\omega_n^2}$ terms. This places the open loop poles either at the origin or very close to the imaginary axis for lightly damped poles. The eigenvalues listed in Table 2.5 indicates the system model is incorrect.

Consider an example where a designer is attempting to model an undamped resonant mode with a natural frequency of 1 rad/sec. The designer derives the following two system plants:

$$\begin{aligned} \text{Case1} &= \begin{pmatrix} 0 & 1 \\ 1 & 0 \end{pmatrix} \\ \text{Case2} &= \begin{pmatrix} 0 & 1 \\ -1 & 0 \end{pmatrix} \end{aligned} \quad (2.40)$$

which produce characteristic equations of $s^2 - 1$ for Case1 and $s^2 + 1$ for Case2. The

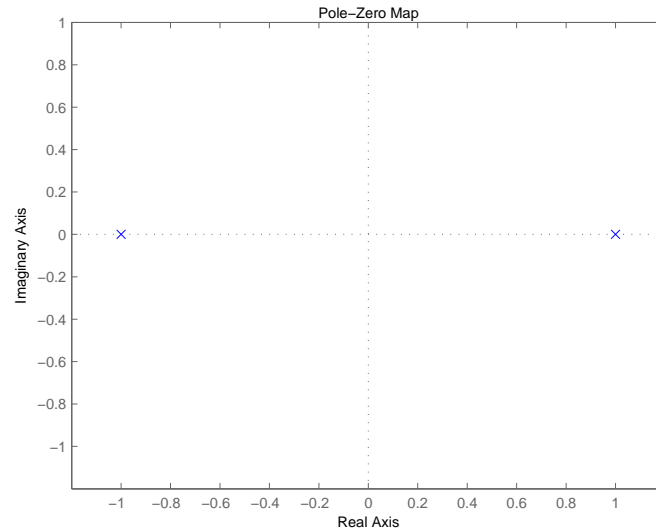


Figure 2.11: Pole-Zero Map for $\frac{1}{s^2-1}$

pole placement for both cases are shown in Figure 2.11 and Figure 2.12. A sign error in the system plant can change the desired model for Case2 to that of an unstable system shown in Case1.

The choice of mode shapes used to describe the deformation of the system is crucial. The cantilever modes apply to a restrained system in which the controlling body is assumed to neither translate nor rotate when the mode shape matrix is formed. A better assumption is to no longer restrain the system and use the free-free mode shapes in the equations of motion. This allows complete freedom of motion in response to impressed moments and forces. In a Tisserand frame[38], the expressions for angular momentum and kinetic energy are structurally simplified by moving the axes so as to set the internal angular momentum always to zero. The requirement also makes the internal linear momentum zero. This constraint is accomplished by locating the origin of the frame at the center of mass of the system. Now that the frame moves with the body, a floating reference frame, the measured displacements relative to this frame will be small where an inertial frame will see large displacements as the body undergoes

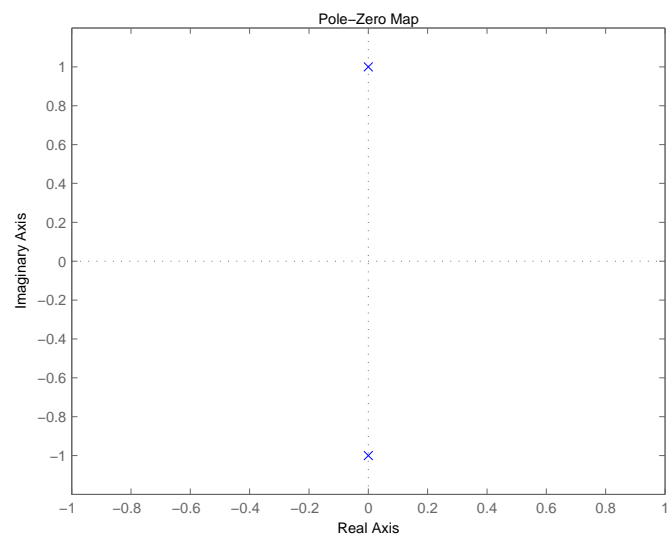


Figure 2.12: Pole-Zero Map for $\frac{1}{s^2+1}$

appreciable rotation.

The use of the floating reference frame is shown in Buttrill's study[31] for flexible aircraft but the methods are valid for a spacecraft as well. The following assumptions used in the study will also apply to this research:

- the spacecraft is idealized as a collection of lumped mass elements, each being a finite rigid body, and each having an associated mass and moments of inertia
- the elastic restoring force resulting from displacement of any mass element is linear and proportional to that displacement
- the total rotational displacement of any lumped mass with respect to its undeformed orientation is small
- deformation is described by a linear sum of mode shapes multiplied by their time dependent participation coefficients

the implications of the above assumptions are summarized in the following statements:

- each mass element resides at a node of the structural finite-element model and constitutes a lumped resistance to acceleration
- proportional strain to stress relationships
- tip deflection is $< 10\%$ of beam length
- $u = \Sigma \phi_i \eta_i$ as shown in Eq. 2.20

To satisfy the minimum relative kinetic energy requirement of a floating reference frame, Bucken's constraint relationships must be considered[103].

$$\begin{aligned} \Sigma_i \phi_{ij} dm_i &= 0 \\ \Sigma_i \tilde{r}_i \phi_{ij} dm_i &= 0 \end{aligned} \tag{2.41}$$

if the assumed mode shapes are the eigenvectors of a structural model in undamped vibration with free-free boundary conditions, then motion according to each mode shape j should satisfy the conditions.

These constraints define the assumed modes method integral terms, X_1 and X_3 , shown in Eq. 2.29. When applied to Eq. 2.28,

$$\begin{aligned}\delta &= X_1^T \tilde{R} - X_3^T \\ \delta &= 0\end{aligned}\tag{2.42}$$

which reduces Eq. 2.27 to

$$\begin{aligned}I\ddot{\theta} &= T_c \\ \ddot{\eta} + 2\zeta\omega_n\dot{\eta} + \omega_n^2\eta &= 0\end{aligned}\tag{2.43}$$

and there no longer exists angular-vibrational momentum exchange.

Kakad provides a solution which does not rely on the hybrid coordinate equation[103]. This study discusses the dynamics and control of slewing maneuvers of a large flexible spacecraft named NASA Spacecraft Control Laboratory Experiment (SCOLE). The system was modeled as a distributed parameter beam with two end masses. The three dimensional linear variation analysis of this free-free beam model is incorporated together with rigid-slewing maneuver dynamics. Beam vibrations at the end of slewing maneuvers were controlled using the infinite time Linear Regulator Problem formulation. The results illustrated how slew angle changes vs time changed between a model using only rigid body modes and a model which added the first two flexible modes to the rigid body equations.

Kakad's analysis of higher uncontrolled modes indicated serious control spillover due to coupling among the modes. This indicated the residual modes were excited by feedback control which is designed for a low-order model, senses and actuates higher-order modes, and renders the system unstable[14] [124]. Spillover can be avoided by

reducing the control gain. However, this often results in poor performance. To improve performance, control objectives lead to high-gain, high-bandwidth control strategies which reduce inherent frequency separation between rigid body and elastic dynamics and increases the possibility for adverse coupling when control loops are closed[233].

The SCOLE system modeled by Kakad deals with slewing maneuvers of an antenna attached at one end of a shuttle robotic arm. Although similar techniques were used by Kakad in his analysis, free-free modeling with linear quadratic control, several differences between that work and the research presented in this document exist. The on-orbit mass of the shuttle is approximately 100,000 kg while the spacecraft bus modeled here is 40 kg. Kakad's results demonstrated the change in slew response between a rigid body model and one which includes the first two flexible modes. However, he doesn't mention the robustness of the system, what the cost/benefits are of including or not including flexible modes, nor provides an explanation as to why he included the first resonant modes and not higher order frequencies. At no point in his paper does he mention the "rule of thumb" of considering the system as a rigid body (information on crossover frequency in relation to the first resonant mode was not provided).

While Kakad's study considered a free-free system, it was similar to several other studies focused on flexible dynamic control of a rotating hub with an attached whip appendage[242] [248]. These studies focused on single axis analysis to avoid the adverse coupling issues. Although the systems were not large flexible spacecraft, the mass of the hub was still much greater than the mass of the appendage. Also, the hub was fixed in translation which further limited the center of mass to small variations. Simulation and comparison studies done by Guo-Ping show that even small tip masses may affect dynamic characteristics of the system significantly, which may result in the largening of vibrating amplitude and the descending of vibrating frequency of the beam, and may affect end position of the hub-beam system as well[32]. While the efforts are closer to the approach provided within this research document, they only looked at single-input

single-output systems.

A recent study which uses finite element methods similar those presented within this document was done by LoBosco in his modeling of a large optical telescope used to find terrestrial planets in other solar systems[132]. The optical telescope modeled was a large flexible structure constructed from cantilever beams. A concern identified in the results of the study pertained to how extremely sensitive the optical performance was to truss uncertainties. It was presented the cause of the sensitivity rests within the reaction wheel assembly broadband disturbance and further study in this area was identified. The error may lie in the fact that cantilever mode shapes were used in the model instead of free-free mode shapes. While the optical telescope has typical characteristics of a large flexible structure, it's highly precise performance requirements may be better met if a modeling approach mirroring the techniques presented within this document were adopted.

Given the small flexible nature of the system modeled in this research effort, and the areas of concern identified from previous researchers in the area of flexible spacecraft control, the FEM analysis outlined in Section 2.2 was modified for the free-free assumption. Material properties were kept the same and the free-free analysis generated eighteen mode shapes. The applicable modes and the frequencies at which they occur are listed in Table 2.6 while plots of the first three bending modes and the torsional mode are provided in Figures 2.13-2.16.

All of the resonant modes for the free-free condition occur at similar frequencies as those of the cantilever modes except for the first bending mode. Where the first bending mode of the cantilever appendage occurs at 0.3947 Hz, the first bending mode of the free-free appendage is almost an order of magnitude higher at 3.1518 Hz. Therefore, each assumption will generate differing mode shape matrices.

Table 2.6: Free-Free Resonant Frequencies From FEM Analysis

Mode Shape	Frequency (Hz)
1 st Bending in Y direction	3.1518
1 st Bending in X direction	3.1518
1 st Torsional Mode	8.0284
2 nd Bending in Y direction	12.588
2 nd Bending in X direction	12.588
3 rd Bending in Y direction	29.491
3 rd Bending in X direction	29.491
1 st Compression Mode	55.555
4 th Bending in Y direction	61.690
4 th Bending in X direction	61.690
5 th Bending in Y direction	115.70
5 th Bending in X direction	115.70
6 th Bending in Y direction	188.62
6 th Bending in X direction	188.62
7 th Bending in Y direction	279.30
7 th Bending in X direction	279.30
8 th Bending in Y direction	386.99
8 th Bending in X direction	386.99

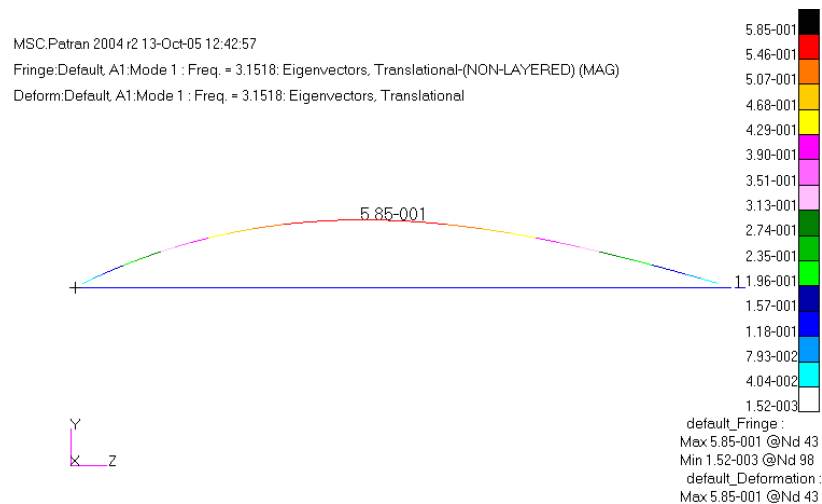


Figure 2.13: First Bending Mode For Free-Free Conditions

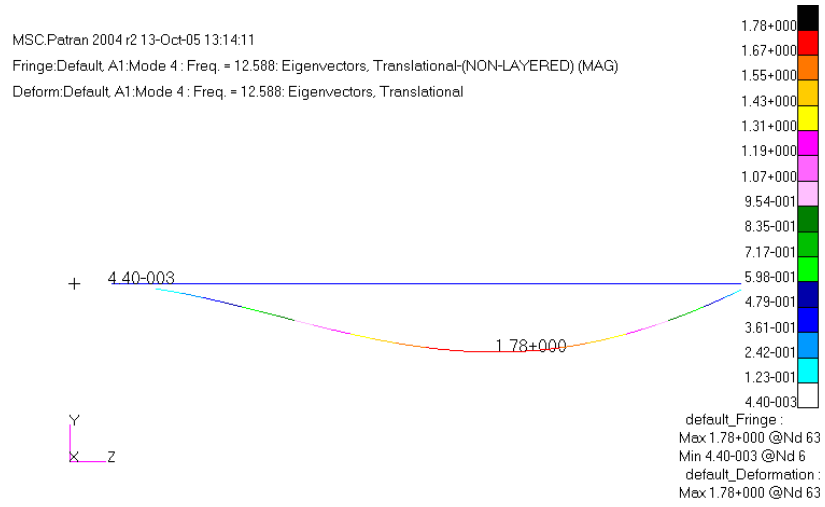


Figure 2.14: Second Bending Mode For Free-Free Conditions

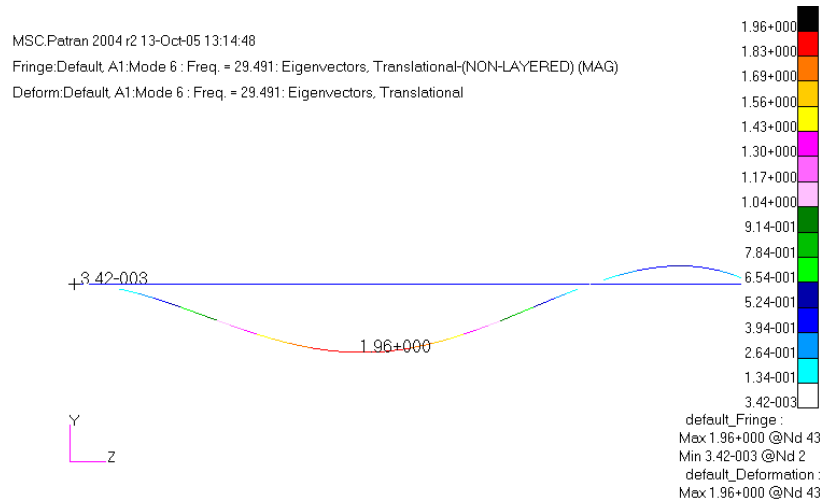


Figure 2.15: Third Bending Mode For Free-Free Conditions

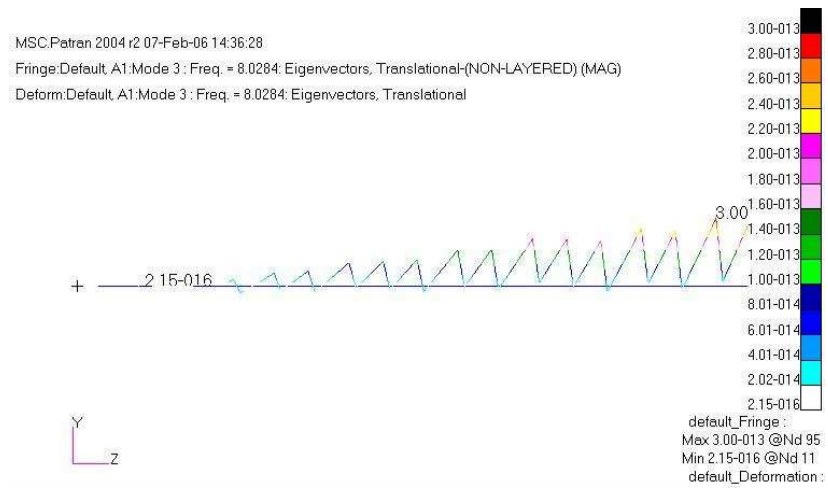


Figure 2.16: First Torsional Mode For Free-Free Conditions

2.3 State Space Form of Nominal System Model

The FEM analysis output is a powerful solution to producing the equations of motion for a small flexible spacecraft using free-free mode shapes. To illustrate this, consider a spacecraft using the material properties shown in Section 2.2 where the FEM model is comprised of 101 nodes with the controlling body treated as a lumped mass located at node 1 and the tip mass is a lumped mass located at node 101. Each node is free to both translate and rotate such that the state vector, x , takes a similar form as Eq. 2.25 but is for 101 nodes instead of 3. Since each node has 6 degrees of freedom, the dimensions of x is (606×1) .

The harmonic equation shown in Eq. 2.21 is now written as

$$[m]\ddot{x} + [k]x = F \quad (2.44)$$

where $[m]$ and $[k]$ are the mass and stiffness coefficients coupling each node and F is the matrix of external forces applied to the system.

The state space representation of Eq. 2.44 requires a set of first order equations. This is done in the following manner:

$$\begin{aligned} \ddot{x} + [m]^{-1}[k]x &= [m]^{-1}F \\ \ddot{x} &= -[m]^{-1}[k]x + [m]^{-1}F \end{aligned} \quad (2.45)$$

let

$$\begin{aligned} z_1 &= x \\ \dot{z}_1 &= \dot{x} \\ z_2 &= \dot{z}_1 \\ \dot{z}_2 &= -[m]^{-1}[k]z_1 + [m]^{-1}F \end{aligned} \quad (2.46)$$

then

$$\begin{pmatrix} \dot{z}_1 \\ \dot{z}_2 \end{pmatrix} = \begin{pmatrix} 0 & I \\ -[m]^{-1}[k] & 0 \end{pmatrix} \begin{pmatrix} z_1 \\ z_2 \end{pmatrix} + \begin{pmatrix} 0 \\ m^{-1}F \end{pmatrix} \quad (2.47)$$

For this system model, F is the control torque moments acting on the controlling body located at node 1. Since there are three independent reaction wheels providing the control input, F takes the form

$$F = \begin{pmatrix} 0_{3 \times 3} \\ I_{3 \times 3} \\ 0_{600 \times 3} \end{pmatrix} u \quad (2.48)$$

Attitude measurements for this system are the rotational orientations of the controlling body and is represented as

$$y = Cz \quad (2.49)$$

where

$$C = [0_{3 \times 3} I_{3 \times 3} 0_{3 \times 600} 0_{3 \times 606}] \quad (2.50)$$

since the measurements are the displacement rotations with no rate measurements.

Now, the state space representation of the system using physical coordinates, x , can become overwhelming depending on the number of nodes used in the FEM. For this case, the plant matrix, A , has dimensions (1212×1212) . Computer processing capacity may be of little concern when using the latest desktop technology, but such luxury is typically not available to small satellites. Therefore, the modal approach, shown in Eq. 2.22 and Eq. 2.23, is desirable due to a reduced number of states and is written as

$$\ddot{\eta} + \bar{D}\dot{\eta} + \bar{K}\eta = \bar{F} \quad (2.51)$$

where the bar denotes a generalized matrix in modal equations, structural damping is included in the form

$$\bar{D} = 2\zeta\sqrt{\bar{K}} \quad (2.52)$$

and the modal forces produced by controller inputs are

$$\bar{F} = [\phi]^T F \quad (2.53)$$

The same development of Eq. 2.47 is applied to Eq. 2.51 to generate the state space representation of the modal equations.

$$\begin{pmatrix} \dot{\bar{z}}_1 \\ \dot{\bar{z}}_2 \end{pmatrix} = \begin{pmatrix} 0 & I \\ -\bar{K} & -\bar{D} \end{pmatrix} \begin{pmatrix} \bar{z}_1 \\ \bar{z}_2 \end{pmatrix} + \begin{pmatrix} 0 \\ \bar{F} \end{pmatrix} \quad (2.54)$$

and

$$\bar{y} = C[\phi]\bar{z} \quad (2.55)$$

Consider what occurs when this approach is applied to cantilever boundary conditions. The modal force vector, with momentum actuators placed only at the controlling body, takes the form

$$\begin{aligned} \bar{F} &= [\phi]^T F \\ &= \begin{pmatrix} N1T1MS1 & N1T2MS1 & \vdots & NnR3MS1 \\ N1T1MS2 & & & \\ \vdots & & \ddots & \vdots \\ N1T1MSm & & \vdots & NnR3MSm \end{pmatrix} \begin{pmatrix} 0 & 0 & 0 \\ 0 & 0 & 0 \\ 0 & 0 & 0 \\ 1 & 0 & 0 \\ 0 & 1 & 0 \\ 0 & 0 & 1 \\ 0 & 0 & 0 \\ \vdots \\ 0 & 0 & 0 \end{pmatrix} \\ &= \begin{pmatrix} N1R1MS1 & N1R2MS1 & N1R3MS1 \\ N1R1MS2 & N1R2MS2 & N1R3MS2 \\ \vdots & \vdots & \vdots \\ N1R1MSm & N1R2MSm & N1R3MSm \end{pmatrix} \end{aligned} \quad (2.56)$$

For the restrained system using cantilever mode shapes, as used extensively in the literature, the boundary conditions applied to the first node constrain both translation

and rotation. This means there is no rotation of node 1 and

$$\bar{F} = \begin{bmatrix} 0 \end{bmatrix} \quad (2.57)$$

Thus, for the cantilever assumption, the described method will generate linearly independent modal equations but with no controlling forces. This is perhaps why the analytical solutions presented in the literature, those originally derived from Likins, all assume cantilever modes; which is a valid assumption for cases where the system center of mass is located at the center of mass of the controlling body and moves very slightly from that location over time as seen with large space structures or symmetric spacecraft.

Recall, the dimensions of A from Eq. 2.47 is (1212×1212) . Now, the size of \bar{A} is dependent on the number of mode shapes included in the system model. There are an infinite number of mode shapes which can be generated for a flexible system. It is impossible to include all of the mode shapes since the accuracy which Patran can determine these mode shapes degrades at higher frequencies and the mode shape matrix, $[\phi]$, no longer is orthonormalized if the number of modes exceeds the number of nodes used in the FEM. A control designer can use the following technique to determine how many mode shapes to include in the nominal plant model.

The higher the frequency of a mode shape, the smaller the energy which is stored in that shape. Harmonic motion of the flexible structure will subject the controlling body to harmonic excitation. The nondimensional ratio, $\frac{F_{tr}}{F_0}$, is a measure of the force transmitted to the controlling body and is written as[147]

$$\frac{F_{tr}}{F_0} = [1 + (\frac{2\zeta\omega}{\omega_n})^2]^{\frac{1}{2}} |G(i\omega)| \quad (2.58)$$

where ζ is the viscous damping factor, ω is the excitation frequency, ω_n is the natural frequency of undamped oscillation, and $|G(i\omega)|$ is the magnitude of the system's frequency response. For higher frequency resonant modes, the force transmitted to the controlling body decreases. In addition, the gain of a stable system drops off at frequencies higher

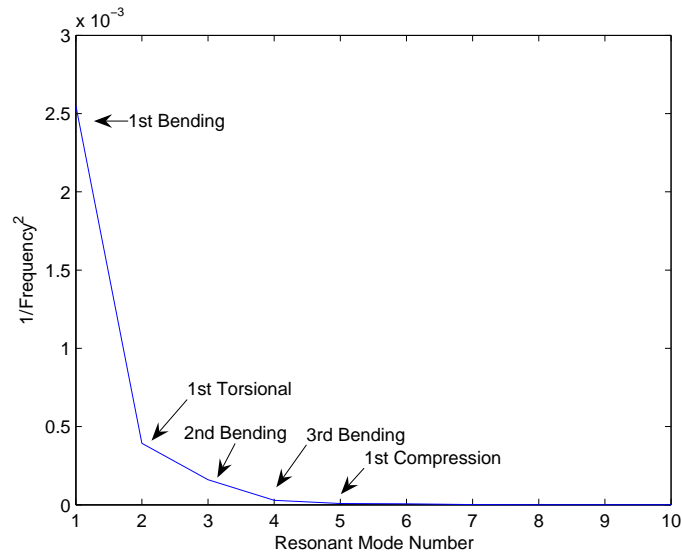


Figure 2.17: Nondimensionalized Resonant Transmission Forces

than the control dynamics of the closed loop system.

Using the free-free resonant frequencies listed in Table 2.6, a plot is created of $\frac{1}{\omega_n^2}$ versus the resonant mode number where each mode number represents each mode shape, with both bending modes in the x and y direction receiving one number instead of two separate numbers (see Figure 2.17).

Resonant modes beyond the fourth bending mode will be excluded from the nominal model because the slope of the plot approaches zero beyond that point which indicates the amount of force transmitted at higher frequencies are indistinguishable from one another. Table 2.7 lists the resonant modes generated in the FEM analysis, which are used to build the nominal system model. These modes lead to a modal \bar{A} matrix of dimensions (32×32) , which is 2.6% the size of the plant matrix generated using physical coordinates.

Table 2.7: Free-Free Resonant Frequencies for Nominal Model

Mode Shape	Frequency (Hz)
Low Frequency Mode	8.3781×10^{-7}
Low Frequency Mode	3.2062×10^{-6}
Low Frequency Mode	3.9299×10^{-6}
Low Frequency Mode	1.0974×10^{-5}
Low Frequency Mode	1.2097×10^{-5}
Low Frequency Mode	1.2959×10^{-5}
1 st Bending in Y direction	3.1518
1 st Bending in X direction	3.1518
1 st Torsional Mode	8.0284
2 nd Bending in Y direction	12.588
2 nd Bending in X direction	12.588
3 rd Bending in Y direction	29.491
3 rd Bending in X direction	29.491
1 st Compression Mode	55.555
4 th Bending in Y direction	61.690
4 th Bending in X direction	61.690

Chapter 3

Attitude Control of Small Flexible Structures

3.1 Control Bandwidth

The normal mode solution of the FEM model generates modal information for all resonant modes of the flexible structure. While all of this information is used in creating the nominal model of the system, the design model may have fewer resonant modes included. The stability and robustness of an optimal controller may be used by designers to determine which modes to include (see Section 3.3). Knowledge of the proximity of resonant modes near the controller bandwidth is also an important consideration. The mode frequencies near the bandwidth of the satellite's attitude control system will have a larger impact on control authority than the higher frequency modes. According to some designers, the lowest natural frequencies of flexible components should be at least an order of magnitude greater than the rigid-body frequencies before flexibility can be neglected[3]. This simplification of design is only valid in models based on assumed cantilever boundary conditions and has not been validated for system's using free-free boundary conditions.

The controller bandwidth defines the frequency where the control authority begins to diminish. Attitude control and disturbance rejection are effective from DC up to the bandwidth[235] and high accuracy implies high position gain and high bandwidth. However, increasing bandwidth may cause bending resonances to affect control system performance by producing large output errors due to measurement noise.

Control designers can estimate controller closed loop bandwidth with the following equation:

$$\omega_{BW} = \sqrt{\frac{K_p}{I}} \quad (3.1)$$

where K_p is the position gain of the controller and I is the spacecraft's moment of inertia. The position gain can be estimated and must be high enough to provide the required attitude control pointing accuracy in the presence of disturbance torques. The units of K_p can either be $\frac{Nm}{deg}$ or $\frac{Nm}{rad}$ and is determined by

$$K_p \geq \frac{T_D}{\theta_\epsilon} \quad (3.2)$$

where T_D is the peak disturbance torque and θ_ϵ is allowable attitude error.

Four environmental disturbance torques are commonly considered when determining the peak disturbance torque. These were the gravity gradient, T_g , solar radiation pressure, T_{sp} , magnetic field, T_m , and aerodynamic torques, T_a . The equations used to calculate these disturbance torques are:

$$T_g = \frac{3\mu}{2R^3} |I_z - I_y| \sin(2\theta) \quad (3.3)$$

where T_g is the max gravity torque, μ is the Earth's gravitational constant ($3.986 \times 10^{14} \frac{m^3}{s^2}$), R is the orbit radius (m), θ is the maximum deviation of the Z-axis from local vertical in radians, and I_z and I_y are the moments of inertia about z and y (or x, if smaller) axes in kgm^2 . The solar radiation pressure can be represented as

$$T_{sp} = F(c_{ps} - c_g) \quad (3.4)$$

where

$$F = \frac{F_s}{c} A_s (1 + q) \cos i \quad (3.5)$$

and F_s is the solar constant, $1,367 \frac{W}{m^2}$, c is the speed of light, $3 \times 10^8 \frac{m}{s}$, A_s is the surface area (m^2), c_{ps} is the location of the center of solar pressure (m), c_g is the center of

Table 3.1: Typical Disturbance Torques for LEO Small Satellites

Disturbance Torque	Worst Case Magnitude
Magnetic Torque ($D = 1.0$)	5.1468×10^{-5}
Gravity Gradient Torque ($I_y - I_z = 139.3$)	4.3686×10^{-5}
Drag Torque ($c_{pa} - c_g = 3cm$)	3.489×10^{-6}
Solar Pressure Torque ($c_{ps} - c_g = 3cm$)	0.02205×10^{-6}

gravity (m), q is the reflectance factor, and i is the angle of incidence of the Sun. The magnetic field torque on the spacecraft is

$$T_m = DB \quad (3.6)$$

where D is the residual dipole of the vehicle (Am^2) and B is the Earth's magnetic field in tesla. B can be approximated as $\frac{2M}{R^3}$ for a polar orbit to half that at the equator. M is the magnetic moment of the Earth, $7.96 \times 10^{15} \text{tesla} \cdot m^3$, and R is the radius from the dipole center to the spacecraft in m .

Finally, the aerodynamic drag on the satellite can be written as

$$T_a = F(c_{pa} - c_g) \quad (3.7)$$

where $F = 0.5\rho C_d AV^2$, C_d is the drag coefficient, ρ is atmospheric density ($\frac{kg}{m^3}$), A is the surface area (m), V is the spacecraft velocity ($\frac{m}{sec}$), c_{pa} is the center of aerodynamic pressure (m), and c_g is the center of gravity (m).

For a typical Low Earth Orbit (LEO) small satellite with a deployed appendage, the worst case magnitude for these environmental disturbance torques are calculated and listed in Table 3.1[231]:

The peak disturbance torque, T_D , used in Eq. 3.2 would be if all of the environmental disturbance torques were acting at the same time in resonance. Assuming $T_D = 1 \times 10^{-4}$ and a attitude pointing accuracy requirement, $\theta_\epsilon = 0.1^\circ$, the controller

closed loop bandwidth would be $\omega_{BW} = 0.45\text{Hz}$. As the altitude of small satellites decrease, an increase in atmospheric drag occurs. If the same satellite is placed in an altitude comparable to that of the space shuttle, the atmospheric density becomes approximately two orders of magnitude larger. This will cause the drag disturbance torque to be approximately $2 \times 10^{-4} Nm$ and the control bandwidth to approximately equal 0.7Hz . The flexible nature of the satellite system further complicates the determination of a specific value for control bandwidth as the center of mass of the system relative to the center of pressure is continuously changing.

3.2 LQG/LTR

Linear Quadratic Regulator (LQR) control leads to linear control laws that are easy to implement and analyze. The system being controlled is assumed to be at equilibrium and it is desired to maintain the equilibrium despite disturbances.

3.2.1 Linear Quadratic Regulator (LQR)

If a system is represented as

$$\begin{aligned}\dot{x} &= Ax + Bu \\ y &= Cx\end{aligned}\tag{3.8}$$

a cost function can be defined as

$$J = \frac{1}{2} \int_0^T (x'Qx + u'Ru)dt\tag{3.9}$$

where J is minimized with respect to the control input $u(t)$.

J represents the weighted sum of energy of the state and control. Q and R are weighting matrices, or design parameters, where the state-cost matrix, Q , weights the states while the performance index matrix, R , weights the control effort. If Q is increased while R remains constant, the settling time will be reduced as the states approach zero

at a faster rate. This means that more importance is being placed on keeping the states small at the expense of increased control effort. If R is very large relative to Q , the control energy is penalized very heavily. This physically translates to smaller motors, actuators, and amplified gains needed to implement the control law.

Pontriagin's minimum principle is used to solve the optimal control problem. First, from the Hamiltonian

$$H(x, \lambda, t) = \frac{1}{2}(x'Qx + u'Ru) + \lambda'(Ax + Bu) \quad (3.10)$$

the minimum principle states that the optimal control and state trajectories must satisfy the following three equations:

$$\begin{aligned} \dot{x} &= \frac{\partial H}{\partial \lambda} \\ -\dot{\lambda} &= \frac{\partial H}{\partial x} \\ \frac{\partial H}{\partial u} &= 0 \end{aligned} \quad (3.11)$$

where $x(0) = x_0$ are the state equations and $\lambda(T) = 0$ are the costate or adjoint equations.

When Eqs. 3.8-3.11 are applied, the equations become

$$\begin{aligned} \dot{x} &= Ax + Bu \\ -\dot{\lambda} &= Qx + A'\lambda \\ u^* &= -R^{-1}B'\lambda \end{aligned} \quad (3.12)$$

where u^* is the optimal control and R has to be positive definite for its inverse to exist. The above coupled linear differential equations form a two point boundary value problem (TPBVP), which, because of mixed boundary conditions, is difficult to solve numerically. Substituting the optimal control into the state equation produces

$$\begin{pmatrix} \dot{x} \\ \dot{\lambda} \end{pmatrix} = \begin{pmatrix} A & -BR^{-1}B' \\ -Q & -A' \end{pmatrix} \begin{pmatrix} x \\ \lambda \end{pmatrix} \quad (3.13)$$

where the matrix on the right hand side is known as the Hamiltonian matrix, H , and plays an important role in LQR theory. If the following substitution is made, the TPBVP doesn't have to be solved:

$$\lambda = Px \quad (3.14)$$

Differentiating both sides of Eq. 3.14 with respect to time, substituting in for λ and \dot{x} (from Eq. 3.13), we get

$$\begin{aligned} \frac{d\lambda}{dt} &= \frac{dP}{dt}x + P\frac{dx}{dt} \\ &= \frac{dP}{dt}x + PAx - PBR^{-1}B'Px \end{aligned} \quad (3.15)$$

and inserting $\dot{\lambda}$ from Eq. 3.12

$$-Qx - A'Px = \frac{dP}{dt}x + PAx - PBR^{-1}B'Px \quad (3.16)$$

Eq. 3.16 must hold true for any x , so a sufficient condition for optimal control is that P must satisfy

$$-\frac{dP}{dt} = Q + A'P + PA - PBR^{-1}B'P \quad (3.17)$$

Eq. 3.17 is known as the Riccati differential equation. It is a nonlinear first order differential equation that has to be solved backwards in time. The above formulation and solution of the LQR problem is known as the finite time problem. It results in a linear time varying controller of the feedback form

$$u(t) = -K(t)x(t) \quad (3.18)$$

where $K(t) = R^{-1}B'P(t)$.

For the infinite time LQR problem, we let t approach infinity. Of course, now one runs into the question of the convergence of the cost function and the existence of the optimal controller. Even if the optimal control exists, it does not necessarily result in a stable closed loop system. It turns out that under mild conditions, $P(t)$ approaches a

constant matrix P ($\frac{dP}{dt} \rightarrow 0$) and the positive definite solution of the algebraic Riccati equation results in an asymptotically stable closed loop system.

$$\begin{aligned} Q + A'P + PA - PBR^{-1}B'P &= 0 \\ u &= -Kx \\ K &= R^{-1}B'P \end{aligned} \tag{3.19}$$

The exact conditions for the above to hold are the following. The pair (A,B) are stabilizable, $R > 0$, and Q can be factored as $Q = C'_q C_q$, where C_q is any matrix such that (C_q, A) is detectable. Stabilizable refers to the uncontrollable portions being asymptotically stable while detectable refers to the unobservable portions being asymptotically stable. These conditions are necessary and sufficient for existence and uniqueness of an optimal controller that will asymptotically stabilize the system.

If one is interested in controlling a subset of the states, the system outputs for this example, the cost function, J, can be written as

$$\begin{aligned} J &= \frac{1}{2} \int_0^\infty (y'Qy + u'Ru)dt \\ &= \frac{1}{2} \int_0^\infty (x'C'QCx + u'Ru)dt \end{aligned} \tag{3.20}$$

and the Hamiltonian takes the form

$$H = \begin{pmatrix} A & -BR^{-1}B' \\ -C'QC & -A' \end{pmatrix} \tag{3.21}$$

An interesting thing to note is the 2n eigenvalues of H are symmetric about both the imaginary axis and the real axis. Thus, the adjointed system has n stable roots and n unstable roots; half associated with x and the other half associated with λ . For the cost function, J, to remain finite, the n stable eigenvalues of H must be the closed loop poles of the system. When we optimize a controllable linear system using a quadratic cost, we will always generate a stable closed-loop system.

3.2.2 Optimal Estimation (Kalman Filter)

The LQR solution is basically a state feedback type of control meaning it requires that all states be available for feedback. This is usually unreasonable and some form of state estimation is necessary. The combination of the state feedback and observer will always result in a stable closed-loop system. Controller performance can be optimized according to some quadratic cost function (LQR). Observer design can also be done in an optimal manner provided the problem is formulated in a probabilistic (or stochastic) sense. The formulation of the state estimation problem is as follows:

$$\begin{aligned}\dot{x} &= Ax + Bu + \omega \\ y &= Cx + \nu\end{aligned}\tag{3.22}$$

where ω represents random noise disturbance input (process noise) and ν represents random measurement (sensor) noise.

It is assumed that both noise processes are unbiased white Gaussian zero-mean stationary processes with known covariances given below.

$$\begin{aligned}E\{\omega(t)\} &= 0 \\ E\{\nu(t)\} &= 0 \\ E\{\omega(t)\omega(t+\tau)'\} &= Q_0\delta(t-\tau) \\ E\{\nu(t)\nu(t+\tau)'\} &= R_0\delta(t-\tau) \\ E\{\omega(t)\nu(t+\tau)'\} &= 0\end{aligned}\tag{3.23}$$

The state-space solution to this problem was first introduced by R. E. Kalman and R. S. Bucy. It obtains an estimate of $x(t)$ based on noise-corrupted measurements such that the variance of the error is minimized. The optimal estimator is given by

$$\dot{\hat{x}} = A\hat{x} + Bu + L(y - C\hat{x})\tag{3.24}$$

where \hat{x} is the estimate of x . The observer gain is computed from

$$L = \Sigma C' R_0^{-1} \quad (3.25)$$

and Σ is found as the positive semi-definite solution of

$$A\Sigma + \Sigma A' + Q_0 - \Sigma C' R_0^{-1} C \Sigma = 0 \quad (3.26)$$

Note that the equations for the filter gain, L , and Σ are very similar to the equations for the LQR solution. In particular, the equation for Σ is an algebraic Riccati equation and is the estimation error covariance and the trace of Σ indicates how well the filter is performing. The Q_0 and R_0 matrices represent the intensity of the process and sensor noise inputs and are the only parameters that are to be provided by the user.

3.2.3 Linear Quadratic Gaussian (LQG)

The LQG combines the LQR with the Kalman filter. Consider the plant equations

$$\begin{aligned} \dot{x} &= Ax + Bu + \omega \\ y &= Cx + \nu \end{aligned} \quad (3.27)$$

with controller

$$\begin{aligned} u &= -K\hat{x} \\ K &= R^{-1}B'P \\ 0 &= A'P + PA + Q - PBR^{-1}B'P \end{aligned} \quad (3.28)$$

and observer

$$\begin{aligned} \dot{\hat{x}} &= A\hat{x} + Bu + L(y - C\hat{x}) \\ L &= \Sigma C' R_0^{-1} \\ 0 &= A\Sigma + \Sigma A' + Q_0 - \Sigma C' R_0^{-1} C \Sigma \end{aligned} \quad (3.29)$$

The LQR results in an asymptotically stable closed loop system. In addition, the controller minimizes the average of the LQR cost function (weighted variance of the state and input)

$$J = \frac{1}{2} \int_0^{\infty} (x'Qx + u'Ru)dt \quad (3.30)$$

producing an optimal solution.

The transfer function of the LQG compensator is similar to the observer-based compensator, and is given by

$$H(s) = K(sI - A + BK + LC)^{-1}L \quad (3.31)$$

An important thing to note is that LQG has no guaranteed stability margins like those produce by LQR. In fact, its margins can be dangerously low. By changing the design parameters Q, R, and the noise intensities, it is observed that some parameters can have drastic effects on the system properties.

3.2.4 Loop Transfer Recovery (LTR)

The major problem with the LQG solution is its lack of robustness. The loop transfer recovery (LQG/LTR) technique maintains the LQG machinery but modifies the design procedure to address some of the short comings of the original LQG approach.

The open loop transfer function of the LQR is given by

$$L(s) = K\Phi(s)B \quad (3.32)$$

where $\Phi(s) = (sI - A)^{-1}$.

The open loop transfer function for LQG is likewise given by

$$L(s)_{LQG} = K(sI - A + BK + LC)^{-1}LC\Phi(s)B \quad (3.33)$$

Under the following two conditions

- (1) G_p , the system plant, is minimum-phase (i.e. it has no zero in the RHP)

$$(2) R_0 = 1 \text{ and } Q_0 = q^2 BB'$$

it can be shown that

$$\lim_{q \rightarrow \infty} L(s)_{LQG} = L(s) \quad (3.34)$$

This suggests the following procedure for design. Choose the LQR parameters (Q and R) such that the LQR loop transfer function, $L(s)$, also called the target feedback loop (TFL), has desirable time and/or frequency domain properties. Design an observer with parameters specified in (2) above. Increase the tuning parameter, q , until the resulting loop transfer function is as close as possible to the TFL while considering Bode gain, closed loop bandwidth, and control effort limitations. Because the loop transfer function of LQG approaches that of LQR, it will asymptotically recover its properties.

Loop Shaping Step

- (1) Determine the controlled variables (which may or may not be the same as the measured variables) and set $Q = C'C$ or $Q = C'_q C_q$
- (2) Convert the design specifications into a desired TFL
- (3) Vary the parameter, q , until the resulting loop transfer function is similar to the TFL. One may use the root square locus (RSL) approach here for SISO systems[212].

To accomplish the recovery step, select a scalar, q , and solve the filter Riccati equation

$$A\Sigma + \Sigma A' + q^2 BB' - \Sigma C' C \Sigma = 0 \quad (3.35)$$

and set $L = \Sigma C'$.

Increase q until the resulting loop transfer function is close to the TFL. The higher the value of q , the closer the LQG system comes to the LQR performance. It should be noted that the value of q should not be increased indefinitely because this may lead to

unreasonably large values for the controller gain. Also, because LQR has -20dB slope at high frequencies, large values of q will also recover this slow roll-off rate. Smaller values for q will tend to trade off lower stability margins with higher roll-off rates at higher frequencies.

3.3 Reduced-Order Controllers

The basic problem in controlling a flexible structure is the presence of a large number of lightly damped structural modes. Theoretically, there exist an infinite number of resonant modes. The higher the modal frequency, the smaller the energy which is contained within the mode. It isn't feasible for a numerical analysis to be conducted on a nominal system plant model which contains one thousand, or even one hundred, resonant modes. The energy of the higher frequency modes will have minimal impact on the overall dynamic response and practical limitations necessitate the use of reduced-order controllers. The initial analysis runs with Patran, shown in Section 2.3, generated 16 resonant modes.

3.3.1 Controller Robustness

The uncontrolled modes, as well as the error in the knowledge of the controlled modes, represent uncertainty. Since the number of structural modes is usually large and finite element modeling accuracy typically decreases with increasing modal frequency, the design model should contain the first few resonant modes. The remaining structural modes then constitute the plant uncertainty.

For single-input single-output systems, the relationship of stability, sensitivity reduction, disturbance attenuation and rejection to the return difference of the closed loop system has been understood for quite some time[22] [87]. Attempts at extending classical design procedures to multivariable systems concentrated on sensitivity reduction[52] and examining scalar quantities associated with the return difference matrix, which

include inverse Nyquist procedures for diagonally dominant systems[179] and characteristic loci plots[137] [136]. However, the designs may possess undetected sensitivities to simultaneous perturbations in the elements of the return difference matrix[57]. Interpretations of quantities such as gain and phase margins in each input channel which lead to invaluable design insights in the single-input single-output case do not extend to the multivariable generalizations[53].

A better understanding of stability margins for multivariable systems is found in the investigation of the norms of the inverse Nyquist matrix. The measure of stability is taken to be the magnitude of the smallest plant perturbation which causes instability and is given by an appropriate matrix norm[57]. The most commonly used norm is the 2-norm. The 2-norms of a matrix and its inverse are the largest singular value and the inverse of the smallest singular value of the matrix[63] [118]. Singular value analysis is popular because the interpretation of the smallest singular value of a matrix is the distance between the matrix and the nearest singular matrix. Since this is precisely the concept needed to determine the nearness of a stable transfer function to an unstable one, its use as a measure of stability robustness is natural.

Understanding how stability margins are represented in multivariable systems is important. However, one must also attempt to reduce the sensitivity of the closed-loop system to plant perturbations as compared to the sensitivity to the open-loop system. A sufficient condition for the return difference matrix to satisfy to achieve the desired sensitivity reduction has been developed in the form of a positive definiteness condition[110] [169] [51] [217]. This condition can be expressed as a condition on the smallest singular value of the return difference. Comparison sensitivity and maintenance of stability both seek to retain a qualitative system property of sensitivity reduction versus stability under errors in the plant model.

Both the sensitivity function,

$$S = \frac{1}{1 + G_p G_c} \quad (3.36)$$

and the complementary sensitivity function,

$$T = \frac{G_p G_c}{1 + G_p G_c} \quad (3.37)$$

of the closed-loop system play an important role in the stability robustness of the system. Stability requirements bound the outputs for all bounded disturbances and bounded reference inputs. Doyle and Stein[58] applied Nyquist encirclement counts for the function

$$\det(I + G_p G_c) \quad (3.38)$$

to multivariable systems and placed magnitude constraints to determine the robustness of the system in the face of uncertainties.

In classical SISO problems, gain and phase margins are used to characterize tolerable uncertainty. This characterization is generalized to MIMO problems as

$$G(s) + \Delta G(s) = [I + L(s)]G(s) \quad (3.39)$$

where $L(s)$ is an arbitrary stable transfer matrix with

$$\bar{\sigma}[L(j\omega)] \leq m(\omega) \quad (3.40)$$

and covers simultaneous gain, phase, and direction errors which are unknown but bounded in size. The bound $m(\omega)$ indicates the maximum normalized magnitude which the model error can attain. Stability is maintained in the presence of all possible uncertainties, Eq. 3.39 and Eq. 3.40, if and only if the complementary sensitivity function satisfies

$$\bar{\sigma}[T(j\omega)] \leq \frac{1}{m(\omega)} \quad (3.41)$$

for all ω . Then,

$$\det(I + G_p G_c + L G_p G_c) = \det(I + LT) \det(S^{-1}) > 0 \quad (3.42)$$

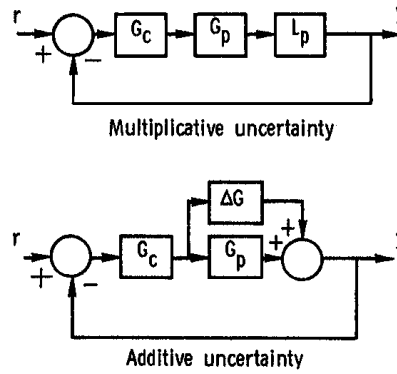


Figure 3.1: Defining Uncertainty in a Model

and the uncertainty can't change the number of encirclements in the Multivariable Nyquist Criterion. The system is stable if the unperturbed system is stable.

The loop gain condition is now written as

$$\bar{\sigma}(L)\bar{\sigma}(T) < 1 \quad (3.43)$$

to arrive at an upper bound on the magnitude of the uncertainty multiplier, L , to guarantee closed loop stability under perturbations. This condition is also necessary if all possible multivariable perturbations are allowed, since there would exist an L with

$$\bar{\sigma}(L) = \frac{1}{\bar{\sigma}(T)} \quad (3.44)$$

which brings the determinate above zero and changes the encirclement count[121].

Plant uncertainty, errors in the plant model, can be represented as either multiplicative or additive uncertainty (see Figure 3.1). The multiplicative uncertainty form is preferred in the literature on robustness because the compensated transfer function has the same uncertainty representation as the nominal model. However, since flexible structure models exhibit naturally the additive uncertainty form of the transfer function matrix, this will be used.

For the case of multiplicative uncertainty, the closed loop system is stable if

$$\bar{\sigma}[L_p(j\omega) - 1] \leq \underline{\sigma}[I + (G_p(j\omega)G_c(j\omega))^{-1}] \quad (3.45)$$

where $G_p(s)$ and $G_c(s)$ are the design model plant and compensator transfer matrices, and $\bar{\sigma}$ and $\underline{\sigma}$ denote the largest and smallest singular values. At high frequencies, assuming $\|L_p(j\omega)\| \gg 1$ and $\|G_p(j\omega)G_c(j\omega)\| \ll 1$, the above stability condition yields

$$\bar{\sigma}(G_p G_c) < \frac{1}{\bar{\sigma}(L_p)} \quad (3.46)$$

The uncertainty, or robustness, barrier is an upper bound $l_m(\omega)$ on $\bar{\sigma}(L_p)$. The system is stable in the presence of unstructured uncertainties if $\bar{\sigma}[G_p G_c] < l_m^{-1}(\omega)$ at high frequencies.

When the additive uncertainty formulation is used, a sufficient condition for stability robustness is given by [53]

$$\frac{\underline{\sigma}(I + G_p G_c)}{\bar{\sigma}(G_c)} > \bar{\sigma}(\Delta G) \quad (3.47)$$

a detailed derivation of the stability robustness conditions with associated theorems and proofs can be found in [53].

At high frequencies, assuming $\|G_p G_c\| \ll 1$, Eq. 3.47 approximately yields

$$\bar{\sigma}(G_c) < \frac{1}{\bar{\sigma}(\Delta G)} \quad (3.48)$$

that is, the compensator must roll off sufficiently rapidly at high frequencies to remain robust in the face of unmodelled/uncertain high frequency structural modes and noise. The main objective of the LQG/LTR approach is to first design a full state compensator which has the behavior of the desired loop transfer matrix (i.e. the loop gain $G_p G_c$). Therefore, any loop shaping should involve the product $G_p G_c$ rather than G_c alone as in Eq. 3.47 and Eq. 3.48. Assuming G_p is a square matrix

$$\begin{aligned} G_c &= G_p^{-1}(G_p G_c) \\ \bar{\sigma}(G_c) &\leq \bar{\sigma}(G_p^{-1})\bar{\sigma}(G_p G_c) \\ \bar{\sigma}(G_c) &\leq \underline{\sigma}^{-1}(G_p)\bar{\sigma}(G_p G_c) \end{aligned} \quad (3.49)$$

Substituting Eq. 3.49 into Eq. 3.47, the following sufficient condition for stability robustness is obtained:

$$\frac{\underline{\sigma}(I + G_p G_c) \underline{\sigma}(G_p)}{\bar{\sigma}(G_p G_c)} > \bar{\sigma}(\Delta G) \quad (3.50)$$

The performance of the closed loop system depends on the low frequency gain and the crossover frequency of the loop transfer matrix $G_p G_c$; that is the behavior of $\underline{\sigma}[G_p G_c]$. Larger low frequency gain and crossover frequency indicate better tracking performance (also shown in Section 3.1). Thus, $\underline{\sigma}[G_p G_c]$ should lie above the performance specification. The other requirement is the stability robustness in the presence of model uncertainties. If the multiplicative uncertainty formulation is used, the $\bar{\sigma}[G_p G_c]$ plot should pass under the robustness barrier $\bar{\sigma}^{-1}[L_p]$ at high frequencies. If the additive formulation is used, the robustness condition of Eq. 3.50 should be satisfied.

3.3.2 Pole-Zero Cancellation

Looking at the robustness of the controller in the presence of unmodeled higher frequency modes most often leads to lower order controllers than those that are required to control the nominal plant. This is a result of the design model being lower in order due to the inclusion of the lower frequency modes while high frequency modes are lumped into the uncertainty of the system dynamics. It may be possible to further reduce the order of the controller when pole-zero cancellation is taken into consideration.

Consider a design model where resonant modes (shown in Table 2.7) of frequencies less than 20 Hz are required to satisfy stability robustness. This will reduce the order of the controller from 32 down to 22. Since the small flexible spacecraft is a multi-input multi-output (MIMO) system using three controller inputs and measuring three angular displacements, the controller is comprised of nine transfer functions all of the order 22. This high order of the controller may be unnecessary if some of the controller poles are in close proximity to controller zeros.

There is no magic number to identify if the controller poles and zeros are within

close proximity of each other or not. Instead, a useful technique in further reducing the order of the controller is to evaluate the effect on dynamic response if some poles are allowed to cancel out with zeros in close proximity. The Matlab command `minreal`, minimal realization, is a useful tool in accomplishing pole-zero cancelation. It is a straightforward search through the poles and zeros looking for matches that are within a specified tolerance[144]. The default tolerance is $\sqrt{\text{eps}}$, where `eps` is machine precision. The tolerance value can be increased to force additional cancelations as long as the Bode plots don't deviate significantly from the unreduced controller. If there is a difference in the Bode plots, a comparison between the dynamic response of the reduced controller and the controller prior to pole-zero cancelation will indicate whether the tolerance was set too high. If the dynamic response shows little change, this may indicate that while a certain pole-zero cancelation may generate differing Bode plots, the contribution of that particular pole-zero pair is not significant enough to alter the system response drastically. Use of this technique is demonstrated in Section 3.4.

3.4 Base-Line Response

A Matlab file was created to accomplish this research. This file reads in the FEM data and generates the mode shape matrix for both the nominal and design model, as outlined in Section 2.3, as well as reading in the natural frequencies for each mode. In addition to the system parameters presented in Section 2.2.1, a damping ratio of 0.01 for the EMC material is assumed. This assumption is common for the structural material industry when experimental data is not available[41][206].

A key design consideration is the controller effort. Since the flexible system is a gravity gradient appendage for a small satellite, it will take more control effort to correct pitch and roll displacements than yaw displacements. In this case, as well as for most flexible appendages, greater control effort is required to produce the same dynamic response one would experience from a three-axis stabilized cube. The small

satellite limitations of mass, volume, and available power impact the torque produced from on board reaction wheels. The typical maximum torque produced by reaction wheels on small satellites is in the 0.02Nm to 0.3Nm range[62][111][157][251]. It is possible that in the near future more power to be made available to on-board control actuators through improved power designs and increased solar array efficiency. For this study, the maximum allowable control effort for the analysis of the system will be 3Nm.

Additionally, the mission of this small flexible spacecraft is to meet the attitude requirements of the scientific payloads presented in Appendix D. The attitude control system needs to keep these payloads pointed $\pm 5^\circ$ in the ram, or velocity, direction. This requirement applies to both yaw and pitch while no hard requirement is placed on the roll of the controlling body. Discussions with payload scientists identified a performance metric which concludes that while data is usable within 5° off nominal, the accuracy of the data degrades the further away from 0° the payloads are pointed[208].

A controller is designed, using the LQG/LTR techniques provided in Section 3.2, to optimally reach nominal pointing requirements once pitch/yaw are 5° off nominal while operating within the control effort limit of 3Nm. This initial displacement is a result of the reaction wheels periodically reaching saturation and momentum dumping is used in conjunction with despinning the wheels. The scientists are concerned with how much time is required for the payloads to go from 5° to 0° and reach a steady state such that vibrations induced by the flexible appendage have minimal impact on system dynamic response.

Initial values used for the design parameters Q and R for the LQR calculation, Q_0 and R_0 for the Kalman filter, and q for the LTR calculation are shown in Table 3.2. The design model for the initial run was set to the nominal model since the first step is to determine if the required control effort, resulting from the design parameter gains, falls within the limit of 3Nm.

A simulation was run using Simulink to plot the system response to the LQG/LTR

Table 3.2: Initial Values for Design Parameters

Design Parameter	Value
Q	$I_{n \times n}$
R	$I_{3 \times 3}$
Q_0	variance of 1
R_0	variance of 0.01
q	[1 1e2 1e4 1e6]
Max Control Effort	3Nm

controller (see Figure 3.2). While physical coordinates are easier to visualize, the controller design is based on modal coordinates because of the greatly reduced number of states. Typically, the desired attitude is set to zero while the undeformed system has some initial orientation. Initial orientation is commonly thought of in physical coordinates with some initial angular displacement. Keep in mind the form of the physical coordinates.

$$x = \begin{pmatrix} N1T1 \\ N1T2 \\ N1T3 \\ N1R1 \\ N1R2 \\ N1R3 \\ N2T1 \\ \vdots \\ NnR3 \end{pmatrix} \quad (3.51)$$

If one wanted to give an initial rotation of 5° for the undeformed system, one cannot simply set $N1R1 = 5^\circ$ because this would give an initial rotation to the first node without propagating this along the appendage. This initial rotation will translate node 2 which will translate node 3 and so on. Instead, the initial rotation is done as

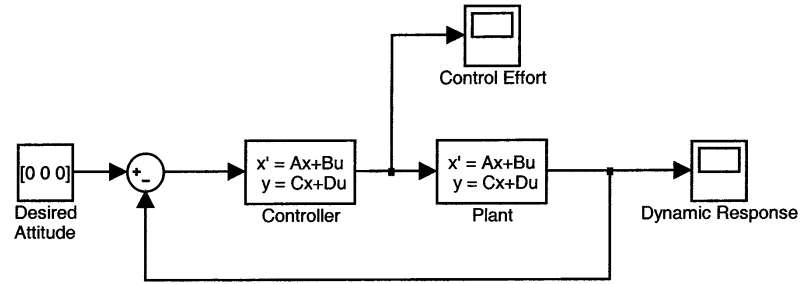


Figure 3.2: Simulink Block Diagram For Closed Loop Response

follows:

for initial roll

$$N\alpha T1 = 0$$

$$N\alpha T2 = -\Delta l \sin(N1R1)$$

$$N\alpha T3 = \Delta l \cos(N1R1) - \Delta l$$

$$N\alpha R1 = N1R1$$

$$N\alpha R2 = 0$$

$$N\alpha R3 = 0 \tag{3.52}$$

for initial pitch

$$N\alpha T1 = \Delta l \sin(N1R2)$$

$$N\alpha T2 = 0$$

$$N\alpha T3 = \Delta l \cos(N1R2) - \Delta l$$

$$N\alpha R1 = 0$$

$$N\alpha R2 = N1R2$$

$$N\alpha R3 = 0 \tag{3.53}$$

and for initial yaw

$$\begin{aligned}
 N_{\alpha T1} &= 0 \\
 N_{\alpha T2} &= 0 \\
 N_{\alpha T3} &= 0 \\
 N_{\alpha R1} &= 0 \\
 N_{\alpha R2} &= 0 \\
 N_{\alpha R3} &= N_{1R3}
 \end{aligned} \tag{3.54}$$

which is similar to the rotational kinematics presented in Appendix C where N_{α} refers to an incremental node number with a length Δl from the first node.

Since the roll and pitch axes will require more control effort, an initial angular displacement of 5° is applied to the pitch axis and the controller is trying to bring the system to a desired attitude of roll = 0° , pitch = 0° , and yaw = 0° . The simulation generates both the control effort and dynamic response for the flexible system.

The control effort, when the initial design parameters are used, is shown in Figure 3.3. The peak value of 9.77Nm exceeds the limit of 3Nm. This shows the controller is weighting the states too heavily in the LQG process while not placing enough emphasis on the control effort. Since the feedback gains are a function of the ratio between Q and R, one can either decrease Q or increase R. After an iterative modification to Q, the final design parameters listed in Table 3.3 produced the control effort shown in Figure 3.4.

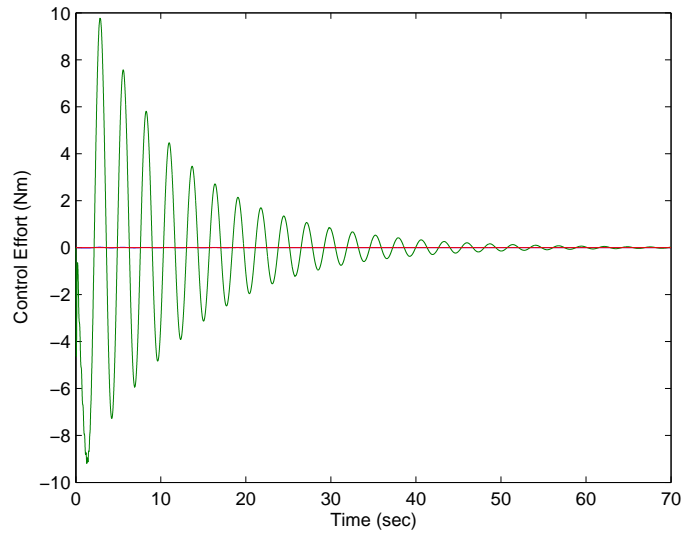


Figure 3.3: Control Effort with Initial Design Parameters

Table 3.3: Final Values for Design Parameters

Design Parameter	Value
Q	$0.01 * I_{n \times n}$
R	$I_{3 \times 3}$
Q_0	variance of 1
R_0	variance of 0.01
q	$[1 \ 1e2 \ 1e4 \ 1e6]$
Max Control Effort	3Nm

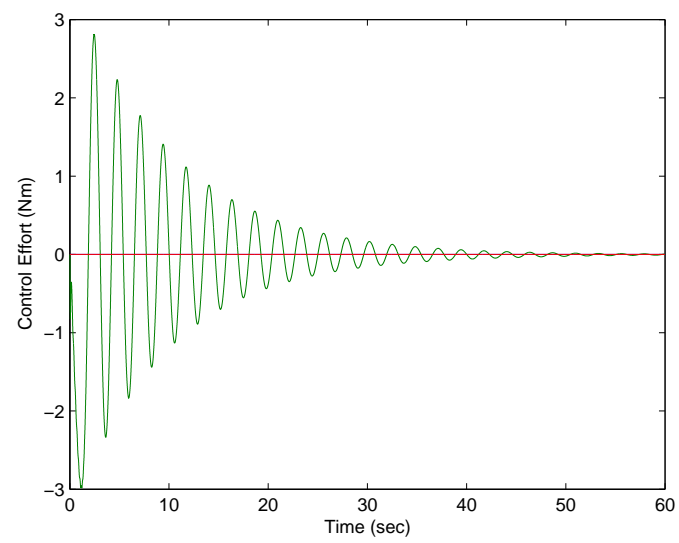


Figure 3.4: Control Effort with Final Design Parameters

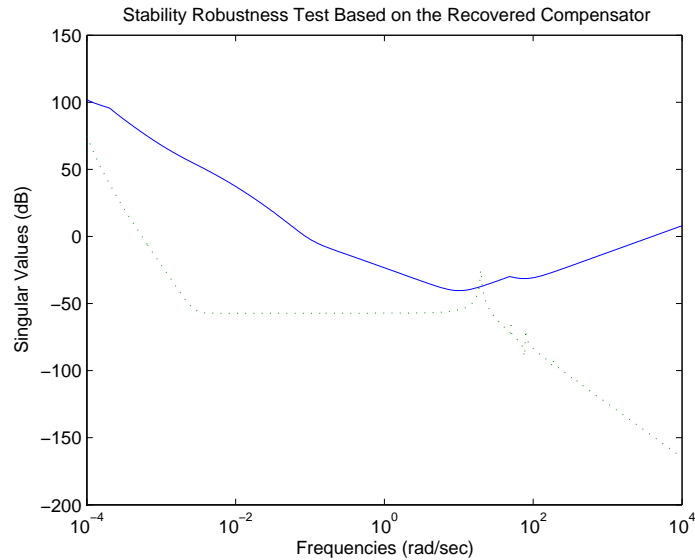


Figure 3.5: Baseline SR Test for Initial Design Model

The stability robustness test, outlined in Section 3.3.1, is evaluated to determine which resonant modes listed in Table 2.7 need to be included in the design model. The stability robustness (SR) barrier is violated if only the first six modes are retained in the design model while all of the resonant modes are placed in the uncertainty transfer matrix (see Figure 3.5). Do not confuse this design model with a rigid body model since the resonance frequencies are in the 10^{-7} to 10^{-5} Hz range and are not zero. This violation of the SR barrier occurs at the same frequency as the first bending mode.

To ensure the baseline system meets SR requirements, additional resonant modes need to be included in the design model. Figure 3.6 is a plot of the SR barrier when the first bending and torsional modes are included. This design model has a stability margin of 41 dB in the frequency region of the second bending mode. The upper curve sloping upwards indicates good tolerance of high-frequency uncertainty.

What is gained by including the second bending mode? Stability robustness can be improved if more resonant modes are included in the design model. Performance of the closed loop system depends on the low-frequency gain and crossover frequency

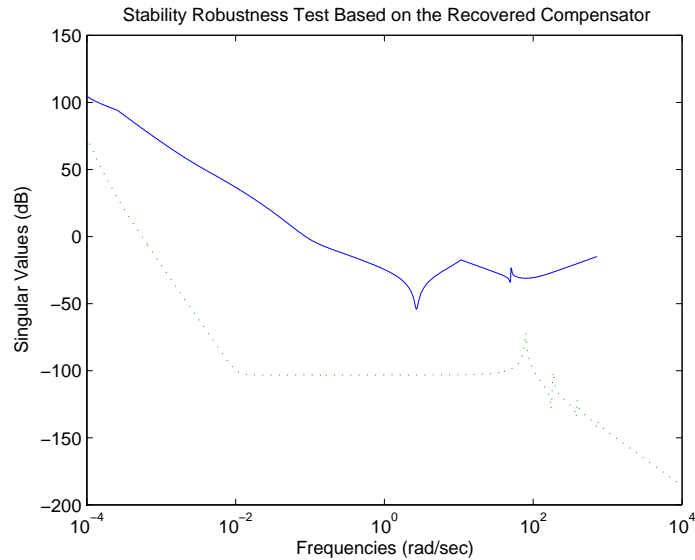


Figure 3.6: Baseline SR Test with First Bending and Torsional Modes

of the loop transfer matrix $G_p G_c$. Larger values indicate better tracking performance. Any increase in gain to improve tracking performance will decrease the stability robustness. The baseline model already takes into consideration the maximum control effort produced by the reaction wheels and an increase in bode gain will exceed this limit.

In addition to the system not being able to take advantage of an increase in control gain, the cost of needlessly adding higher frequency resonant modes may prove detrimental to onboard processor limitations. The LQG/LTR process generates a controller of the same order as the system plant. The controller for a design model containing nine resonant modes is a 3 by 3 matrix of transfer functions, each the ratio of a 17th order polynomial to a 18th order polynomial. It would require programming 333 coefficients to implement this controller. By adding the second bending modes to the design model, the order of the controller is increased to 22 and requires an additional 72 coefficients. The inclusion of the first bending mode in both the x and y directions and the first torsional mode is enough to satisfy the stability robustness of the controller and the inclusion of higher resonant modes is not required.

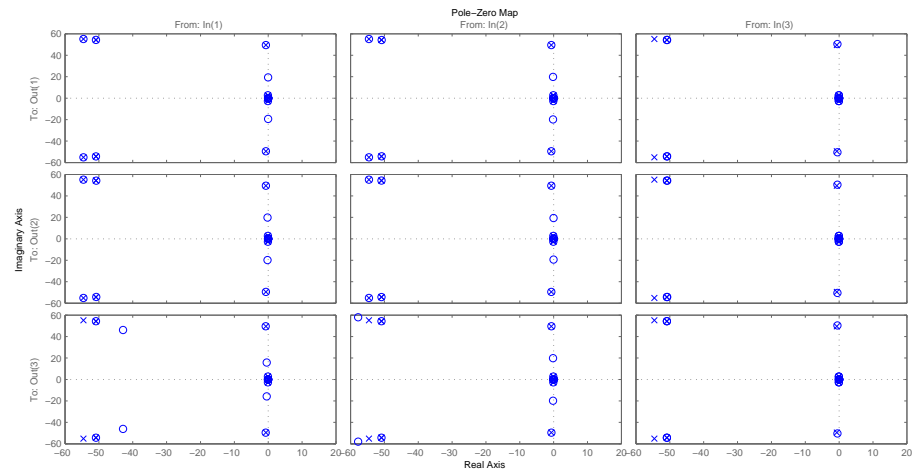


Figure 3.7: Pole-Zero Map of Each Element of the 3×3 Controller Transfer Function

Using the controller reduction technique outlined in Section 3.3.2, the number of required coefficients is greatly reduced. To illustrate the pole-zero cancellation technique, consider the pole-zero map of the controller transfer function shown in Figure 3.7. It is apparent several controller poles lie in close proximity to controller zeros. Cancellations may occur as long as the Bode plots of the reduced controllers, as well as the system dynamic response, match those of the unreduced controllers. The Bode plots of the unreduced controller are shown in Figure 3.8.

Recall that the default tolerance value for the Matlab `minreal` command is $\sqrt{\epsilon}$. It is possible to increase this tolerance and generate the same Bode plot of the reduced controller as the unreduced one. As long as the plots for both the full and reduced order controllers match up, then the dynamics of both controllers are similar. For example, consider the controllers if the default tolerance setting is used, $\sqrt{\epsilon}$, for the transfer function going from input 1 to output 1, $G_c(1,1)$. From Figure 3.9, one can see how the reduced order controller (green x's) matches up with the full order controller (red line) in both magnitude and phase, for both low and high frequencies.

One may relax the tolerance in the minimum realization until a divergence in the Bode plots is noticed. A better approach is to run a sweep of tolerance values and,

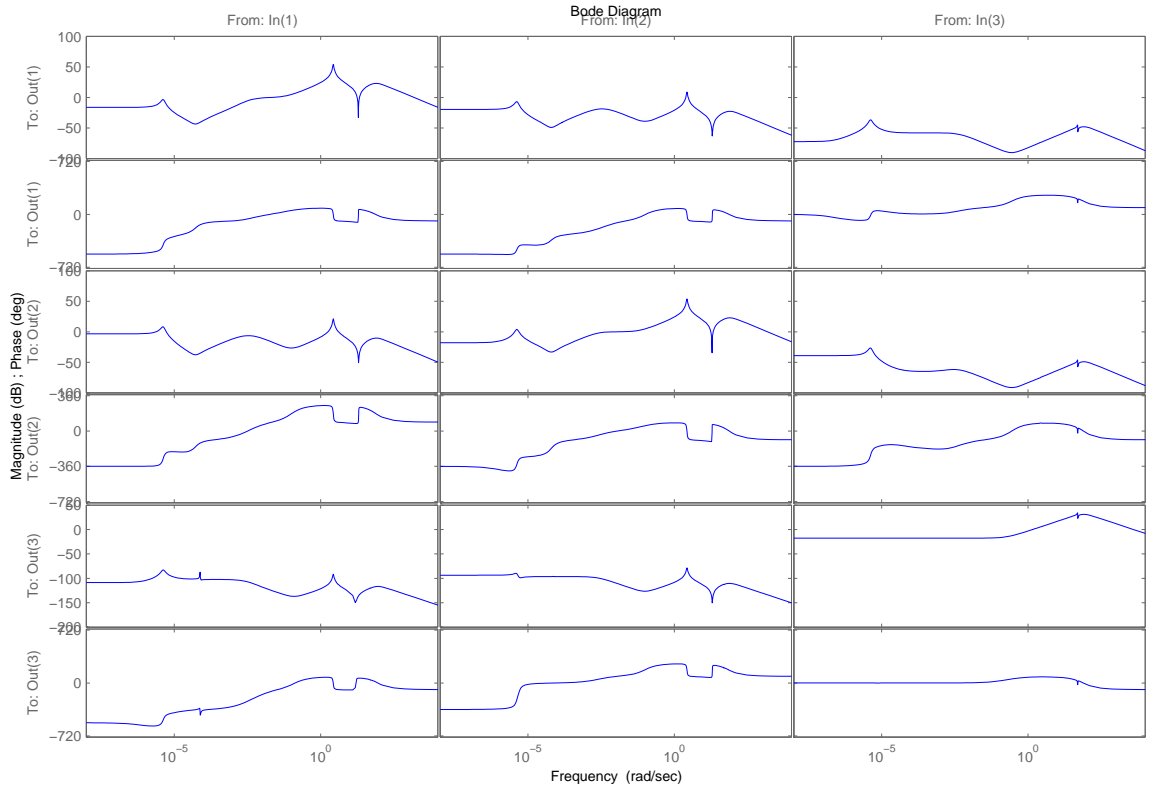


Figure 3.8: Bode Plots of Each Element of the 3x3 Controller Transfer Function

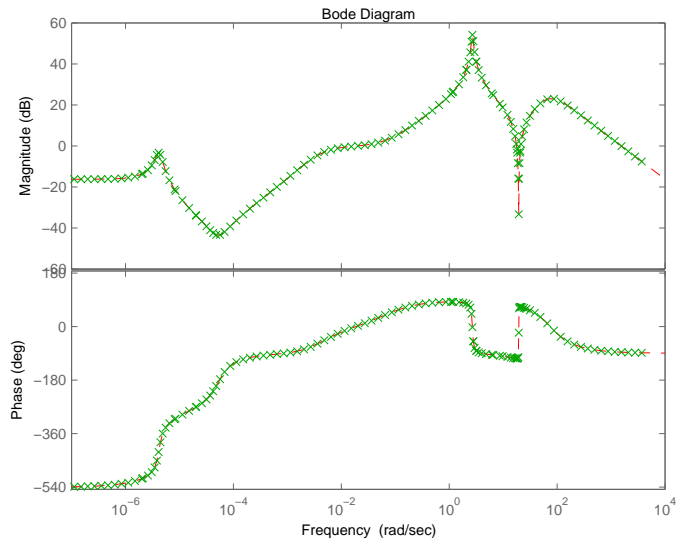


Figure 3.9: Comparison of Reduced and Full Order Controller (default tol)

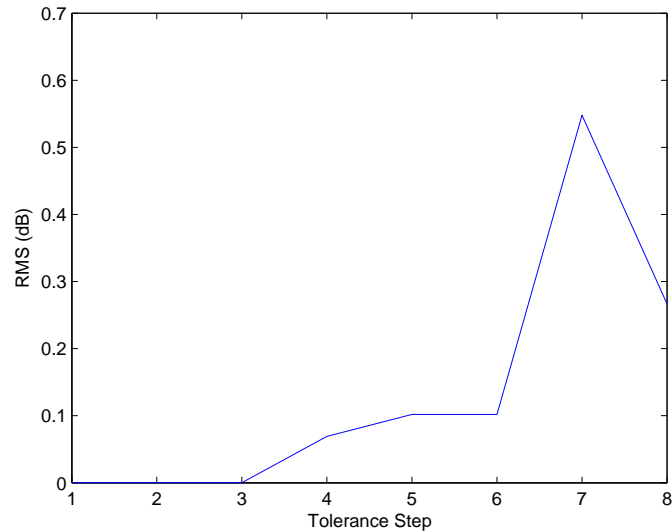


Figure 3.10: RMS of Bode Magnitude for $G_c(1,1)$

instead of visually comparing the Bode plots, calculate the RMS values and plot those values vs. the tolerance step. The tolerance is stepped from $\sqrt{\epsilon}$ to $1e-1$ in orders of magnitude such that tolerance step 1 is $\sqrt{\epsilon}$, tolerance step 2 is $1e-7$, tolerance step 3 is $1e-6$, and so on out to tolerance step 8 equalling $1e-1$. The RMS of the Bode plots are calculated for both magnitude and phase for all 9 controller transfer functions. Since the previous plot was for $G_c(1,1)$, the following two plots are the RMS plots for the same transfer function.

Looking at Figure 3.10 and Figure 3.11, a noticeable change in RMS values occurs between tolerance steps 3 and 4 ($1e-6$ and $1e-5$). This means a noticeable change in the reduced order controller dynamics occurs when additional pole-zero cancelations are performed beyond a tolerance of $1e-6$. Figure 3.12 and Figure 3.13 show the Bode comparisons for both tolerance steps.

Notice how the two Bode plots differ once the RMS is noticeable. This would lead one to believe that the tolerance limit should be set at $1e-6$. However, note how the plot in Figure 3.13 diverges at low frequencies. This is in a location where the poles and

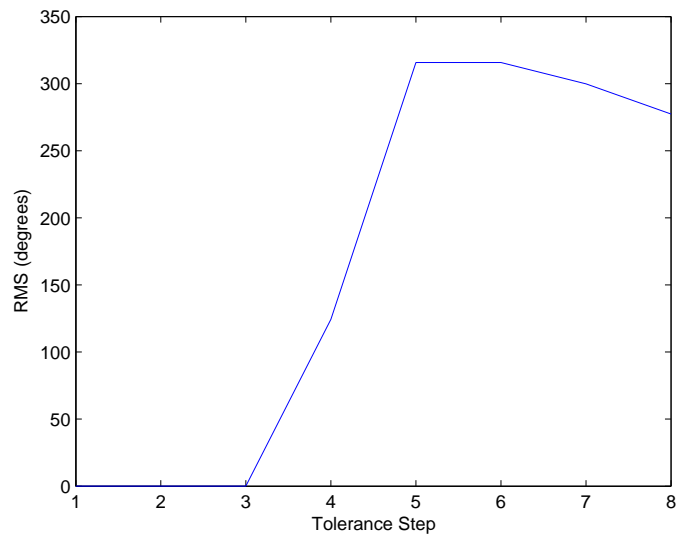


Figure 3.11: RMS of Bode Phase for Gc(1,1)

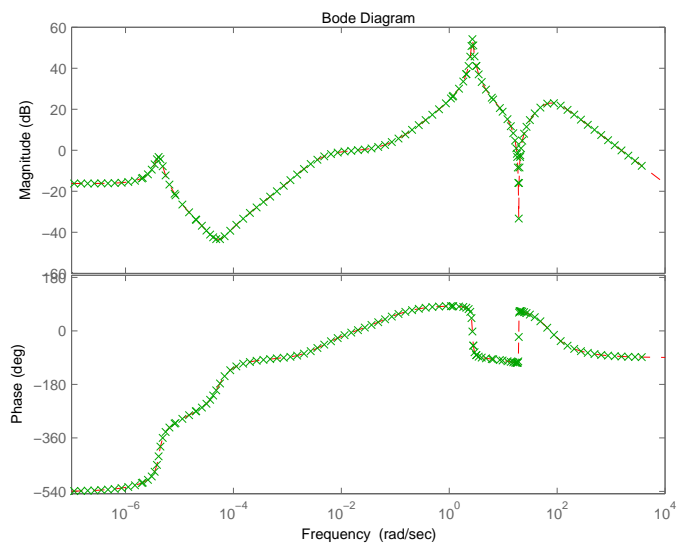


Figure 3.12: Comparison of Reduced and Full Order Controller (tol=1e-6)

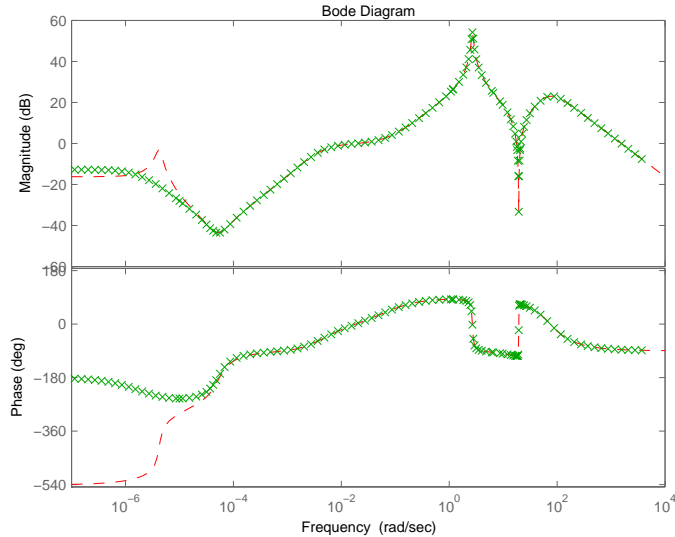


Figure 3.13: Comparison of Reduced and Full Order Controller (tol=1e-5)

zeros are in close proximity to each other and the origin of the s-plane. It is expected to see more cancelations occurring in this region than in the regions where the distance from the s-plane origin (i.e. frequency) is greater.

Looking at the simulation results of how the system responds to the reduced order controller shows no noticeable difference between tolerance step 3 or 4. Instead of visually determining this, RMS values can be calculated and plotted in the same manner as above for both control effort and dynamic response of the system. The following figures plot these RMS values.

From Figure 3.14 and Figure 3.15, a noticeable change in RMS values occurs between tolerance steps 6 and 7 ($1e-3$ and $1e-2$). A design consideration is to limit the pole-zero cancelation by using either the controller dynamics or the overall system dynamics. With the controller approach, the reduced controller closely resembles the dynamics of the full order controller. However, the cost of this approach is an increased number of coefficients required to code up the controller. If the system dynamics approach is used, a smaller number of coefficients will be needed.

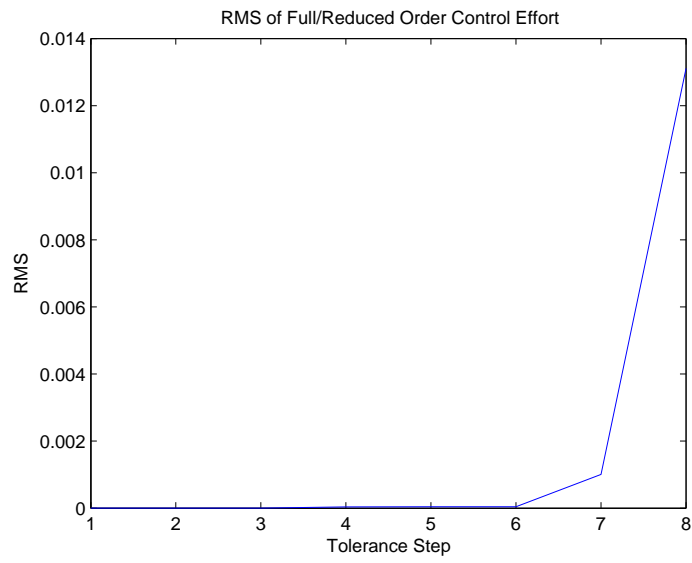


Figure 3.14: RMS of Full/Reduced Order Control Effort

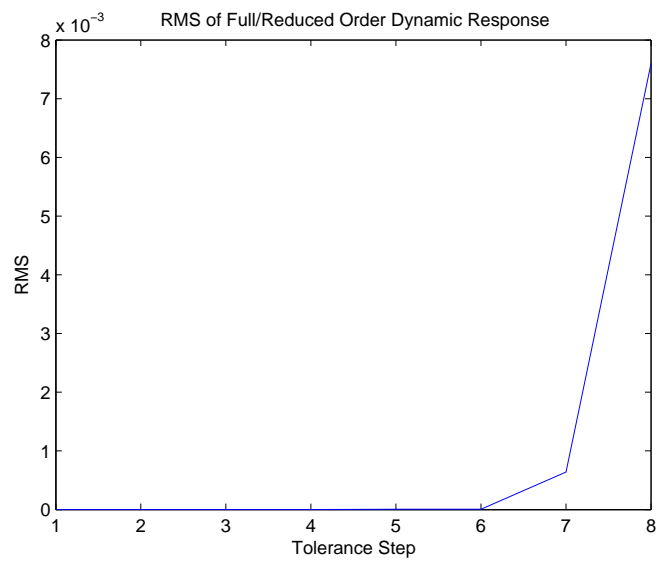


Figure 3.15: RMS of Full/Reduced Order Dynamic Response

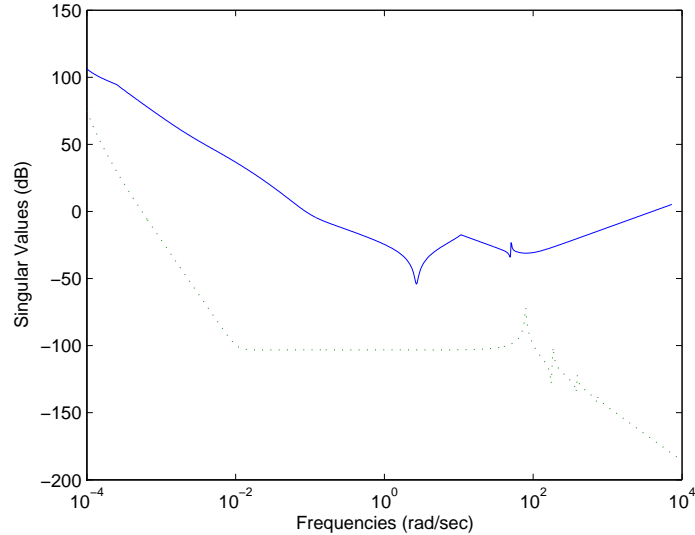


Figure 3.16: Stability Robustness Test Using Reduced Controller

To illustrate this, the design model is comprised of the first nine resonant modes. For the full order system, 333 coefficients are required. For the Bode dynamics approach to pole-zero cancellation, 245 coefficients are required. The system dynamic approach only needs 108 coefficients (67.6% reduction in the number of coefficients when compared to the full order system).

The SR plot using the reduced controller is shown in Figure 3.16 and generates the same stability robustness as that shown in Figure 3.6 for the full order controller. Figure 3.17 and Figure 3.18 compare the full order controller performance (dashed line) to the reduced order controllers (marked with x's). From the singular value plots, the control effort, and dynamic response, it is apparent that the reduced order controller has the same dynamic response as the full order LQG/LTR controller.

Transient system performance is often described in terms of the unit step function response. Since the input into the system is optimally shaped, the system performance specifications are similar with the following definitions. Dynamic delay time is the time required for the system to reach 50% the initial displacement value. Dynamic rise time

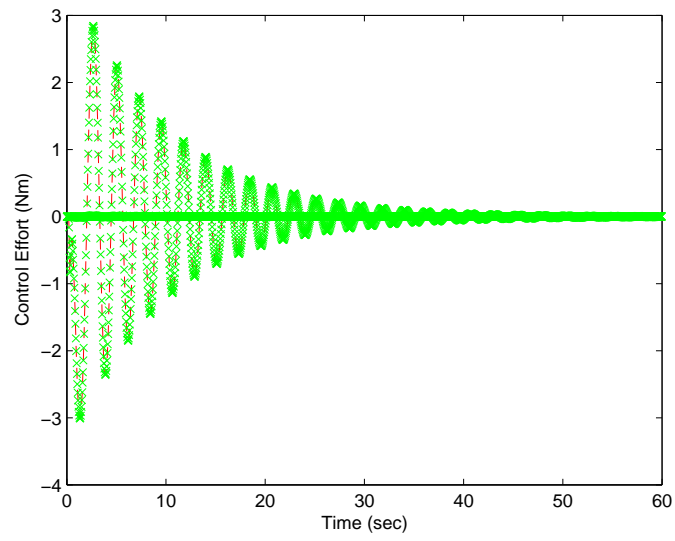


Figure 3.17: Control Effort of Full and Reduced Order Controller

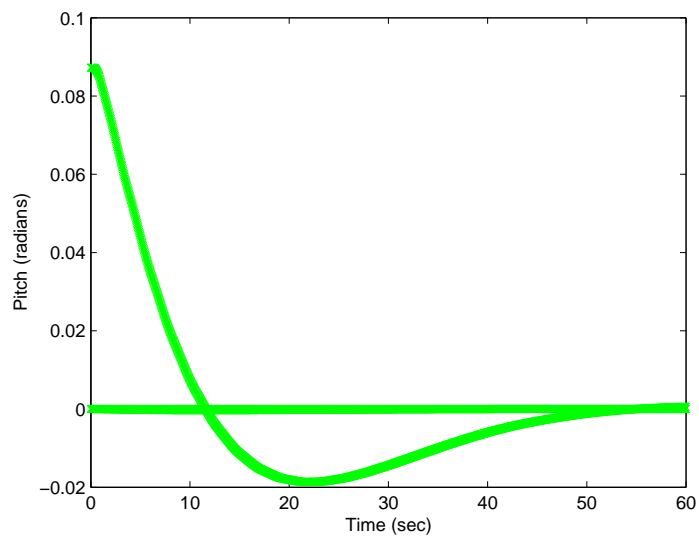


Figure 3.18: Dynamic Response of Full and Reduced Order Controller

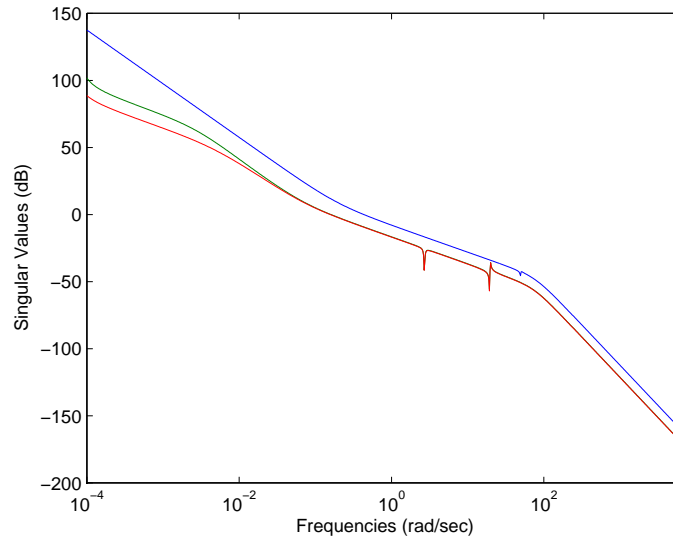


Figure 3.19: Singular Values of Recovered Loop Transfer Matrix, $G_c G_p$

is the time required for the response to go from 90% to 10% of its initial value. The time which the system response settles within 2% of its initial value is the dynamic settling time. Dynamic peak overshoot is the maximum difference between the transient and steady state solution and is represented as a percentage of the initial displacement.

Another performance specification which is measured is the crossover frequency, ω_0 , of the loop transfer matrix. While the stability margin is an indicator of the system performance, the crossover frequency determines the speed of the system response. A higher value for ω_0 means faster response. The crossover frequency is determined by the frequency at which the minimum singular value of the loop transfer matrix, $G_c G_p$, has a gain of 0 dB (see Figure 3.19).

System performance specifications for the baseline model are listed in Table 3.4. The following chapter illustrates how these performance specifications are affected when the elastic properties of the appendage and its length are modified.

Table 3.4: Baseline System Performance

Dynamic Performance	Value
Delay Time	4.1 sec
Rise Time	8.2 sec
Settling Time	48.8 sec
Peak Overshoot	21.3%
Stability Robustness	41 dB
Crossover Frequency	0.025 Hz

Chapter 4

Variation of Appendage Parameters

4.1 Satellite Design Concerns

A survey was presented to lead satellite design engineers involved with the programs at the Space Systems Research Center (SSRC) located at the US Air Force Academy. The involvement characterization of those engineers who responded to the survey includes eight satellite control engineers working directly for the SSRC and the Department of Astronautics, three engineers who formally worked on SSRC satellite design projects, two engineers working for the Air Force Research Laboratory in the Space Vehicles and Propulsion Directorates, two former SSRC members who are currently working on PhD programs with Surrey, and four first-degree Academy Cadets (undergraduate seniors) taking the small satellite design course.

The survey asked each individual what were their top three small satellite design concerns from the following list:

Control Complexity: Number of resonant modes included in the nominal model and design model, reduced order of the controllers, etc.

Material Uncertainties: Variations in elastic modulus, thickness, laminate structure, on-orbit fatigue cycles, etc.

$\frac{\omega_1}{\omega_0}$: The ratio of the first bending mode frequency to the crossover frequency varied via length variation of the appendage.

Control Design Parameters: Weight on states and control effort, loop transfer recovery gain, diagonal matrices, frequency shaped, tuning parameters in Kalman filter, etc.

Spacecraft Parameters: Inertia and mass of spacecraft and tip mass, appendage properties, structural damping ratio, appendage configuration, etc.

Sensors and Actuators: Differing types and locations

The three areas of concern for satellite designers surveyed were control complexity in the implementation sense, system response and sensitivity in the face of material uncertainties, and how the system performs as the ratio $\frac{\omega_1}{\omega_0}$ varies as a result of increasing the length of the appendage. Small flexible spacecraft performance characteristics used to analyze these three concerns were settling time, delay time, rise time, peak overshoot, number of processor operations for each controller, crossover frequency and stability robustness. A discussion on each of the three primary satellite design concerns are presented in the following sections.

4.2 Control Complexity

The complexity of the controller does not refer to whether a simple classical PID controller or compensator is used instead of a more involved optimal controller. The calculation of the controller is done on the ground where computer processing efforts are of little concern. The controllers are determined and the coefficients of the controller transfer functions are loaded onto the spacecraft's on-board processor. A satellite designer's concern is if the on-board processor will be able to run the code or not. A designer would like to see as few lines of code and to minimize the number of operations per computing cycle as possible as long as the system performs within mission requirements. This allows valuable processor time to be dedicated to other system tasks such as telemetry and data handling, payload management, and health and

status updates. This section considers what capabilities a satellite designer gains from using a higher order controller while paying increased computing efforts to implement such controllers.

The primary concern is to measure increased processor costs. Will a satellite designer be able to use a current processor to successfully meet mission requirements or will a more capable processor be required? The answer to this question lies in determining the number of floating point operations a processor can dedicate to the attitude control system. This value is dependant on processor memory size and speed, other system functions the processor needs to support and the sequencing of those functions, and the number of operations per computing cycle required to implement the controller. The latter processor dependency is addressed here while the first two reside in the realm of system integration and concept of operations.

The FLOPS command in Matlab was used by satellite designers to count the number of floating point operations certain programs and functions used during their execution. However, since the release of Matlab version 6.0, this command became obsolete and is no longer practical. In addition, satellite processors typically run C+ code and not Matlab. Time limitations of the research efforts also makes it unfeasible to benchmark simulations of the controller on various commercial-off-the-shelf (COTS) satellite processors and operating systems.

The PROFILE command in Matlab is useful in determining the execution time of a program or function. It is mainly used to debug and optimize run times of M-files by providing information such as execution time, number of calls, parent functions, child functions, code line hit count, and code line execution time. While useful when running Matlab commands, the PROFILE command does not track Simulink simulation runs.

The TIC and TOC commands can be used while executing a Simulink model from the Matlab command window. Tic/toc are stopwatch commands which provide elapsed time measurements from when tic starts the watch and when toc stops it. The command

entered in the Matlab command window is `tic,[t,x,y]=sim('modelname',runtime);toc`. This command starts the stopwatch, executes the Simulink model 'modelname' and runs from 0 to runtime (in seconds), then stops the stopwatch and prints the elapsed time.

Test runs of the Simulink model were for 60 second simulations. Since integrators like `ode45` have variable time steps, it is necessary to change the time step size in the simulation configuration parameters solver options from variable-step sizes to fixed time steps so that each run was conducted over fixed time intervals. The Runge-Kutta solver `ode4` was used with fixed time step size of 1 ms. In addition, various programs open on the desktop may use CPU resources while the simulations were being run. Therefore, prior to data collection, the computer needs to be restarted with only Matlab open. This will prevent occasional pings to the system from the network or resource allocations used from Outlook during received emails.

Even after restarting the computer, slight variations in run time may be experienced during several runs of the same simulation. Larger variations were noticed when the CPU usage history demonstrated increased numbers of non-linear affects instead of smooth histories. An interesting observation is larger occurrences of non-linear CPU usage was noted when simulations involved larger numbers of controller coefficients (see Figure 4.1 and Figure 4.2). This is meaningful in that if the on-board processor must cache data, a non-linear usage of the processor will be noted.

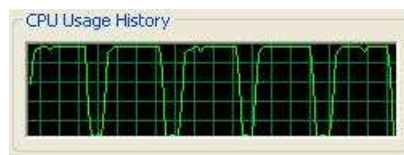


Figure 4.1: Smooth CPU Usage History

To determine a more accurate estimate of run times, 10 runs were done for each

simulation with the average time being recorded. In addition, each run wasn't started until the hard drive was no longer being accessed and the CPU Usage History was 0% for 5 seconds.

Elapsed execution times were recorded for differing design models based on included flexible modes, m . From previous work presented in Chapter 3, the truth model includes the first 10 flexible modes, $m=10$, along with the six low frequency resonant modes while the baseline design model included the first flexible modes about each axis, $m=3$. Not only were simulations run for the full order controllers for each design model, but times were also calculated for reduced order controllers.

The number of operations performed per computing cycle is equivalent to the number of addition, subtraction, multiplication, and division operations conducted. If a transfer function of the controller is of the general form

$$\frac{a_0 s^m + a_1 s^{m-1} + \dots + a_{m-1} s^1 + a_m}{b_0 s^n + b_1 s^{n-1} + \dots + b_{n-1} s^1 + b_n} \quad (4.1)$$

where a and b are coefficients needing to be programmed, n is the order of the controller, and m is the order of zeros. Recall there are nine controller transfer functions for a 3-input 3-output system. Considering only the addition and multiplication of the coefficients, the total number of operations performed is equal to

$$operations = \sum_i^9 2(n_i) + \sum_i^9 2(m_i) + 18 \quad (4.2)$$

Since $m = n - 1$, and adding to the result nine for the division within the transfer functions, six for the computation of each of the three input signal as a result of three



Figure 4.2: Non-Linear CPU Usage History

measurement contributions for each, and adding an additional three for feeding back the three inputs, Eq.4.2 becomes

$$\begin{aligned} \text{operations} &= \sum_i^9 2(n_i) + \sum_i^9 2(n_i - 1) + 18 + 9 + 6 + 3 \\ &= \sum_i^9 4(n_i) + 18 \end{aligned} \quad (4.3)$$

As was shown in Chapter 3, the number of coefficients needing to be programmed into the on-board processor is

$$\text{coefficients} = \sum_i^9 2(n_i) + 9 \quad (4.4)$$

and the number of operations performed per computing cycle is twice the number of coefficients of the controller transfer function matrix.

The elapsed run time for each case is plotted vs the number of operations for each design model and is shown in Figure 4.3. The legend identifies which plot line corresponds to which design model where m is the value representing the number of flexible modes included in the design model. The plot is linear except in the region where the number of operations exceeds 600. This is a result of the non-linear usage of the CPU capability and caching of virtual memory to the hard drive.

The data collected for the run times was collected on a Pentium(R) 4 CPU, 1.69 GHz, with 256 MB of RAM and using the Microsoft Windows XP version 2002 operation system. However, satellite processors are not using the same processor and will run code in forms other than M-files. To account for this, the data is non-dimensionalized by dividing through all of the run times by the time it took to execute the baseline design model with the smallest order controller (pole-zero cancellations determined with tolerance equal to 0.1 during the minimum realization calculations). This allows a comparison of implementation difficulty of one design model/reduced controller over another (see Figure 4.4). This information is useful for satellite designers to determine on-board processor size and capabilities while considering more complex control structures by

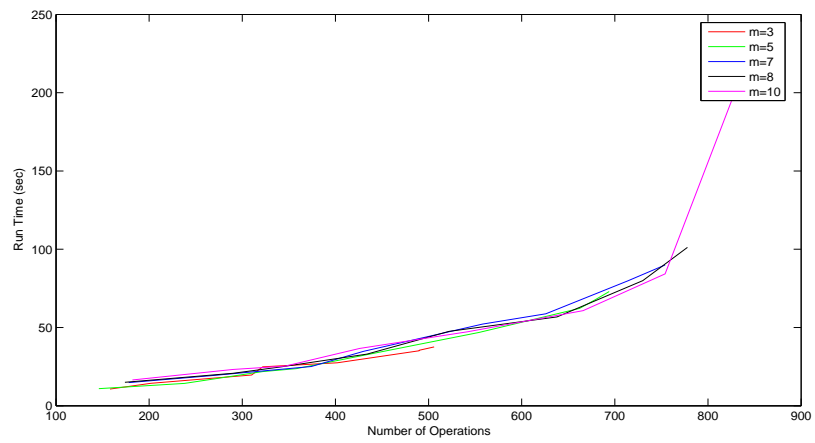


Figure 4.3: Elapsed Time vs Number of Operations

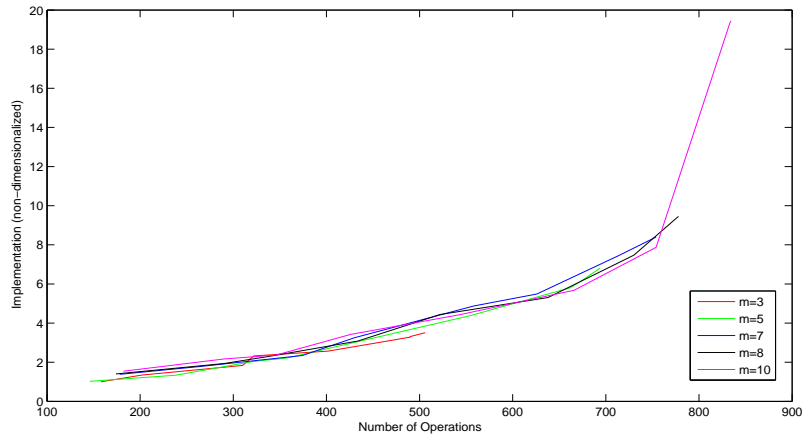


Figure 4.4: Implementation Costs of Various Order Design Models

allowing them to quickly look up how many operations are required to implement the various orders of controllers.

Figure 4.5 takes a look at how the number of operations per computing cycle decreases as the tolerance step changes. Using this plot, satellite designers can consider how many operations their on board processor can dedicate to the attitude control architecture and determine which design model to implement and how far they need to reduce the controller order before needing to acquire a higher performing processor. For example, if a satellite designer determines that a given processor is capable of dedicating 500 operations per cycle to the control system, then a design model which includes the first three flexible modes may be run regardless of the reduced order of the controller. However, to implement any of the other design models which include more flexible modes, the controllers need to be reduced in order while using tolerance equal to 0.0001 during the minimum realization process. Now, the satellite designer must determine whether they need to go to a better performing processor or not.

The main considerations for a satellite designer, when determining processor size, is will the added cost and power consumption generate increased stability robustness and performance. As shown in Chapter 3, the baseline model ($m=3$) had a stability

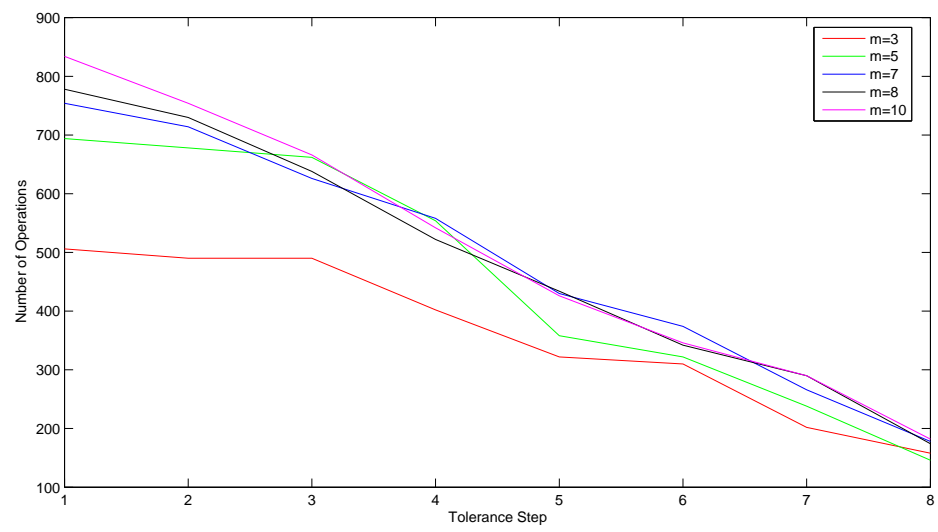


Figure 4.5: Pole-Zero Cancellation Effects on Number of Operations

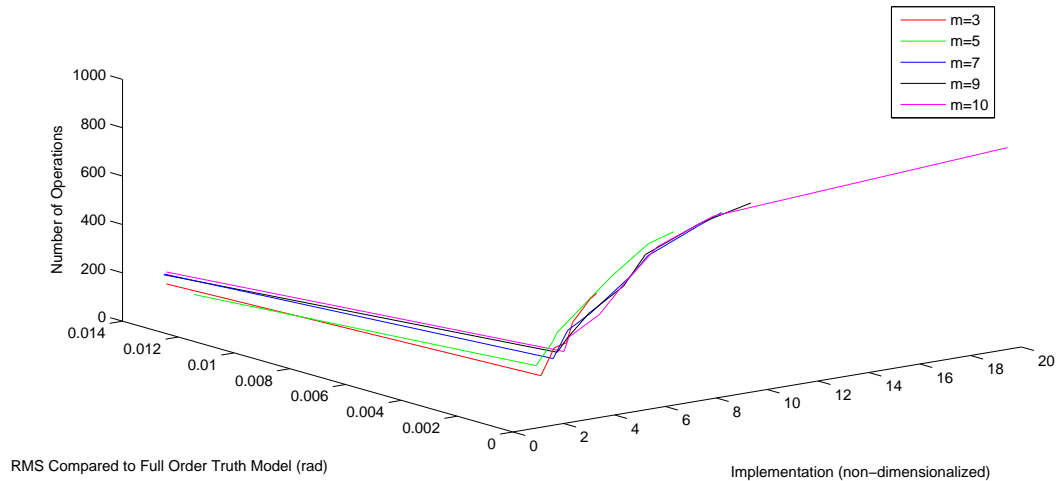


Figure 4.6: Dynamic Performance and Implementation Difficulty

robustness of 41 dB. Adding more flexible modes in the design model increases this stability robustness. However, since the reaction wheels have a limit placed on them with how much torque they can generate, the increased stability robustness gains the satellite designer nothing since the bode gain cannot be increased to improve performance (the control effort limit of 3Nm and how the weighting matrices in the LQG/LTR design impact this effort and system performance is shown in Chapter 3).

Since a satellite designer doesn't benefit from an increase in stability robustness, the consideration of dynamic performance becomes important. Now, the full order controller generated for the truth model is the benchmark when determining system performance. RMS values are calculated for each design model and each reduced controller to compare their dynamic response to that of the full order truth model. A 3-dimensional plot is created to show the relationship between these RMS values, implementation difficulty, and number of operations (see Figure 4.6).

A satellite designer can use Figure 4.6 to determine which control complexity to use on the satellite. A favorable location occurs in the lower/middle portion of the graph where RMS values of the reduced system response compared to the full order

Table 4.1: Performance Comparison Between Baseline and Truth Model

Performance	Baseline Model	Truth Model
Delay Time (sec)	4.1	4.1
Rise Time (sec)	8.2	8.3
Settling Time (sec)	48.8	48.8
Peak Overshoot (%)	21.3	21.0
Crossover Frequency (Hz)	0.025	0.025
Stability Robustness (dB)	41	125

truth model response are the smallest with requiring fewer operations per cycle and easier implementation. From this plot, and knowing that the baseline model ($m=3$) meets stability robustness requirements, the baseline model presented in Chapter 3 is an ideal choice for a satellite designer. The system performance of the baseline model is nearly identical to the performance of the full order truth model except for stability robustness (see Table 4.1). The same performance is achieved with the baseline model while using 37.2% the number of operations, being 20 times easier to implement, and only has an dynamic RMS error of 0.01° . Therefore, the baseline model is the better choice unless mission requirements desire pointing accuracies of 0.01° or better.

4.3 Material Uncertainty

System performance was nearly identical between the baseline model using reduced order controllers and the truth model using full order controllers. Satellite designers can use this information in the sizing of on-board processors. However, another concern the survey indicated was would mission requirements be greatly impaired if material uncertainties in the flexible structure were taken into consideration.

Not every elastic memory composite component is manufactured with identical properties. A certain level of uncertainty, or error bar, exists between one piece and

another. CTD mentions this is a result of variances in material thickness, laminate properties, mesh formulation, variances in parasitic components such as heating coils, resin, connections, etc. The composite industry typically does not measure every possible variance in the material. Instead, they lump the material uncertainties into the elastic modulus and accept an uncertainty of $\pm 10\%$ of the baseline elastic modulus (3-sigma).

One consideration which is not included in the error bar is on-orbit fatigue cycling of the composite material. Currently, no data exists (theoretical or experimental) to determine a level of uncertainty in the elastic modulus resulting from prolonged exposure to the space environment. On-orbit fatigue of the material may result in an increase of stiffness (non-linear stress to strain relationships, resin hardening, etc) or an increase in flexibility (severed laminate fibers, variance in thermal transition barriers, etc) in the material.

To account for the unmodeled fatigue cycles, numerical analysis of the baseline model was run while varying the baseline elastic modulus, E_o , from 80% to 120% at 1% intervals. This allowed the modified elastic modulus, E_i , to take on values of $0.80E_o$, $0.81E_o$, \dots , $1.19E_o$, and $1.20E_o$. While the ratio, $\frac{E_i}{E_o}$, was varied, the following parameters were held constant: mass, inertia, structural shape, area, poisson ratio, shear modulus, density, weighting matrices Q and R, recovery gain r, and the tolerance used in the minimum realization of the controllers.

An analytical relationship of how the resonant frequencies change as a function of elastic modulus is shown in the following derivation:

$$\omega = c\sqrt{\frac{EA}{mL}} \quad (4.5)$$

where ω is the baseline resonant frequency, c is a characteristic value dependent on boundary conditions and resonant number, E is the elastic modulus, A is the cross-sectional area, m is the appendage mass, and L is its length.

When the elastic modulus is varied by a value of δE , the modified resonant

frequency, ω^* , is found by

$$\omega^* = c\sqrt{\frac{(E + \delta E)A}{mL}} \quad (4.6)$$

and this frequency is determined by

$$\begin{aligned} \left(\frac{\omega^*}{\omega}\right)^2 &= \frac{\frac{c^2(E+\delta E)A}{mL}}{\frac{c^2EA}{mL}} \\ &= \frac{E + \delta E}{E} \\ \omega^* &= \omega\sqrt{1 + \frac{\delta E}{E}} \end{aligned} \quad (4.7)$$

Analytical relationships between elastic modulus variation and system performance characteristics do not exist. However, it is possible to estimate these relationships by taking data from the numerical analysis on the baseline model as perviously mentioned. Each elastic modulus ratio is entered into Patran and generates a new eigen analysis. This information is placed into an input file for the Matlab code and dynamic response simulations are executed. Values for peak control effort, stability robustness, crossover frequency, delay time, rise time, settling time, and percent overshoot were recorded. The data was plotted versus the elastic modulus ratios to determine a relationship between material uncertainties and system performance.

The Basic Fitting Option was used to evaluate the plots and generate a "best fit" polynomial, in the least squares sense, for a given set of data. Residuals were calculated as a measure of how well the predicted data matches the observed data. If the residuals show strongly patterned behavior, then it should be possible to do better than a simple polynomial fit (exponential fit). Error bounds are also calculated for each data set to determine if the data is reasonably modeled by the fit. The error bound uses an interval of $\pm 2\delta$ which corresponds to a 95% confidence interval. The Matlab commands POLYFIT and POLYVAL were used to perform curve fitting.

As the flexible structure increases in stiffness, the crossover frequency of the loop transfer matrix remained constant, peak control effort, stability robustness, and peak

Table 4.2: Performance Characteristics as a Function of Material Uncertainty

Performance Characteristic	Material Uncertainty Ratio (x)
Peak Control Effort (Nm)	$= 1.3551 + 1.6588x$
Stability Robustness (dB)	$= 31.136 + 8.1023x$
Crossover Frequency (Hz)	$= 0.025$
Delay Time (sec)	$= 4.5491 - 0.46261x$
Rise Time (sec)	$= 9.2476 - 0.9941x$
Settling Time (sec)	$= 49.729 - 1.0029x$
Peak Overshoot (%)	$= 17.053 + 4.4043x$

overshoot increases, and delay, rise, and settling times decrease. The linear equations for these relationships are listed in Table 4.2 while the resulting plots are shown in Figures 4.7 through 4.20.

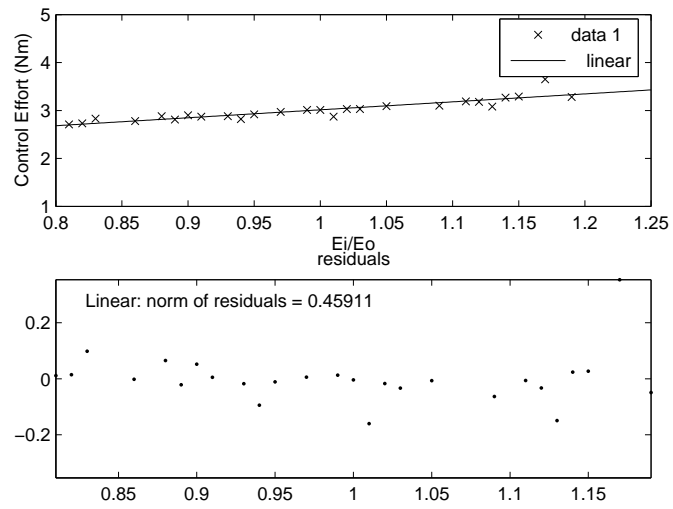


Figure 4.7: Linear Fitting of Peak Control Effort Data

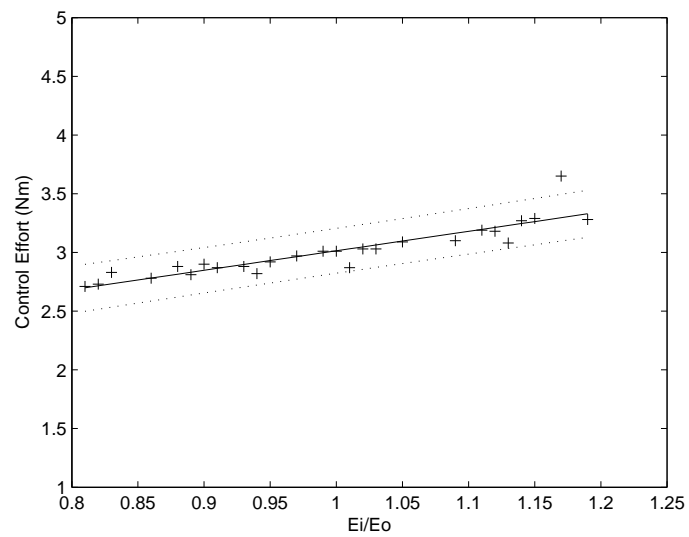


Figure 4.8: Error Bounds for Peak Control Effort Data

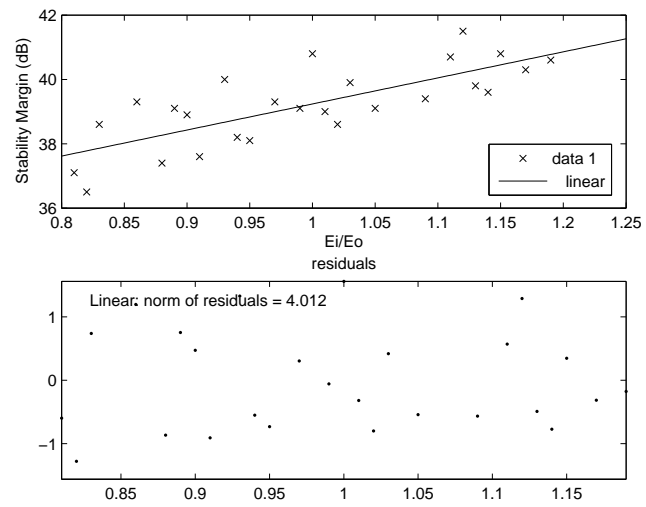


Figure 4.9: Linear Fitting of Stability Robustness Data

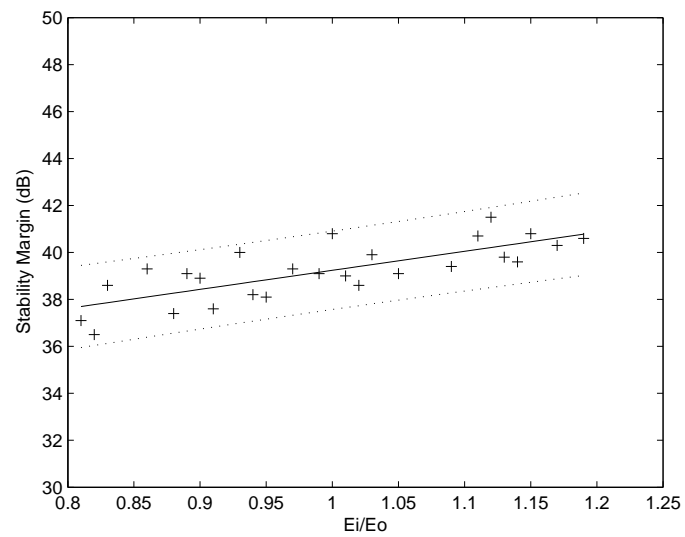


Figure 4.10: Error Bounds for Stability Robustness Data

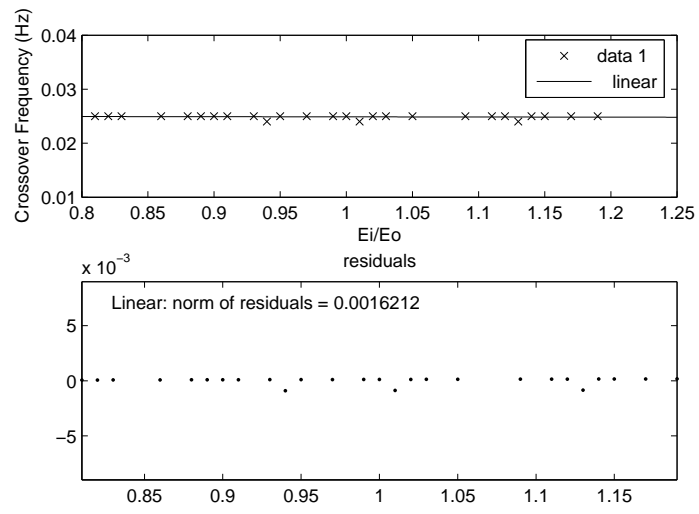


Figure 4.11: Linear Fitting of Crossover Frequency Data

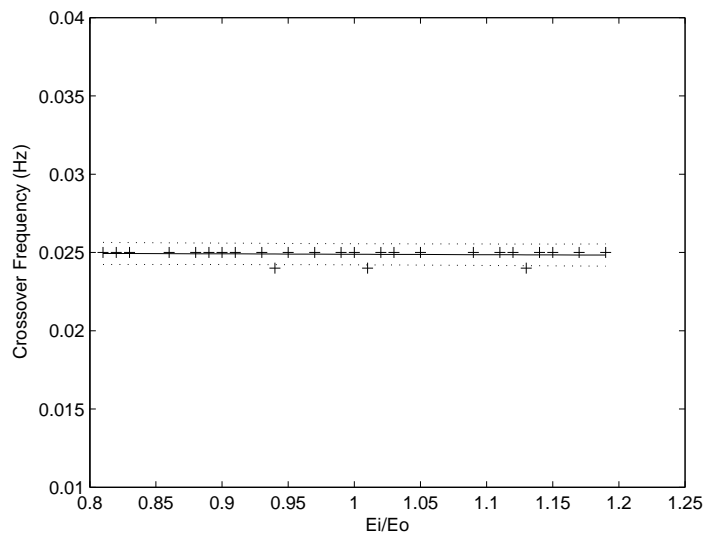


Figure 4.12: Error Bounds for Crossover Frequency Data

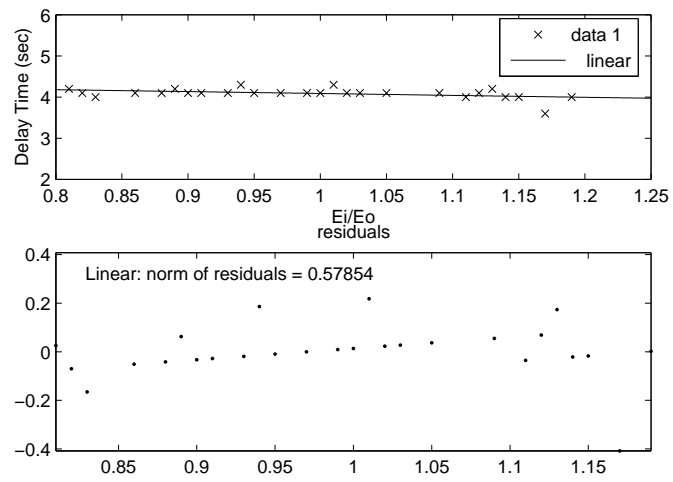


Figure 4.13: Linear Fitting of Delay Time Data

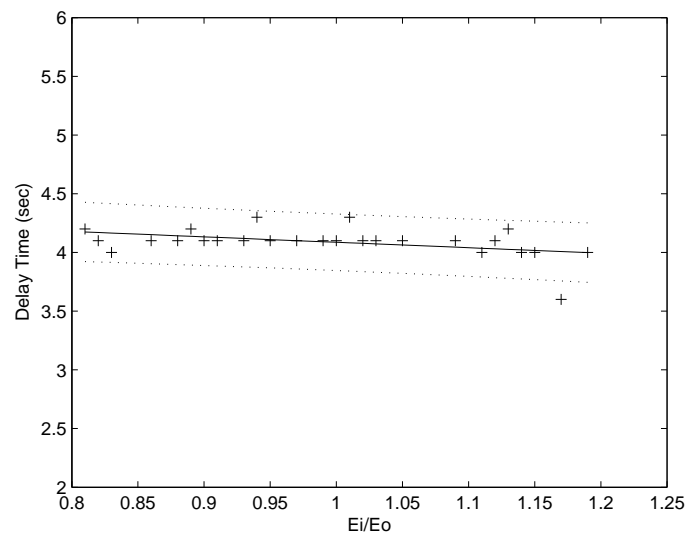


Figure 4.14: Error Bounds for Delay Time Data

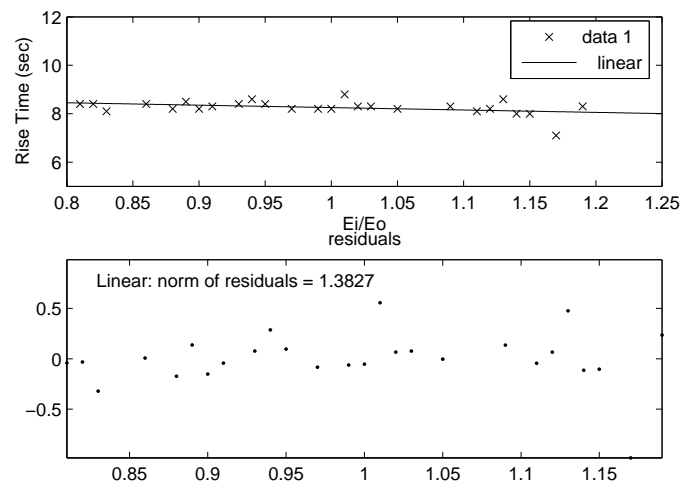


Figure 4.15: Linear Fitting of Rise Time Data

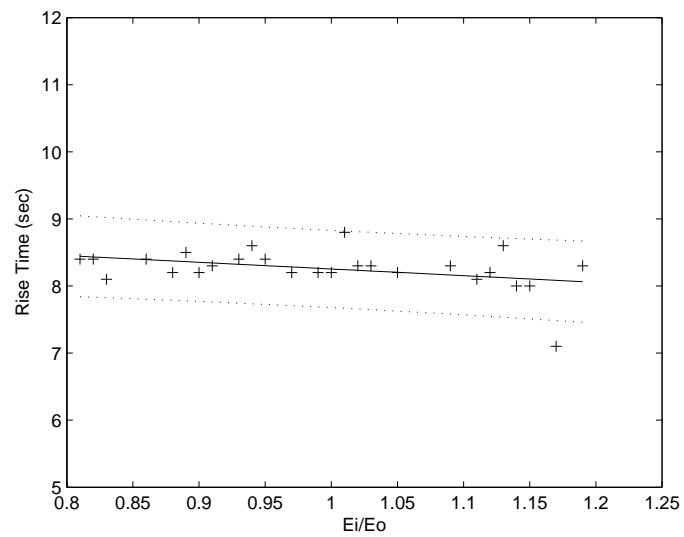


Figure 4.16: Error Bounds for Rise Time Data

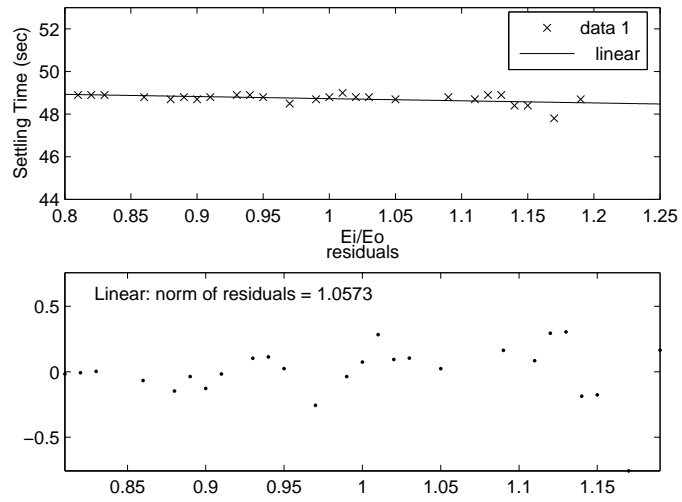


Figure 4.17: Linear Fitting of Settling Time Data

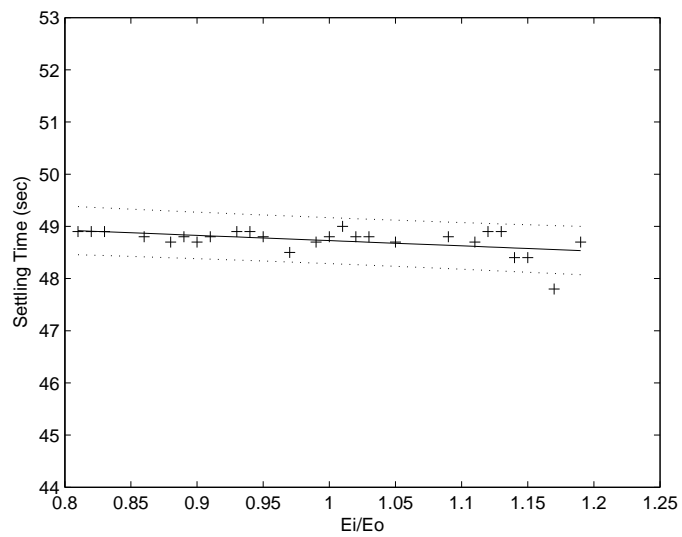


Figure 4.18: Error Bounds for Settling Time Data

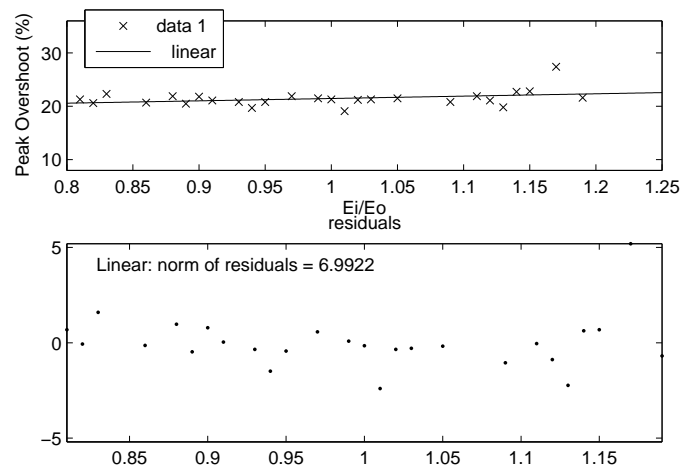


Figure 4.19: Linear Fitting of Peak Overshoot Data

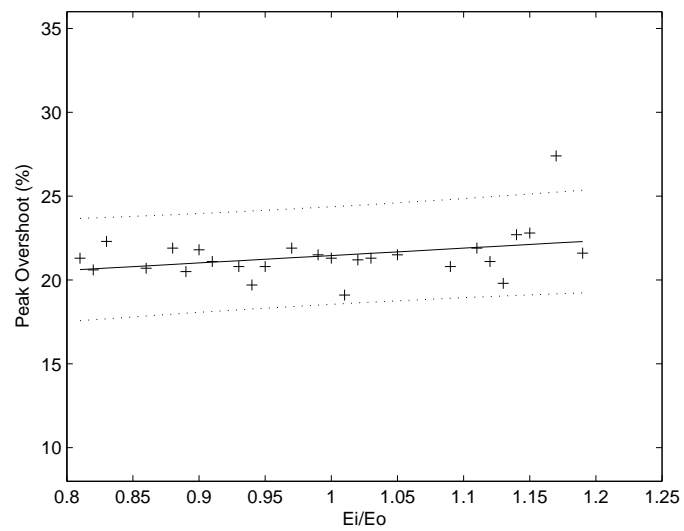


Figure 4.20: Error Bounds for Peak Overshoot Data

An interesting observation is drawn from the residual plots in that each data entry resulting from the Simulink run of ratio 1.17 resulted in an observed value which falls outside the error bound. It is expected for some values to fall outside the error bounds since the confidence interval is 95%. However, for all simulation response points for this one case may indicate a faulty assumption.

A likely assumption which contributes to this observation is holding the tolerance value constant during the minimum realization of the controllers. The comparison plot of the reduced and full order controller bode dynamics in Section 3.4 shows a divergence at low frequencies (see Figure 3.13). This difference is in the low frequency region of the system where the system poles and zeros are in close proximity. When Patran generates the modal information, it is unable to provide zero frequency information. Numerical artifacts in the analysis produce frequencies of 10^{-11} Hz. It is possible these numerical artifacts may become important in the system dynamic response.

RMS values were calculated of both control effort and dynamic response for the case where the elastic modulus ratio equaled 1.17 (see Figure 4.21 and Figure 4.22). A large gradient is apparent in the tolerance step region where the baseline model plots indicated a tolerance value of 0.001, tolerance step of 6, during minimum realization of the controllers while the following plots indicate the tolerance value should equal 10^{-6} , tolerance step of 3.

For more accurate predictions, the use of a full order controller is required so that low frequency dynamics are not lost. However, it turns out the system is not sensitive to the differing controller order. The system performance characteristics, for the case where $\frac{E_i}{E_o} = 1.17$, shown in Table 4.3 for a full order controller and those of a controller realized when tolerance equals 0.001 indicate minimal impact of increased pole zero cancelations near the origin. Five of the seven values were identical while the difference in settling time was 0.6% and peak overshoot was 0.4%.

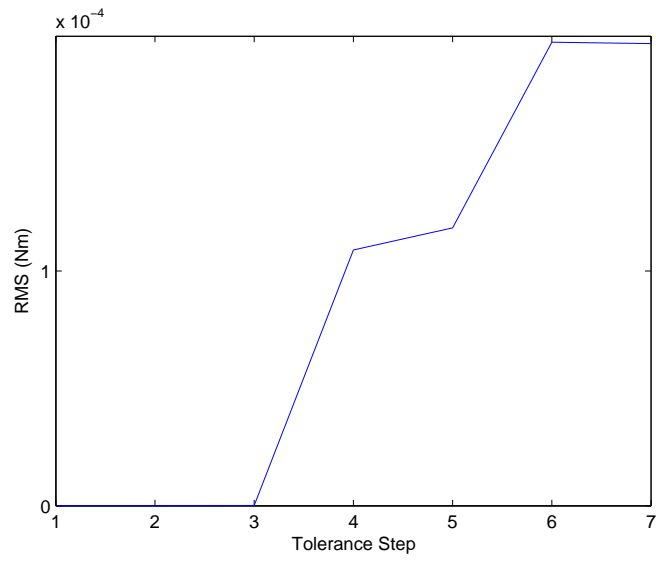


Figure 4.21: Full/Reduced Order Control Effort for Material Uncertainty Ratio 1.17

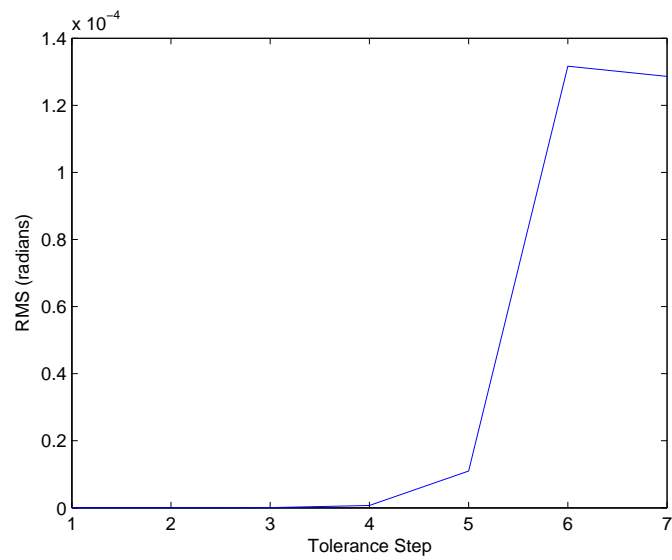


Figure 4.22: Full/Reduced Order Dynamic Response for Material Uncertainty Ratio 1.17

Table 4.3: Performance Comparison Between Full and Reduced Controller

Performance	Full Order Controller	Reduced Order Controller
Delay Time (sec)	3.6	3.6
Rise Time (sec)	7.1	7.1
Settling Time (sec)	47.8	48.1
Peak Overshoot (%)	27.4	27.3
Peak Control Effort (Nm)	3.65	3.65
Crossover Frequency (Hz)	0.025	0.025
Stability Robustness (dB)	40.3	40.3

4.4 Appendage Length

As the length of a gravity gradient boom is increased, the mass located at its deployed end can be reduced while maintaining the required moment of inertia in the nadir/zenith axis. This is a concern for small satellite designers because of the mass and volume limitations these satellites possess. While uncertainties in the appendage material produced linear approximations for system performance, this may not remain the case as its length is increased. The appendage may reach a certain length at which the design model will need to be modified to include higher frequency mode shapes.

To vary the appendage length for data collection purposes, a small step size (on the order of 1% of the original length) is used and system performance parameters are calculated. The length is increased by the same step size and the parameters are calculated again. If the data appears linear, then the step size is doubled. Increasing the step size in this matter is repeated until the data no longer appears linear. Then, the initial step increment is applied to the appendage length prior to the last step size increase and the process is continued. The gradient decent method provides a systematic approach to increasing the appendage length while spending less time in regions of minimal change and focusing most of the data collection efforts where the

data varies at a greater rate.

A primary concern for this section is how does the flexible system perform as the resonant frequencies approach the crossover frequency of the loop transfer matrix. A relationship between the original resonant frequency, ω_1 , and the frequency once the length is modified, ω_2 , is shown in the following equations:

$$\begin{aligned}
 \omega_1 &= c\sqrt{\frac{EA}{mL}} \\
 \omega_2 &= c\sqrt{\frac{EA}{m(L+\delta L)}} \\
 \frac{\omega_2}{\omega_1} &= \left(\sqrt{\frac{1}{L+\delta L}}\right)/\left(\sqrt{\frac{1}{L}}\right) \\
 \frac{\omega_2}{\omega_1} &= \sqrt{\frac{L}{L+\delta L}}
 \end{aligned} \tag{4.8}$$

where the frequency equation was shown in Eq. 4.5.

The baseline system has the first bending mode at a frequency of 3.1518 Hz (see Table 2.7) and a crossover frequency at 0.025 Hz (see Table 3.4). This yields a baseline ratio of $\frac{\omega_1}{\omega_0} = 126.07$. Inserting this value into Eq. 4.8 creates a method of relating an increase in length to a desired frequency ratio.

$$\begin{aligned}
 \omega_2 &= 126.07\omega_0\sqrt{\frac{L}{L+\delta L}} \\
 \frac{\omega_2}{\omega_0} &= 126.07\sqrt{\frac{L}{L+\delta L}} \\
 \sqrt{1+\frac{\delta L}{L}} &= \frac{\text{currentratio}}{\text{desiredratio}} \\
 1+\frac{\delta L}{L} &= \left(\frac{\text{currentratio}}{\text{desiredratio}}\right)^2 \\
 \delta L &= L\left(\left(\frac{\text{currentratio}}{\text{desiredratio}}\right)^2 - 1\right)
 \end{aligned} \tag{4.9}$$

An initial run of the simulations considered increasing the length of the appendage while holding all other variables constant across the simulations. Data collected is shown

Table 4.4: Simulation Results When Only Appendage Length is Varied

Length (m)	Peak CE (Nm)	SR (dB)	ω_1 (Hz)	ω_0 (Hz)	Frequency Ratio
4.0	3.06	40.7	3.1518	0.0241	130.78
4.111	3.06	39.6	3.0979	0.0250	124.10
4.32	2.92	35.4	3.0009	0.0242	124.15
4.5	2.80	34.8	2.9211	0.0234	124.59
4.8	2.71	32.8	2.7952	0.0228	122.84
5.1	2.63	29.6	2.6764	0.0215	124.74
5.7	2.45	26.0	2.4557	0.0211	116.40
6.9	2.12	15.3	2.0638	0.0181	113.90
7.8	2.03	11.8	1.8046	0.0176	102.30
8.0	1.87	10.7	1.7509	0.0164	106.47
8.2	1.77	10.9	1.6986	0.0164	103.25

in Table 4.4. The heading for the table lists appendage length, peak control effort, stability robustness, frequency of the first bending mode, crossover frequency, and the ratio of first bending mode to crossover.

The stability robustness value steadily decreases as the appendage length increases. There occurs a length at which the baseline design model will no longer remain robust in the face of unmodeled/uncertain high frequency structural modes and noise. To estimate at what point this occurs, the stability robustness values were plotted versus length (see Figure 4.23).

If the decreasing values of the norm of the residuals shown in Table 4.5 are used to indicate which order of polynomial to fit the observed data, a fifth order polynomial can be determined to estimate at what length the SR test is violated and should not be used to accurately estimate values beyond the immediate range of the data observed. The fifth order polynomial produced is

$$SR = -0.18411L^5 + 5.8804L^4 - 73.717L^3 + 453.7L^2 - 1379.6L + 1701.3 \quad (4.10)$$

Using Eq. 4.10, one can estimate at what appendage length will the stability

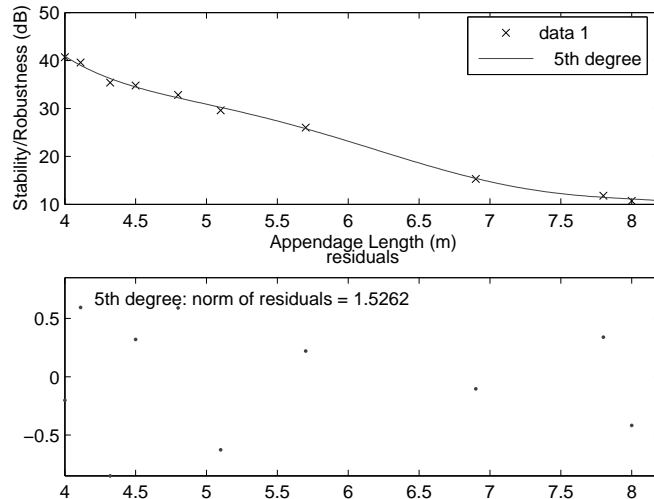


Figure 4.23: Curve Fitting of Stability Robustness Data for Length Variation

robustness value be negative, which indicates the need to include the second bending modes in the design model. This resulted in an appendage length of 9.2 m.

Since the weighting matrices used in the LQG/LTR process, Q and R , were held constant, both peak control effort and crossover frequency decreased. The intent is to maximize the control input of the reaction wheels (3.0 Nm). Therefore, the simulations were repeated while increasing the q/r ratio so that the peak control effort of 3.0 Nm is maintained. The resulting data is presented in Table 4.6. The inclusion of the frequency of the second bending modes, ω_2 , is included to illustrate how its ratio changes.

By allowing the simulation to reach the control limit of the reaction wheels, the $\frac{\omega_1}{\omega_0}$ ratio decreased at a faster rate. Also, the stability robustness value becomes an issue at a shorter appendage length than the estimated 9.2m. When the SR values of 3.9 dB and 3.8 dB (for lengths of 8.0m and 8.2m) are taken in consideration with the information provided in Section 4.3, a different conclusion is made. The linear equation relating stability robustness to material uncertainty, the associated error bounds, and the norm of the residuals indicate the SR value of 3.9 dB for an appendage length of

Table 4.5: Norm of Residuals for Appendage Length Variation

Curve Fitting Order	Norm of Residuals
Linear	4.7192
Quadratic	2.6403
Cubic	2.5253
4th order	1.9473
5th order	1.5262
6th order	1.5258
7th order	1.5134

8.0m may not provide a safe enough margin for the baseline design model.

To further study when inclusion of the second bending modes in the design model is desirable, consider the plot of q/r ratio versus appendage length (see Figure 4.24). The plot is linear until an appendage length of 8.0 m is reached. This is another indication that for appendage lengths equal to or greater than 8.0m, the system will not remain robust in the face of unmodeled/uncertain high frequency dynamics and noise.

Consider what happens to the stability robustness plot for a design model using an appendage length of 8.2m. From the plots shown in Figure 4.25 and Figure 4.26, a satellite designer sees that a better stability robustness value is achieved when the second bending modes are included in the design model. Table 4.7 contains key simulation data for both design models with an appendage length of 8.2m.

When the second bending modes are included in the design model, the SR value changes from 3.8dB to 34.7dB, while the q/r ratio and crossover frequency remain relatively the same. Once the appendage length reaches 8.0m, the satellite designer must consider stability robustness of the system with information provided on material uncertainties and the increased number of operations to execute such a controller using on-board processors.

Table 4.6: Simulation Results When Control Effort Limit is Maintained

Length	q/r	Peak CE	SR	ω_0	ω_1	$\frac{\omega_1}{\omega_n}$	ω_2	$\frac{\omega_2}{\omega_n}$
4.0	0.010	3.06	40.7	0.0241	3.1518	130.78	12.5924	522.50
4.111	0.010	3.06	39.6	0.0250	3.0979	124.10	12.1313	485.25
4.32	0.011	2.99	35.2	0.0247	3.0009	121.49	11.3213	458.35
4.5	0.013	2.99	34.2	0.0251	2.9211	116.59	10.6764	425.36
4.8	0.015	2.99	31.9	0.0252	2.7952	110.93	9.7202	385.72
5.1	0.017	3.00	28.5	0.0244	2.6764	109.62	8.8757	363.76
5.7	0.021	2.99	24.4	0.0255	2.4557	96.43	7.4989	294.07
6.9	0.033	3.00	12.6	0.0241	2.0638	85.77	5.6494	234.42
7.8	0.041	3.00	8.6	0.0251	1.8046	71.98	4.7640	189.80
8.0	0.059	2.99	3.9	0.0249	1.7509	70.42	4.6073	185.03
8.2	0.084	2.99	3.8	0.0271	1.6986	62.79	4.4592	164.55

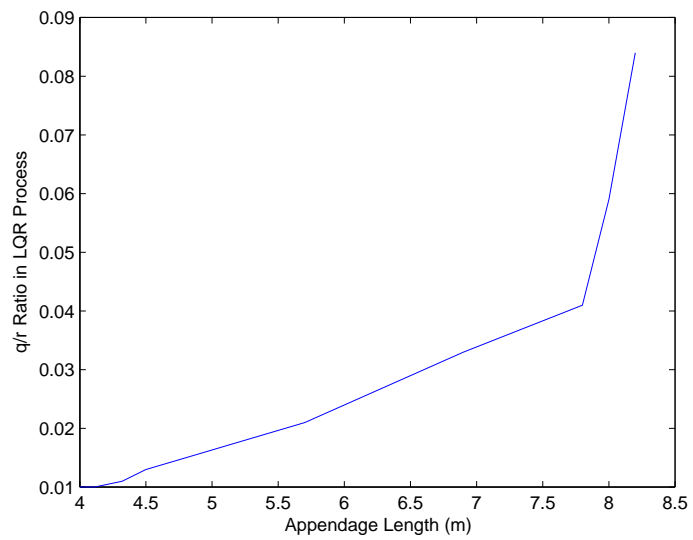


Figure 4.24: LQG/LTR Design Ratio, q/r, as Appendage Length is Varied

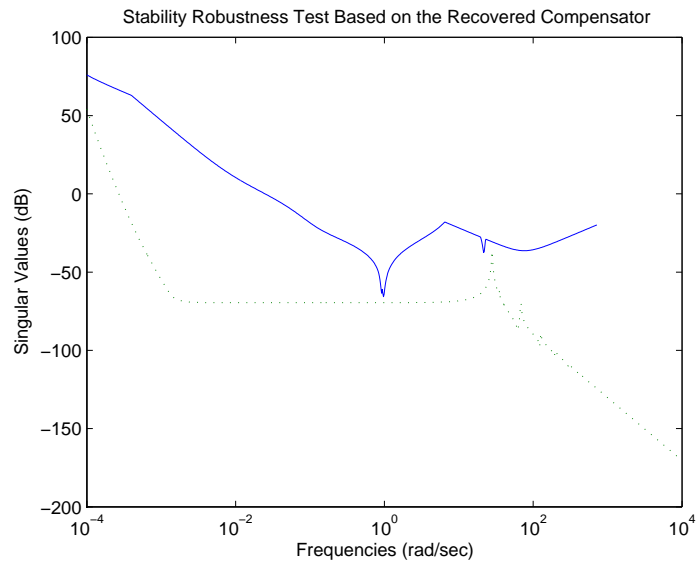


Figure 4.25: SR Plot for 8.2m Appendage with 1st Bending Modes in Design Model

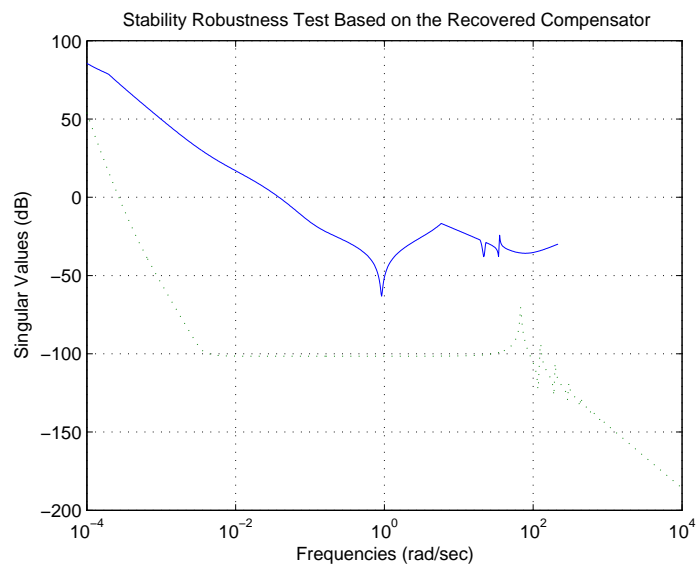


Figure 4.26: SR Plot for 8.2m Appendage with 2nd Bending Modes in Design Model

Table 4.7: Comparison of Design Models for the 8.2m Appendage

	1st Bending Modes	2nd Bending Modes
q/r Ratio	0.084	0.073
Peak CE	2.99	2.99
SR	3.8	34.7
ω_0	0.0271	0.0260
$\frac{\omega_1}{\omega_0}$	62.79	65.26
$\frac{\omega_2}{\omega_0}$	164.55	171.32

Chapter 5

Research Summary and Recommendations

5.1 Research Summary

The trend in utilizing small satellites to accomplish space missions has been steadily increasing over the last two decades. Businesses, governmental organizations, and academic institutions find the reduced development costs and time lines, when compared to the larger conventional satellites, an appealing benefit when establishing a small satellite program.

As the number of small satellite missions increase in the coming years, so too will the unique ways in which designers prepare for these missions. Working within mass, volume, and power constraints, satellite designers will "push the envelope" on what is possible to accomplish. These efforts will generate creative ways of designing satellites to successfully meet mission requirements. Non-traditional methods of deploying structures on small satellites is one such emerging area of study.

Current research efforts conducted within the materials industry are looking into constructing deployable structures from elastic memory composites (EMC). Strain energy is stored within appendages made from shape memory composites and can be released upon command by heating the material beyond its glass transition temperature. Shape memory mechanisms can eliminate the need for traditional highly complex mechanical deployment devices, massive launch canisters, and independent deployment control systems.

While EMC appendages require less mass and volume compared to similar performing traditional booms made from beryllium copper, the increased flexible nature is a concern for the satellite's attitude control system. Historically, research in the area of flexible spacecraft control has focused on assuming cantilevered boundary conditions at the connection point between the spacecraft bus and the flexible appendage. This assumption simplifies several terms in the Lagrangian dynamics because the center of mass of the system experiences small variations. However, the cantilever assumption becomes less valid as the mass of the satellite bus is reduced and the appendage configuration does not take on an asymmetric shape.

As the system's center of mass moves further away from the center of mass of the controlling body, larger displacements of the system's center of mass are realized in the body reference frame for the deformed spacecraft. This means the time rate of change of the system's inertia matrix is not zero and terms once neglected in the Lagrangian now need to be taken into consideration. Assuming a free-free boundary condition for determining the mode shapes of the small flexible spacecraft is the correct approach in creating a more accurate dynamic model of the system.

LQG/LTR optimal control techniques were applied to a dynamic model generated from generalized mass and stiffness matrices created from a finite element model of a small satellite using a gravity gradient boom comprised of EMC materials. The satellite mirrors the FalconSat-3 spacecraft designed at the US Air Force Academy's Space Systems Research Center. The design considerations for the LQG/LTR controller is to return the spacecraft to nominal pointing requirements following an initial displacement that could result from momentum dumping of the on-board reaction wheels.

This research provides insight in the area of small flexible spacecraft which a satellite designer can use to determine computer processor sizing, how material uncertainties and fatigue cycling may impact system performance parameters, and what happens to the robustness of the control system as the length of the appendage is varied.

5.2 Future Research Recommendations

Several key areas of future research are mentioned in this section. A significant finding from this research study is if one were to create the nominal and design models using the method outlined in Section 2.3, and then calculate the additive uncertainty matrix using

$$\Delta G = G_{nom} - G_{des} \quad (5.1)$$

then it becomes necessary to include the first bending and torsional modes in the design model even though these modes are two orders greater than the magnitude of the crossover frequency. According to the literature, control system designers model a system as a rigid body as long as the first resonant mode is at least one order of magnitude greater than the crossover frequency. Yet, for this research, the low frequency design model should not be confused with a rigid body model since the FEM analysis generates low frequency information instead of zero mode information.

The rule of thumb of one order of magnitude is using the same assumption of boundary conditions as has been used repeatedly for the last 40 years of research. This assumption is that the system is modeled as a cantilever appendage where the system center of mass is contained within the controlling body and only experiences a small variance in its location. This research is conducted on a free-free system where the center of mass is not restricted within the controlling body and will experience larger variances in its location. The one order of magnitude statement applies to and has been validated for cantilever systems. Further research effort is required to characterize the system modeled in this document and determine what factors affect the stability robustness of a free-free system.

One area of research currently being conducted at the Air Force Research Labs, Propulsion Directorate, is the application of micro pulsed plasma thrusters (μ PPTs) in augmenting the attitude control system of small flexible spacecraft. Future efforts

could evaluate the effectiveness of placing μ PPTs on the tip mass of a gravity gradient boom and calculate the significance of their contribution to meeting system performance requirements.

The FEM outlined in Chapter 3 would be modified to incorporate the μ PPTs as translational inputs located at the tip mass, node 101. Sensors may be placed at the tip mass to eliminate complications experienced from having non-collocated actuators and sensors.

An important consideration in this research effort is the amount of torque produced by μ PPTs. Engineering model testing of the thrusters measured average output values of 25×10^{-6} Nm. Recall the limit of the reaction wheels is set at 3 Nm, a value which can also be varied by altering the q/r ratio in the LQG/LTR process. The design parameter, R, would take the form

$$R = \begin{pmatrix} RW \\ mPPT \end{pmatrix}_{6 \times 3} \quad (5.2)$$

which can be thought of as

$$R = \begin{pmatrix} rw * I_{3 \times 3} \\ th * I_{3 \times 3} \end{pmatrix} \quad (5.3)$$

where rw and th scaling factors which can be modified until the dynamic response of the closed loop system indicates reaction wheel output of 3 Nm and μ PPT outputs of 25×10^{-6} Nm.

This analysis could determine if the μ PPTs improve or degrade system performance of the baseline model. Is anything gained by placing sensors on the tip mass? Would this allow improved control of the tip mass or orientation of the flexible appendage relative to the controlling body? Thrusters used for station keeping, orbital maneuvers, and plane changes can also be evaluated in a similar fashion and would

allow a combining of attitude dynamics presented in this study with efforts in orbital dynamics.

Appendage dynamics is another area where further research efforts may be focused. The Simulink model used in this research currently plots measured outputs. It is possible to analyze tip mass deflection and appendage deformation shapes without measuring the outputs in Simulink. Numerical integrations may be performed within a Matlab program to propagate the system forward in time. The time history of the modal coordinates, η , could then be transformed back to state variables. Plots of the physical states would provide insight on how tip mass deflection changes as the controlling body moves. Optimal configurations of the controlling body, flexible appendage, and tip mass could be evaluated against design and mission requirements needed for such missions where pointing of the tip of the appendage is a primary concern while the controlling body is only utilized to reach predetermined pointing requirements.

Studying the motion of the node points along the appendage will open up areas for future study in micro-meteoroid impacts at various locations along the appendage. Also, the FEM is an effective testbed in furthering efforts in technological advances in sensors and actuators imbedded within the appendage material by providing a detailed system dynamic model which is easily modified to accommodate placement of these sensors and actuators through the state space matrices, B and C.

This research effort described in this document, and future research efforts utilizing the findings from this analysis, will strengthen the field of study in attitude control of small flexible structures. The near term utilization of this study will support both commercial and governmental efforts in small flexible spacecraft and appendages constructed from shape memory composites. Future impacts of these findings are as limitless as space itself.

Bibliography

- [1] “ASM Materials Handbook,” 1990. Materials Park, Ohio.
- [2] Agnes, Gregory. “MECH533: Intermediate Space Flight Dynamics Class Notes.” Air Force Institute of Technology, Spring 1998.
- [3] Agrawal, B. N. Design of Geosynchronous Spacecraft. Prentice-Hall, Inc.: Englewood Cliffs, NJ, 1986.
- [4] Agrawal, B. N. and Jr. R. J. Watkins. “Experimental Verification of Attitude Control Techniques for Flexible Spacecraft.” 42nd Congress of the International Astronautical Federation. 5-11 October 1991.
- [5] Air, National and Space Museum Smithsonian, “Explorer I, Milestones of Flight,” 2006. <http://www.nasm.si.edu/exhibitions/GAL100/exp1.html>.
- [6] Akella, M. R., Valdivia A. and G. R. Kotamrajo. “Velocity-Free Attitude Controllers Subject to Actuator Magnitude and Rate Saturations,” Journal of Guidance, Control, and Dynamics, 28(4):659–666 (July-August 2005).
- [7] Albassam, B. A. “Optimal Near-Minimum-Time Control Design for Flexible Structures,” Journal of Guidance, Control, and Dynamics, 25(4):618–625 (2002).
- [8] Anderson, B. D. O. and J. B. Moore. Optimal Control: Linear Quadratic Methods. Prentice-Hall, Inc.: Englewood Cliffs, NJ, 1990.
- [9] Anderson, P. W. “Absence of Diffusion in Certain Random Lattices,” Physical Review, 109:1492–1505 (1958).
- [10] Antsaklis, P. J., Passino K. M. and S. J. Wang. “Towards Intelligent Autonomous Control Systems: Architecture and Fundamental Issues,” Journal of Intelligent Robotic Systems, 1:315–342 (1989).
- [11] Ashley, S. “Shape-Shifters,” Scientific American (May 2001).
- [12] Bailey, T. and J. E. Hubbard. “Distributed Piezoelectric-Polymer Active Vibration Control of a Cantilever Beam,” Journal of Guidance, Control and Dynamics, 8(5):605–611 (1985).
- [13] Balas, M. “Feedback Control of Flexible Systems,” IEEE Transactions on Automatic Control, AC-23(4):673–679 (1978).

- [14] Balas, M. J. “Modal Control of Certain Flexible Dynamic Systems,” SIAM Journal of Control and Optimization, 16:450–462 (1978).
- [15] Balas, M. J. “Trends in Large Space Structure Control Theory: Fondest Hopes, Wildest Dreams,” IEEE Transactions on Automatic Control, AC-27(3):522–535 (June 1982).
- [16] Bascetta, L. and P. Rocco. “Modelling Flexible Manipulators with Motors at the Joints,” Mathematical and Computer Modelling of Dynamical Systems, 8(2):157–183 (June 2002).
- [17] Bauchau, O. A. and J. Rodriguez. “Formulation of Modal Based Elements in Nonlinear, Flexible Multibody Dynamics,” Journal of Multiscale Computational Engineering, 1(2):161–180 (2003).
- [18] Bayard, D. S., “Averaging Methods for Transient Analysis in Adaptive Control of Large Space Structures,” 4 February 1988. Jet Propulsion Laboratory, Engineering Memo EM 347-88-228.
- [19] Bayard, D. S., “Optimal Adaptive Control Design for Large Space Structures,” 21 November 1988. Jet Propulsion Laboratory, Engineering Memo EM 347-1107.
- [20] Bennighof, J. K. and S. H. M. Chang. “Closed Loop Near Minimum Time Pulse Response Based Control of Flexible Spacecraft.” AIAA Guidance, Navigation and Control Conference. 705–716. 10 August 1992. A92-55151.
- [21] Blelloch, P. A. and D. L. Mingori. “Modified LTR Robust Control for Flexible Structures.” Proceedings of the AIAA Guidance, Navigation and Control Conference. 314–318. 1986.
- [22] Bode, H. W. Network Analysis and Feedback Amplifier Design. New York: Van Nostrand, 1945.
- [23] Bodineau, G., Boulade S. and B. Frapard. “Robust Control of Large Flexible Appendages for Future Space Missions.” Proceedings of the 6th Conference on Dynamics and Control of Systems and Structures in Space. 251–260. 18-22 July 2004.
- [24] Bolandi, H. and A. Badpi. “Three Axes Satellite Attitude Control Stabilized Using Adapted Gravity Gradient and Magnetic Torquers Based Consumed Energy.” 11th Proceeding of the Persian Electrical Conference. June 2004.
- [25] Book, W. J. “Recursive Lagrangian Dynamics of Flexible Manipulator Arms,” International Journal of Robotics Research, 3(3):87–101 (1984).
- [26] Bryson, A. E. Applied Linear Optimal Control: Examples and Algorithms. Cambridge University Press: United Kingdom, 2002.
- [27] Bryson, A. E., Jr. Control of Spacecraft and Aircraft. Princeton University Press: Princeton, NJ, 1994.

- [28] Bryson, A. E., Jr. Dynamic Optimization. Addison Wesley Longman, Inc.: Menlo Park, CA, 1999.
- [29] Bryson, A. E., Jr. and Y. C. Ho. Applied Optimal Control: Optimization, Estimation and Control. Hemisphere Publishing Corporation, Washington DC, 1975.
- [30] Bryson, Arthur E., Jr. “Notes on Guidance and Control.” American Astronautical Society, Rocky Mountain Guidance and Control Conference. February 1983.
- [31] Buttrill, C. S., Zeiler T. A. and P. D. Arbuckle. “Nonlinear Simulation of a Flexible Aircraft in Maneuvering Flight.” AIAA Flight Simulation Technologies Conference. 122–133. 17-19 August 1987. 87-2501-CP.
- [32] Cai, G.-P., Hong J.-Z. and S. Yang. “Dynamic Analysis of a Flexible Hub-Beam System with Tip Mass,” Mechanics Research Communications, 32(2):173–190 (March-April 2005).
- [33] Calise, A., Hovakimyan N. and M. Idan. “Adaptive Output Feedback Control of Nonlinear Systems Using Neural Networks,” Automatica, 37(8):1201–1211 (2001).
- [34] Calise, A. J., Yang B. and J. I. Craig. “Augmenting Adaptive Approach to Control of Flexible Systems,” Journal of Guidance, Control, and Dynamics, 27(3):387–396 (May-June 2004).
- [35] Campbell, J. E. et al. “Staged Microgravity Deployment of a Pressurizing Scale Model Spacecraft.” 43rd AIAA/ASME/ASCE/AHS/ASC Structures, Structural Dynamics, and Materials Conference and Exhibit. April 22-25 2002. AIAA 2002-1455.
- [36] Campbell, D., Lake M. S. and N. Wilder. “Development of a Shape Memory Coilable Boom Using Elastic Memory Composite Material.” ASCE Earth and Space 2004 Conference. March 2004.
- [37] Canavin, J. R. “The Control of Spacecraft Vibrations Using Multivariable Output Feedback.” AIAA/AAS Astrodynamics Conference. August 7-9 1978. AIAA paper no. 78-1419.
- [38] Canavin, J. R. and P. W. Likins. “Floating Reference Frames for Flexible Spacecraft,” Journal of Spacecraft and Rockets, 14(12):724–732 (December 1977).
- [39] Cavin, R. K. and A. R. Dusto. “Hamilton’s Principle: Finite-Element Methods and Flexible Body Dynamics,” AIAA Journal, 15(12):1684–1690 (December 1977).
- [40] Chalhoub, N. G. and L. Chen. “A Structural Flexibility Transformation Matrix of Modelling Open-Kinematic Chains with Revolute and Prismatic Joints,” Journal of Sound and Vibration, 218(1):45–63 (November 1998).
- [41] Chandra, Singh and Gupta. “Damping Studies in Fiber-Reinforced Composites - A Review,” Composite Structures, 46:41–51 (1999).

- [42] Chen, B. M., Saberi A. and P. Sannuti. “Necessary and Sufficient Conditions for a Nonminimum Phase Plant to have a Recoverable Target Loop – A Stable Compensator Design for LTR,” Automatica, 28(3):493–507 (1992).
- [43] Chen, B. M., Saberi A.-Bingulac S. and P. Sannuti. “Loop Transfer Recovery for Non-Strictly Proper Plants,” Control-Theory and Advanced Technology, 6(4):573–594 (December 1990).
- [44] Chobotov, Vladimir A. Spacecraft Attitude Dynamics and Control. Krieger Publishing Company: Malabar, FL, 1991.
- [45] Clagett, C. E. et al. “The Attitude Control System Design for the Submillimeter Wave Astronomy Satellite.” Proceedings of the 9th Annual AIAA/USU Conference on Small Satellites. September 1995.
- [46] Clem, A. L., Smith S. W. and J. A. Main. “Experimental Results Regarding the Inflation of Unfolding Cylindrical Tubes.” 42nd AIAA/ASME/ASCE/AHS/ASC Structures, Structural Dynamics, and Materials Conference and Exhibit. April 16-19 2001. AIAA 2001-1264.
- [47] Command, Air Force Space, “Milstar Satellite Communications System Fact Sheet,” February 2003. Public Affairs Office; 150 Vandenberg St., Suite 1105; Peterson AFB, CO 80914-4500.
- [48] Connolly, A. J., Green M. Chicharo J. F. and R. R. Bitmead. “The Design of LQG and H_∞ Controllers for Use in Active Vibration Control and Narrow Band Disturbance Rejection.” 34th IEEE Conference on Decision and Control. 1995.
- [49] Crawford, R. F. “Strength and Efficiency of Deployable Booms for Space Applications.” AAS/AIAA Variable Geometry and Expandable Structures Conference. April 21-23 1971. AIAA paper no. 71-396.
- [50] Croopnick, S. R., Lin Y. H. and R. R. Strunce. “A Survey of Automatic Control Techniques for Large Space Structures.” Proceedings of 8th IFAC Symposium on Automatic Control in Space. 275–284. 1979.
- [51] Cruz, J. B. Feedback Systems. New York: McGraw-Hill, 1972.
- [52] Cruz, J. B. and W. R. Perkins. “A New Approach to the Sensitivity Problem in Multivariable Feedback System Design,” IEEE Transactions on Automatic Control, AC-9(4):216–223 (July 1964).
- [53] Cruz, J. B. et al. “A Relationship Between Sensitivity and Stability of Multivariable Feedback Systems,” IEEE Transactions on Automatic Control, AC-26:66–74 (February 1981).
- [54] December, Brian Dell, “ACL-97-002 A Study of Methods to Improve the Disturbance Rejection Properties of LQG/LTR.”
- [55] DeSouza, L. C. G., Kuga H. K. and A. Fenili. “Elastic Parameters Estimation of a Rigid-Flexible Satellite Using a Kalman Filter.” Proceedings of the 6th Conference on Dynamics and Control of Systems and Structures in Space. 271–282. 18-22 July 2004.

- [56] DiStefano, J. J., Stubberud A. R. and I. J. Williams. Schaum's Outline of Theory and Problems of Feedback and Control Systems (2nd Edition). McGraw-Hill, Inc.: New York, 1990.
- [57] Doyle, J. C. "Robustness of Multiloop Linear Feedback Systems." Proceedings of the IEEE Conference on Decision and Control. 12–17. January 1979.
- [58] Doyle, J. C. and G. Stein. "Multivariable Feedback Design: Concepts for a Classical/Modern Synthesis," IEEE Transactions on Automatic Control, AC-26(1):4–16 (February 1981).
- [59] Dusto, A. et al. A Method for Predicting the Stability Characteristics of an Elastic Airplane, Volume 1: FLEXSTAB Theoretical Description. Technical Report, Boeing Commercial Airplane Co., October 1974. NASA-CR-114712.
- [60] Dwyer, T. A. W. "The Control of Angular Momentum for Asymmetric Rigid Bodies," IEEE Transactions on Automatic Control, AC-27(3):42–44 (June 1982).
- [61] Fay, J. P. and C. R. Steele. "Bending and Symmetric Pinching of Pressurized Tubes." IUTAM-IASS Symposium on Deployable Structures: Theory and Applications. September 1998.
- [62] Fennell, M., Untalam V. and M. Lee. "The Attitude Control System Design for the Wide-Field Infrared Explorer Mission." Proceedings of the 11th Annual AIAA/USU Conference on Small Satellites. September 1997.
- [63] Forsythe, G. E. and C. B. Moler. Computer Solutions of Linear Algebraic Systems. Englewood Cliffs, NJ: Prentice-Hall, 1967.
- [64] Franklin, G. F., Powell J. D. and A. Emami-Naeini. Feedback Control of Dynamic Systems (2nd Edition). Addison-Wesley Publishing Company: Menlo Park, CA, 1991.
- [65] Freudenberg, J. S. and D. P. Looze. "Right Half Plane Zeros and Design Tradeoffs in Feedback Systems," IEEE Transactions on Automatic Control, AC-30(6):555–565 (June 1985).
- [66] Friedland, B. Control System Design – An Introduction to State Space Methods. New York: McGraw-Hill, 1986.
- [67] Frisch, H. P. "Thermally Induced Vibrations of Long Thin-Walled Cylinders of Open Section," Journal of Spacecraft and Rockets, 7(8):897–905 (August 1970).
- [68] Fuller, C. R. and A. H. von Flotow. "Active Control of Sound and Vibration," IEEE Control Systems Magazine, 9–19 (1995).
- [69] Fulton, Joseph M. Attitude Control and Multimedia Representation of Air Force Institute of Technology's (AFIT's) Simulation Satellite (SIMSAT). Master's Thesis, Air Force Institute of Technology, Wright-Patterson Air Force Base, OH, March 2000.

- [70] Gall, K. et al. "Micro-Mechanisms of Deformation in Fiber Reinforced Polymer Matrix Elastic Memory Composites." 42nd AIAA/ASME/ASCE/AHS/ASC SDM Conference. April 16-19 2001. AIAA paper no. 2001-1419.
- [71] Gall, Ken et al. "Shape Memory Polymer Nanocomposites," Acta Materialia, 50:5115–5126 (2002).
- [72] George, L. E. Active Vibration Control of a Flexible Base Manipulator. Ph.D. Dissertation, School of Mechanical Engineering, Georgia Institute of Technology, August 2002.
- [73] Gerstner, E. "Shape-Memory Alloys," Nature Materials (October 2002).
- [74] Gili, P. A., Battipede M. and L. Massotti. "Modelling and Neural Control of Satellites with Flexible Appendages." Proceedings of the 6th Conference on Dynamics and Control of Systems and Structures in Space. 489–500. 18-22 July 2004.
- [75] Glabisz. "Vibration and Stability of a Beam with Elastic Supports and Concentrated Masses Under Conservative and Non-Conservative Forces," Computers and Structures, 70:305–313 (1999).
- [76] Gluck, R. "Equations of Motion of Flexible Spacecraft." AIAA 8th Aerospace Sciences Meeting. 19-21 January 1970.
- [77] Gorinevsky, Dimitry and G. Vukovich. "Nonlinear Input Shaping Control of Flexible Spacecraft Reorientation Maneuver," Journal of Guidance, Control, and Dynamics, 21(2):264–270 (March-April 1998).
- [78] Grassi. "Attitude Determination and Control for a Small Remote Sensing Satellite," Acta Astronautica, 40:675–681 (1997).
- [79] Greenwood, Donald T. Classical Dynamics. Dover Publications, Inc.: Mineola, New York, 1997.
- [80] Griffin, Michael D. and James R. French. Space Vehicle Design. American Institute of Aeronautics and Astronautics, Inc.: Washington, DC, 1991.
- [81] Griffith, D. T., Junkins J. L. and J. D. Turner. "Automatic Generation and Integration of Equations of Motion for Linked Mechanical Systems." Proceedings of the 6th Conference on Dynamics and Control of Systems and Structures in Space. 693–706. 18-22 July 2004.
- [82] Grimble, M. J. and T. J. Owens. "On Improving the Robustness of LQ Regulators," IEEE Transactions on Automatic Control, AC-31(1):54–55 (January 1986).
- [83] Gupta, M. J. "Frequency Shaped Cost Functionals: Extension of Linear Quadratic Gaussian Design Methods," Journal of Guidance and Control, 3(6):529–535 (1980).
- [84] Hailey, J. A., Sortun C. D. and B. N. Agrawal. "Experimental Verification of Attitude Control Techniques for Slew Maneuvers of Flexible Spacecraft." AIAA Guidance, Navigation and Control Conference. 653–667. 10-12 August 1992.

- [85] Haug, E. et al. "The Numerical Simulations of the Inflation Process of Space Rigidized Antenna Structures." Proceeding of the International Conference on Spacecraft Structures and Mechanical Testing. April 1991.
- [86] Hibbeler, R. C. Mechanics of Materials (4th Edition). Prentice Hall: Upper Saddle River, NJ, 2000.
- [87] Horowitz, I. M. Synthesis of Feedback Systems. New York: Academic, 1963.
- [88] Hovakimyan, N., Lee H. and A. Calise. "On Approximate NN Realization of an Unknown Dynamic System from Its Input-Output History." Proceedings of the American Control Conference. 919–923. 2000.
- [89] Hughes, P. C. "Dynamics of Flexible Space Vehicles with Active Attitude Control," Celestial Mechanics, 9:21–39 (1974).
- [90] Hughes, Peter C. Spacecraft Attitude Dynamics. John Wiley and Sons: New York, 1986.
- [91] Hurty, W. C. "Dynamic Analysis of Structural Systems Using Component Modes," AIAA Journal, 3:678–685 (May 1965).
- [92] Ioannou, P. and P. Kokotovic. Adaptive Systems with Reduced Models. Springer-Verlag, Berlin, 1983.
- [93] Ioannou, P. and J. Sun. Robust Adaptive Control. Prentice-Hall, Upper Saddle River, NJ, 1996.
- [94] Izzo, D., Pettazzi L. and R. Bevilacqua. "Taking Into Account Flexibility in Attitude Control." Proceedings of the 6th Conference on Dynamics and Control of Systems and Structures in Space. 459–466. 18-22 July 2004.
- [95] Izzo, D., Pettazzi L. and C. Valente. "A Comparison Between Models of Flexible Spacecraft." Proceedings of the 6th Conference on Dynamics and Control of Systems and Structures in Space. 241–250. 18-22 July 2004.
- [96] Jilla, Cyrus D. and David W. Miller. "Satellite Design: Past, Present, and Future." 1997.
- [97] Johnson, E. N. Limited Authority Adaptive Flight Control. Ph.D. Dissertation, School of Aerospace Engineering, Georgia Institute of Technology, Atlanta, December 2000.
- [98] Joshi, S. M., Armstrong E. S. and N. Sundararajan. "Application of LQG/LTR Technique to Robust Controller Synthesis for a Large Flexible Space Antenna," NASA Technical Publication 2560, 61 (September 1986).
- [99] Joshi, S. M. "Robustness Properties of Collocated Controllers for Flexible Spacecraft," Journal of Guidance, Control, and Dynamics, 9(1):85–91 (1986).
- [100] Junkins, J. L., editor. Mechanics and Control of Large Flexible Structures, 129. Progress in Astronautics and Aeronautics. American Institute of Aeronautics and Astronautics, Inc.: Washington, DC, 1990.

- [101] Junkins, J. L. and Y. Kim. Introduction to Dynamics and Control of Flexible Structures. AIAA: Washington, D. C., 1993.
- [102] Junkins, J., Rahman Z. and H. Bang. “Near-Minimum-Time Control of Distributed Parameter Systems: Analytical and Experimental Results,” Journal of Guidance, Control, and Dynamics, 14(2):406–415 (1991).
- [103] Kakad, Y. P. “Dynamics and Control of Slew Maneuver of Large Flexible Spacecraft.” AIAA Guidance, Navigation, and Control Conference. 629–634. 18-20 August 1986. A86-47401.
- [104] Kang, B. S. and J. K. Mills. “Dynamic Modelling of Structurally-Flexible Planar Parallel Manipulator,” Robotica, 20:329–339 (May-June 2002).
- [105] Kauffman, G. and Isaac Mayo. “Memory Metal,” Chem Matters, 4–7 (October 1993).
- [106] Kazerooni, H., Sheridan T. B. and P. K. Houpt. “On the Loop Transfer Recovery,” International Journal of Control, 43(3):981–986 (March 1986).
- [107] Khorrami, F., Jain S. and A. Tzes. “Experiments on Rigid Body-Based Controllers with Input Preshaping for Two-Link Flexible Manipulator,” IEEE Transactions on Robotics and Automation, 10(1):55–65 (1994).
- [108] Kosut, R. L. and H. Salzwedel. “Stability and Robustness of Control Systems for Large Space Structures.” Proceedings of the Third VPI/SU/AIAA Symposium on Dynamics and Control of Large Flexible Spacecraft, edited by L. Meirovitch. 343–364. 1981.
- [109] Kosut, R. L., Salzwedel H. and A. Emami-Naeini. “Robust Control of Flexible Spacecraft,” Journal of Guidance, Control, and Dynamics, 6(2):104–111 (1983).
- [110] Kreindler, E. “Closed-Loop Sensitivity Reduction of Linear Optimal Control Systems,” IEEE Transactions on Automatic Control, AC-13:254–262 (June 1968).
- [111] Krogstad, T. R. Attitude Control of Satellites in Clusters. Master’s Thesis, NTNU, Trondheim, June 2005.
- [112] Kwakernaak, H. “Optimal Low Sensitivity Linear Feedback Systems,” Automatica, 5:279–285 (1969).
- [113] Kwakernaak, H. “Minimax Frequency Domain Performance and Robustness Optimization of Linear Feedback Systems,” IEEE Transactions on Automatic Control, AC-30(10):994–1004 (October 1985).
- [114] Lake, Mark S. and Fred L. Beavers. “The Fundamentals of Designing Deployable Structures with Elastic Memory Composites.” 43rd Structures, Structural Dynamics, and Materials Conference. April 22-25 2002. AIAA paper no. 2002-1454.
- [115] Lake, Mark S. et al. “Application of Elastic Memory Composite Materials to Deployable Space Structures.” AIAA Space 2001 Conference and Exposition. August 28-30 2002. AIAA paper no. 2001-4602.

- [116] Lake, Mark S. et al. “Development of Coilable Longerons Using Elastic Memory Composite Material.” 43rd Structures, Structural Dynamics, and Materials Conference. April 22-25 2002. AIAA paper no. 2002-1453.
- [117] Laskin, R. A. and S. W. Sirlin. “Future Payload Isolation and Pointing System Technology,” Journal of Guidance, Control, and Dynamics, 9(4):469–477 (1986).
- [118] Laub, A. J. Linear Multivariable Control: Numerical Considerations. Technical Report, Massachusetts Institute of Technology, Electronic Systems Laboratory. Paper ; ESL-P-833, 1978.
- [119] Lavretsky, E., Hovakimyan N. and A. Calise. “Upper Bounds for Approximation of Continuous-Time Dynamics Using Delayed Outputs and Feedforward Neural Networks,” IEEE Transactions on Automatic Control, 48(9):1606–1610 (2003).
- [120] Ledesma, R. and E. Bayo. “A Non-Recursive Lagrangian Solution of the Non-Causal Inverse Dynamics of Flexible Multibody Systems: The Planar Case,” International Journal for Numerical Methods in Engineering, 36(16):2725–2741 (29 June 2005).
- [121] Lehtomaki, N., Sandell N. Jr. and M. Athens. “Robustness Results in Linear-Quadratic Gaussian Based Multivariable Control Designs,” IEEE Transactions on Automatic Control, AC-26(1):75–92 (February 1981).
- [122] Lendlein, A. and R. Langer. “Biodegradable, Elastic Shape-Memory Polymers for Potential Biomedical Applications,” Science, 296(5573):1673–1676 (May 31 2002).
- [123] Levine, Alan J. The Missile and the Space Race. Praeger Publishers: London, 1994.
- [124] Li, Y. Adaptive Isolations of Vibration and Noise. Ph.D. Dissertation, Clemson University, 2005.
- [125] Liang, C., Rogers C. A. and E. Malafew. “Investigation of Shape Memory Polymers and Their Hybrid Composites,” Journal of Intelligent Material Systems and Structures, 8:380–386 (April 1997).
- [126] Likins, P. W., Ohkami Y. and C. Wong. “Appendage Modal Coordinate Truncation Criteria in Hybrid Coordinate Dynamic Analysis,” Journal of Spacecraft and Rockets, 13(10):611–617 (1976).
- [127] Likins, P. W. Dynamics and Control of Flexible Space Vehicles. Technical Report, Jet Propulsion Laboratory Technical Report 32-1329, Rev. 1, January 15, 1970.
- [128] Likins, P. W. Analytical Dynamics and Nonrigid Spacecraft Simulation. Technical Report, Jet Propulsion Laboratory Technical Report 32-1593, July 15, 1974.
- [129] Likins, P. W. and G. E. Fleischer. “Results of Flexible Spacecraft Attitude Control Studies Utilizing Hybrid Coordinates,” Journal of Spacecraft and Rockets, 8(3):264–273 (March 1971).

- [130] Lin, Chun-Liang. “Perturbation Analysis for Flexible System Control,” Journal of Guidance, Control, and Dynamics, 18(3):633–635 (May-June 1995).
- [131] Liu, Q. and B. Wie. “Robust Time-Optimal Control of Uncertain Flexible Spacecraft,” Journal of Guidance, Control, and Dynamics, 15(3):597–604 (1992).
- [132] LoBosco, D. M. Integrated Modeling of Optical Performance for the Terrestrial Planet Finder Structurally Connected Interferometer. Master’s Thesis, Massachusetts Institute of Technology, 2004.
- [133] Lomas, Norman S. “Comparing Model Simulations with Flight Performance of Spacecraft Deployable Appendages,” Journal of Guidance, Control, and Dynamics, 24(5):933–938 (September-October 2001).
- [134] Lombardi, A. V. “The Effect of the Non-Conservative Forces on the Attitude Dynamics of a Variable Geometry Satellite,” Aerotecnica Missili e Spazio, 81:26–33 (January 2002).
- [135] Ltd., Surrey Satellite Technologies, 2004. <http://www.sstl.co.uk>.
- [136] MacFarlane, A. G. J. and B. Kouvaritakis. “A Design Technique for Linear Multivariable Feedback Systems,” International Journal of Control, 23:837–874 (June 1977).
- [137] MacFarlane, A. G. J. and I. Postlethwaite. “The Generalized Nyquist Stability Criterion and Multivariable Root Loci,” International Journal of Control, 23:81–128 (January 1977).
- [138] Mackison, D. L. Guaranteed Cost Control of Flexible Space Structures. Ph.D. Dissertation, University of Colorado, Boulder, CO, 1988.
- [139] Mackison, D. L. “Low Order Closed Loop Compensation for Satellite Attitude Control/Determination Using Linear Quadratic Regulator/Loop Transmission Recovery (LQG/LTR) Methods.” AIAA/AAS Space Flight Mechanics Meeting. 11–31. January 23–26 2000. AAS 00-102.
- [140] Mackison, D. L. “Further Results in Reduced Order Compensators for Dynamics Systems Using LQG/LTR Methods.” 15th AAS/AIAA Astrodynamics Specialist Conference. August 2005. AAS 05-422.
- [141] Mackison, D. L. “Results of Generating Classical Compensators vis Linear Quadratic Design with a Minimum Realization of the Compensator.” 15th AAS/AIAA Space Flight Mechanics Conference. January 23–27 2005. AAS 05-166.
- [142] Maghami, Peiman G., Sparks D. W. and K. B. Lim. “Fault Accommodation in Control of Flexible Systems,” Journal of Guidance, Control, and Dynamics, 21(3):500–507 (May-June 1998).
- [143] Martin, G. D. and A. E. Bryson. “Attitude Control of a Flexible Spacecraft,” Journal of Guidance and Control, 13:37–41 (January-February 1980).
- [144] MathWorks. Control System Toolbox User’s Guide (5 Edition). 2005.

- [145] Medanic, J., Tharp H. S. and W. R. Perkins. "Pole Placement by Performance Criterion Modification," IEEE Transactions on Automatic Control, 33(5):469–472 (May 1988).
- [146] Meirovitch, L. "Modeling and Control of Distributed Structures." Proceedings of the Workshop on Applications of Distributed Systems Theory to the Control of Large Space Structures, edited by G. Rodriguez. 1–30. 1983. JPL Publication 83-46.
- [147] Meirovitch, L. Elements of Vibration Analysis (2nd Edition). McGraw-Hill, Inc: Boston, MA, 1986.
- [148] Meirovitch, L. Dynamics and Control of Structures. John Wiley and Sons: New York, 1990.
- [149] Meirovitch, L. and H. Oz. "An Assessment of Methods for the Control of Large Space Structures." Proceedings of the Joint Automatic Control Conference. 34–41. 1979.
- [150] Mester, S. S. and H. Benaroya. "Localization in Near Periodic Structures." 35th AIAA/ASME/ASCE/AHS/ASC Structures, Structural Dynamics, and Materials Conference. 1488–1496. Washington, DC: AIAA, 1994.
- [151] Middleton, R. and G. Goodwin. Digital Control and Estimation: A Unified Approach. Prentice-Hall, Inc.: Englewood Cliffs, New Jersey, 1990.
- [152] Misra, P. and R. V. Patel. "Numerical Algorithms for Eigenvalue Assignment by Constant and Dynamic Output Feedback," IEEE Transactions on Automatic Control, AC-34(6):577–588 (1989).
- [153] Miyazaki, Y. and M. Uchiki. "Deployment Dynamics of Inflatable Tube." 43rd AIAA/ASME/ASCE/AHS/ASC Structures, Structural Dynamics, and Materials Conference and Exhibit. April 22-25 2002. AIAA 2002-1254.
- [154] Modi, V. J. "Attitude Dynamics of Satellites with Flexible Appendages - A Brief Review," Journal of Spacecraft and Rockets, 11(11):743–751 (1974).
- [155] Moheimani, S. O. R., Hemanshu R. P. and I. R. Peterson. "Spatial Control for Active Vibration Control of Piezoelectric Laminates." Proceedings of the 37th IEEE Conference on Decision and Control. 4308–4313. 16-18 December 1998.
- [156] Moore, J. B. and L. Xia. "Loop Recovery and Robust State Estimate Feedback Designs," IEEE Transactions on Automatic Control, AC-36(6):512–517 (June 1987).
- [157] Morrissey, J. R., Quinn T. H. and G. Parcelli. "Attitude Determination and Control Subsystem for Spartan Lite Spacecraft." Proceedings of the 11th Annual AIAA/USU Conference on Small Satellites. September 1997.
- [158] Murphey, T. W., Meink T. and M. M. Mikulas. "Some Micromechanics Considerations in the Folding of Rigidizable Composite Materials." 42nd AIAA/ASME/ASCE/AHS/ASC SDM Conference. April 16-19 2001. AIAA paper no. 2001-1418.

- [159] NASA/SP-8024, "Spacecraft Gravitational Torques," May 1969. NASA Space Vehicle Design Criteria (Guidance and Control).
- [160] NASA/SP-8065, "Tubular Spacecraft Booms(Extendible, Reel Stored," February 1971. NASA Space Vehicle Design Criteria (Guidance and Control).
- [161] Nurre, D. S., Ryan R. S. Scofield H. N. and J. L. Sims. "Dynamics and Control of Large Space Structures," Journal of Guidance, Control, and Dynamics, 7(5):514–526 (1984).
- [162] Oakley, C. M. and R. H. Canon. "Theory and Experiments in Selecting Mode Shapes for Two-Link Flexible Manipulators." Proceedings of First International Symposium on Experimental Robotics. June 1989.
- [163] O'Dell, B. D. and E. A. Misawa. "Obtaining Uniform Singular Values of Augmented Systems Using LQG/LTR," Proceedings of the American Control Conference, 1 (1995).
- [164] Ohkami, Y. and P. W. Likins. "The Influence of Spacecraft Flexibility on System Controllability and Observability." 6th IFAC Symposium on Automatic Control in Space. August 1974.
- [165] Palmer, P. L., Mikkola S. and Y. Hashida. "A Simple High Accuracy Integrator for Spacecraft Attitude Systems." AIAA Guidance, Navigation, and Control Conference. 16-19 August 2004. AIAA paper no. 2004-5339.
- [166] Pao, L. Y., Chang T. N. and E. Hou. "Input Shaper Design for Minimizing the Expected Level of Residual Vibration in Flexible Structures." 1997 American Control Conference. 3542–3546. Evanston, IL: American Automatic Control Council, 1997.
- [167] Park, J. H. "Dynamic Analysis of Constrained Multibody Systems Using Hybrid Coordinates." The 2nd Asian Conference on Multibody Dynamics. 2-4 August.
- [168] Peek, M. and P. J. Antsaklis. "Parameter Learning for Performance Adaptation," IEEE Control Systems Magazine (December 1990).
- [169] Perkins, W. R. and J. B. Cruz. "Feedback Properties of Linear Regulators," IEEE Transactions on Automatic Control, AC-16:659–664 (December 1971).
- [170] Pfeiffer, F. "A Feedforward Decoupling Concept for the Control of Elastic Robots," Journal of Robotic Systems, 6(4):407–416 (1989).
- [171] Piedboeuf, J. C. and B. Moore. "On the Foreshortening Effects of a Rotating Flexible Beam Using Different Modeling Methods," Mechanics of Structures and Machines, 30(1):83–102 (2002).
- [172] Porcelli, G. "Attitude Control of Flexible Space Vehicles," AIAA Journal, 10(6):807–812 (1972).
- [173] Racca, G. D. et al. "SMART-1 Mission Description and Development Status," Planetary and Space Science, 50:1323–1337 (2002).

- [174] Ridgely, D. B. and S. S. Banda. Introduction to Robust Multivariable Control. Technical Report, Report No. AFWAL-TR-3120, Flight Dynamics Laboratories, Air Force Systems Command, Wright-Patterson AFB, OH, 1986.
- [175] Ridgely, D. B. et al. "Linear-Quadratic-Gaussian with Loop Transfer Recovery Methodology for an Unmanned Aircraft," Journal of Guidance, Control, and Dynamics, 10(1):82–89 (1986).
- [176] Rimrott, F. P. J. Introductory Attitude Dynamics. Springer-Verlag: New York, 1989.
- [177] Robinson, A. C. "A Survey of Optimal Control of Distributed-Parameter Systems," Automatica, 7:371–388 (1971).
- [178] Rogers, C. A. "Intelligent Materials," Scientific American, 154–157 (September 1995).
- [179] Rosenbrock, H. H. Computer-Aided Control System Design. New York: Academic, 1974.
- [180] Saada, Adel S. Elasticity Theory and Applications (2nd Edition). Krieger Publishing Company: Florida, 1993.
- [181] Saberi, A. and P. Sannuti. "Observer Design for Loop Transfer Recovery and for Uncertain Dynamical Systems," IEEE Transactions on Automatic Control, AC-35(8):878–897 (1990).
- [182] Safonov, M. G., Laub A. J. and G. Hartmann. "Feedback Properties of Multivariable Systems: The Role and Use of Return Difference Matrix," IEEE Transactions on Automatic Control, AC-26:47–65 (1981).
- [183] Safonov, M. G. and M. K. H. Fan. "Editorial: Special Issue on Multivariable Stability Margin," International Journal of Robust and Nonlinear Control, 7:97–103 (1997).
- [184] Sanner, R. and J. Slotine. "Gaussian Networks for Direct Adaptive Control," IEEE Transactions on Neural Networks, 3(6):837–864 (1992).
- [185] Schwertassek, R., Wallrapp O. and A. A. Shabana. "Flexible Multibody Simulation and Choice of Shape Functions," Nonlinear Dynamics, 20:361–380 (1999).
- [186] Sellers, Jerry J. Understanding Space: An Introduction to Astronautics (2nd Edition). McGraw-Hill Companies, Inc: New York, 2000.
- [187] Sesak, J. R. "Suppressed Mode Damping for Model Error Sensitivity Suppression of Flexible Spacecraft Controllers." Proceedings of the AIAA Guidance and Control Conference. 27–32. 1980.
- [188] Sesak, J. R. and R. V. Halstenberg. "Decentralized Elastic Body and Rigid Body Control by Modal Error Sensitivity Suppression." Proceedings of the Joint Automatic Control Conference. 1980. Paper FA1-D.

- [189] Sesak, J. R. and P. Likins. "Model Error Sensitivity Suppression: Quasi-Static Optimal Control for Flexible Structures." Proceedings of the 18th IEEE Conference on Decision and Control. 207–213. 1979.
- [190] Sesak, J. R., Likins P. and T. Coradetti. "Flexible Spacecraft Control by Model Error Sensitivity Suppression," Journal of Astronautical Sciences, 27(2):131–156 (1979).
- [191] Shabana, A. A. "Resonance Conditions and Deformable Body Coordinate Systems," Journal of Sound and Vibration, 192(1):389–398 (1996).
- [192] Shabana, A. A. "Flexible Multibody Dynamics: Review of Past and Recent Developments," Multibody System Dynamics, 1:189–222 (1997).
- [193] Shahian, B. and M. Hassul. Control System Design Using MATLAB. Prentice-Hall, Inc.: Englewood Cliffs, New Jersey, 1993.
- [194] Sievers, L. A. and A. H. von Flotow. "Linear Control Design for Active Vibration Isolation of Narrow Band Disturbances." 27th IEEE Conference on Decision and Control. 1988.
- [195] Sievers, L. A. and A. H. von Flotow. "Comparison of Two LQG-Based Methods for Disturbance Rejection." 28th IEEE Conference on Decision and Control. 1989.
- [196] Sievers, L. A. and A. H. von Flotow. "Comparison and Extensions of Control Methods for Narrow-Band Disturbance Rejection," IEEE Transactions on Signal Processing, 40:2377–2391 (1992).
- [197] Singer, N. C. and W. P. Seering. "Preshaping Command Inputs to Reduce System Vibrations," Journal of Dynamic Systems, Measurement and Control, 115(1):76–82 (1990).
- [198] Singh, S. K., Gran R. and B. N. Agrawal. "Comparison of Different Attitude Control Schemes for Large Communication Satellites." AIAA Guidance, Navigation and Control Conference. August 1987.
- [199] Singh, T. and S. R. Vadali. "Robust Time-Optimal Control: Frequency Domain Approach," Journal of Guidance, Control, and Dynamics, 17(2):346–353 (1994).
- [200] Singhose, W. E., Porter L. J. and N. P. Singer. "Vibration Reduction Using Multi-Hump Extra-Insensitive Input Shapers." 1995 American Control Conference. 3830–3834. Evanston, IL: American Automatic Control Council, 1995.
- [201] Skelton, R. E. and P. W. Likins. "On the Use of Model Error Systems in the Control of Large Scale Linearized Systems." Proceedings of the IFAC Symposium on Large Scale Systems, Theory and Applications. 641–650. June 1976.
- [202] Skelton, R. E. and P. W. Likins. "Orthogonal Filters for Model Error Compensation in the Control of Nonrigid Spacecraft," Journal of Guidance and Control, 1(1):41–49 (1978).

- [203] Smith, O. J. M. "Posicast Control of Damped Oscillatory Systems," Proceedings of the IRE, 1249–1255 (1957).
- [204] Sosnitskii. "The Stabilization of the Equilibrium of Conservative Systems Using Gyroscopic Forces," Journal of Applied Mathematics and Mechanics, 64:53–63 (2000).
- [205] Space Systems Research Center, United States Air Force Academy, CO. FalconSAT-3 Attitude Determination and Control System Interface Control Document (B Edition), February 2004. in house document.
- [206] Space Systems Research Center, United States Air Force Academy, CO. FalconSAT-3 Boom System Critical Design Review, 15 June 2004.
- [207] Space Systems Research Center, United States Air Force Academy, CO. FalconSAT-3 Critical Design Review, February 2004. in house document.
- [208] Space Systems Research Center, United States Air Force Academy, CO. FalconSAT-3 Flat Plasma Spectrometer Interface Control Document (B Edition), February 2004. in house document.
- [209] Space Systems Research Center, United States Air Force Academy, CO. FalconSAT-3 Plasma Local Anomalous Noise Environment Interface Control Document (B Edition), February 2004. in house document.
- [210] Spangers, Greg G., "Micro Pulsed Plasma Thruster Having Coaxial Cable Segment Propellant Modules," August 7 2001. Patent Number US 6,269,629.
- [211] Spores, R. A. and M. Birkan. "The USAF Electric Propulsion Research Program." 38th Joint Propulsion Conference. July 2002. AIAA paper no. 02-3558.
- [212] Stefani, R. T., Savant C. J. Shahian B. and G. H. Hostetter. Design of Feedback Control Systems (3rd Edition). Saunders College Publishing: Boston, 1994.
- [213] Stein, G. and M. Athans. "The LQG/LTR Procedure for Multivariable Feedback Control Design," IEEE Transactions on Automatic Control, AC-32(2):105–114 (February 1987).
- [214] Steyn, W. H. A Multi-Mode Attitude Determination and Control System for Small Satellites. Ph.D. Dissertation, University of Stellenbosch, 1995.
- [215] Subudhi, B. and A. S. Morris. "Dynamic Modelling, Simulation and Control of a Manipulator with Flexible Links and Joints," Robotics and Autonomous Systems, 41(4):257–270 (December 2002).
- [216] Sundararajan, N., Joshi S. M. and E. S. Armstrong. "Robust Controller Synthesis for a Large Flexible Space Antenna," Journal of Guidance, Control, and Dynamics, 10(2):201–208 (March-April 1987).
- [217] Sundararajan, N. and J. B. Cruz. "Sensitivity Reduction in Time-Varying Linear and Nonlinear Systems," International Journal of Control, 15:937–943 (1972).

- [218] Sweeting, M. N. "UoSAT - An Investigation into Cost-Effective Spacecraft Engineering," The Journal of the Institution of Electrical and Radio Engineers, 52(8/9):363-378 (August-September 1982).
- [219] Tafazoli, S. and K. Khorasani. "A Flexible Spacecraft Attitude Recovery Using Feedback Linearization Approach." Proceedings of the Intelligent Systems and Control Conference. 2004.
- [220] Takahito, S. "New Modeling Method of Flexible Multibody Systems and its Application for Motion and Vibration Control." The 2nd Asian Conference on Multibody Dynamics. 2-4 August 2004.
- [221] Takawa, T., Fukuda T. and T. Takada. "Flexural-Torsion Coupling Vibration Control of Fiber Composite Cantilevered Beam by Using Piezoceramic Actuators," Smart Materials and Structures, 6(4):477-484 (August 1997).
- [222] Tallarida, Ronald J. Pocket Book of Integrals and Mathematical Formulas (2nd Edition). CRC Press: Boca Raton, 1992.
- [223] Thomson, W. T. "Spin Stabilization of Attitude Against Gravity Gradient Torque," Journal of the Astronautical Sciences, 9:31-33 (1962).
- [224] Tipler, Paul A. Physics (2nd Edition). Worth Publishers, Inc.: New York, 1982.
- [225] Tobushi, H. et al. "Shape Fixity and Shape Recovery in a Film of Shape Memory Polymer of Polyurethane Series," Journal of Intelligent Material Systems and Structures, 9:127-136 (1998).
- [226] Tsoi, S. H. H. Modeling and Simulation of Inflatable Space Structures. Master's Thesis, Department of Aeronautics and Astronautics, Stanford University, June 1997.
- [227] Tupper, M. L. et al. "Developments in Elastic Memory Composite Materials for Deployable Spacecraft Structures." 2001 IEEE Aerospace Conference. March 10-17 2001. IEEE paper no. 3673.
- [228] Turner, J. A. and J. S. Wiehn. "Sensitivity of Flexural and Torsional Vibration Modes of Atomic Force Microscope Cantilevers to Surface Stiffness Variations," Nanotechnology, 12:322-330 (28 August 2001).
- [229] Turner, J. D. and H. M. Chun. "Optimal Feedback Control of a Flexible Spacecraft During a Large Angle Rotational Maneuver." AIAA Guidance and Control Conference. 1982. 82-1589-CP.
- [230] Tyler, J. S. and F. B. Tuteur. "The Use of a Quadratic Performance Index to Design Multivariable Control Systems," IEEE Transactions on Automatic Control, AC-11(1):84-92 (January 1966).
- [231] Van Beusekom, C., Lisowski R. Fulton J. and C. Morand. "Three-Axes Attitude Determination and Control System Design for Low-Cost Micro-Satellites," IEEE Aerospace Conference, 6:2615-2628 (March 8-15 2003).

- [232] Wang, J. T. and A. R. Johnson. "Deployment Simulation of Ultra-Lightweight Inflatable Structures." 43rd AIAA/ASME/ASCE/AHS/ASC Structures, Structural Dynamics, and Materials Conference and Exhibit. April 22-25 2002. AIAA 2002-1261.
- [233] Waszak, M. R., Buttrill C. S. and D. K. Schmidt. Modeling and Model Simplification of Aeroelastic Vehicles: An Overview. Technical Report, NASA Technical Memorandum 107691, September 1992.
- [234] Waszak, M. R. and D. K. Schmidt. "On the Flight Dynamics of Aeroelastic Vehicles," Journal of Aircraft, 25(6) (June 1988).
- [235] Wertz, James R. and Wiley J. Larson. Space Mission Analysis and Design (3rd Edition). Microcosm, Inc: El Segundo, CA, 1999.
- [236] West-Vukovich, G. S., Davison E. J. and P. C. Haughes. "The Decentralized Control of Large Flexible Space Structures," Institute of Electrical and Electronics Engineer Transactions on Automatic Control, 29(10):866-879 (1984).
- [237] Wie, B. and C. T. Plescia. "Attitude Stabilization of Flexible Spacecraft During Stationkeeping Maneuvers," Journal of Guidance, Control, and Dynamics, 7:430-436 (July-August 1984).
- [238] Wie, Bong. Space Vehicle Dynamics and Control. American Institute of Aeronautics and Astronautics, Inc.: Washington, DC, 1998.
- [239] Wie, B., Lehner J. A. and C. T. Plescia. "Roll/Yaw Control of a Flexible Spacecraft Using Skewed Bias Momentum Wheels," Journal of Guidance, Control, and Dynamics, 8(4):447-453 (July-August 1985).
- [240] Wiesel, William E. Spaceflight Dynamics. McGraw-Hill Companies, Inc: New York, 1989.
- [241] Wilson, D. G. et al. "Nonlinear Adaptive Control for Slewing Flexible Active Structures," Journal of Guidance, Control, and Dynamics, 27(1):142-145 (January-February 2004).
- [242] Yang, H., Hong J. and Z. Yu. "Dynamics Modeling of a Flexible Hub-Beam System with a Tip Mass," Journal of Sound and Vibration, 266(4):759-774 (2003).
- [243] Yedavalli, R. K. "Critical Parameter Selection in the Vibration Suppression of Large Flexible Space Structures," Journal of Guidance, Control, and Dynamics, 7(3):274-278 (1984).
- [244] Yedavalli, R. K. and R. E. Skelton. "Determination of Critical Parameters in Large Flexible Space Structures with Uncertain Modal Data," ASME Journal of Dynamic Systems, Measurement, and Control, 105:238-244 (December 1983).
- [245] Yoo, W. S. et al. "Physical Experiments and Computer Simulations of a Stepped Cantilever Beam with a Hybrid Coordinate Formulation," Mechanical Based Design of Structures and Machines, 32(4):515-532 (2004).

- [246] Zee, Robert E. and Peter C. Hughes. "Mode Localization in Flexible Spacecraft: A Control Challenge," Journal of Guidance, Control, and Dynamics, 23(1):69–76 (January-February 2000).
- [247] Zhang, Z. and J. S. Freudenberg. "Loop Transfer Recovery for Nonminimum Phase Plants," IEEE Transactions on Automatic Control, 35(5):547–553 (1990).
- [248] Zhao, H. Passive, Iterative, and Repetitive Control for Flexible Distributed Parameter Systems. Ph.D. Dissertation, Pennsylvania State University, 2005.
- [249] Zheng, Y. and M. Sweeting. "Initial Mission Status Analysis of 3-Axis Stable Tsinghua-1 Microsatellite." Proceedings of the 14th Annual AIAA/USU Conference on Small Satellites. 2000.
- [250] Zhou, C., Whiteley J. R. Misawa E. A. and K. A. M. Gasem. "Application of Enhanced LQG/LTR for Distillation Column," IEEE Control Systems Magazine, 15(4):56–63 (August 1995).
- [251] Zimbelman, D., Wilmont J. and S. Evangelista. "The Attitude Control System Design for the Transition Region and Control Explorer Mission." Proceedings of the 10th Annual AIAA/USU Conference on Small Satellites. September 1996.

Appendix A

Assumed Modes Method

A.1 Assumed Modes Model

The following mathematical development is based on the work of Canavin[37] and Mackison[138] with modifications added to include torsional strain storage in the flexible appendage. To begin, consider the satellite system shown in Figure A.1.

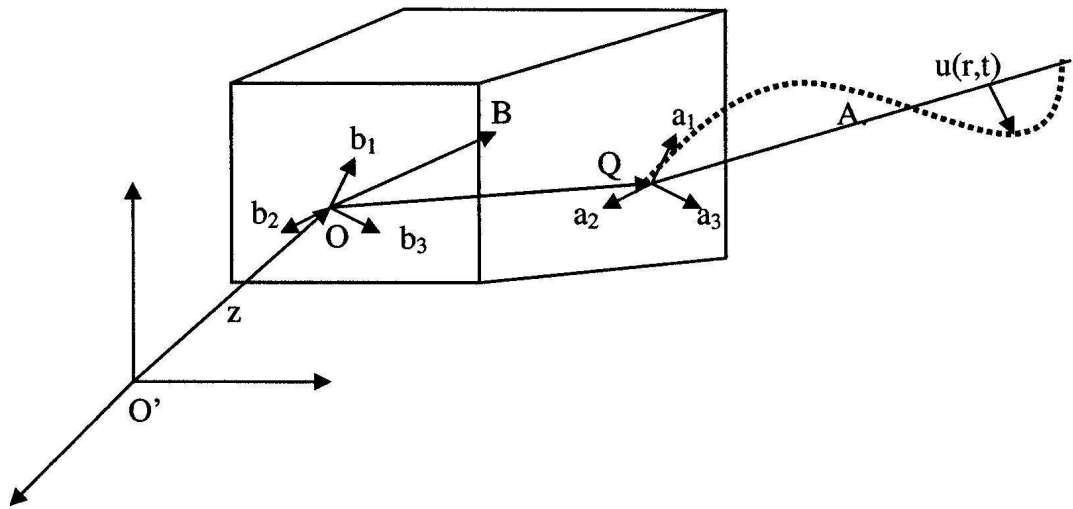


Figure A.1: Flexible Satellite Dynamic Model

with the following nomenclature:

- (b_1, b_2, b_3) : Unit vectors in the body frame.
- (a_1, a_2, a_3) : Unit vectors in the appendage frame.
- (i_1, i_2, i_3) : Unit vectors in the inertial frame.

- O: Origin of the body frame. Center of mass of the undeformed system.
- O' : Position of O at rest.
- B: Center of mass of rigid body.
- A: Center of mass of undeformed appendage.
- M^* : Total system mass.
- M: Appendage mass.
- Q: Connection point of appendage.
- $z(t)$: Motion of the system center of mass.
- R: Vector from system center of mass to beam attachment point.
- R_B : Vector of the center of mass of the rigid body with respect to a coordinate system origin in the rigid body.
- L: Coordinate of the center of mass in the undeformed body.
- $R_B = z - L$
- $\dot{R}_B = \dot{z} - \omega_B \times L$
- r_a : Vector from beam attachment point to center of mass of beam.
- z: Displacement of system center of mass from rest.
- ω_B : Inertial angular velocity of rigid body.

The basis for the development includes:

- The model is a rigid body with an attached flexible cantilevered beam.
- The beam rest position is constant relative to its base.

- The motion of the body and the beam consists of small translations and rotations.

No orthogonality requirements have been placed on the assumed mode shapes. The vibration equations are therefore coupled.

The linearized attitude matrix is

$$[\theta] = [E - \tilde{\theta}] \quad (\text{A.1})$$

Therefore, the relation between the inertial coordinates, $\{i\}$, and the body fixed coordinates, $\{b\}$, is given by

$$b = [\theta]\{i\} \quad (\text{A.2})$$

where $[\theta]$

$$[\tilde{\theta}] = \begin{pmatrix} 0 & -\theta_3 & \theta_2 \\ \theta_3 & 0 & -\theta_1 \\ -\theta_2 & \theta_1 & 0 \end{pmatrix} \quad (\text{A.3})$$

The transformation from the rigid body frame to the flexible appendage frame is

$$a = [c]\{b\} \quad (\text{A.4})$$

where $[c]$ is constant for an undriven appendage.

For the undeformed system, the location of the center of mass is defined by

$$\int_{sys} \rho \, dm = 0 \quad (\text{A.5})$$

where ρ is the generic position vector from the center of mass to the differential mass element.

Next, the integral is evaluated,

$$\int_{sys} \rho \, dm = \int_{rigidbody} \rho \, dm + \int_{flexbody} \rho \, dm \quad (\text{A.6})$$

The first integral on the right hand side of the equation is $-(M^* - M)L$ while the second of the integrals is $M(R + r_a)$. Thus,

$$-(M^* - M)L + M(R + r_a) = 0 \quad (\text{A.7})$$

The inertia dyadic of the undeformed system is

$$II^* = II_{RB}^o + II_{Ap-u}^o \quad (\text{A.8})$$

where II_{RB}^o is the inertia dyad of the rigid body and II_{Ap-u}^o is the inertia dyad of the undeformed appendage.

$$II_{RB}^o = II_{RB}^B + (M^* - M)(LLU - LL) \quad (\text{A.9})$$

$$II_{Ap-u}^o = II_{Ap-u}^A + M[(R + r_a)(R + r_a)U - (R + r_a)(R + r_a)] \quad (\text{A.10})$$

The kinetic energy for the system, T_{sys} , consists of terms for the rigid body and for the flexible appendage.

$$T_{sys} = \frac{1}{2} \int_{rb} v \cdot v \, dm + \frac{1}{2} \int_{app} v \cdot v \, dm \quad (\text{A.11})$$

where v is the inertial velocity of a generic mass element. For the rigid body

$$\begin{aligned} T_{RB} &= \frac{1}{2} \int_{rb} v \cdot v \, dm \\ T_{RB} &= \frac{1}{2}(M^* - M)\dot{R}_B \cdot \dot{R}_B + \frac{1}{2}\omega_B \cdot II_{RB}^B \cdot \omega_B \end{aligned} \quad (\text{A.12})$$

Recall

$$\begin{aligned} R_B &= z - L \\ \dot{R}_B &= \dot{z} - \omega_B \times L \\ z &= O - O' \end{aligned} \quad (\text{A.13})$$

Inserting Eqs. A.13 into Eq. A.12, the resulting kinetic energy of the rigid body becomes

$$\begin{aligned} T_{RB} &= \frac{1}{2}(M^* - M)\{\dot{z} - \omega_B \times L\} \cdot \{\dot{z} - \omega_B \times L\} + \frac{1}{2}\omega_B \cdot II_{RB}^B \cdot \omega_B \\ &= \frac{1}{2}(M^* - M)\dot{z} \cdot \dot{z} - (M^* - M)[\dot{z} \cdot (\omega_B \times L)] \\ &\quad + \frac{1}{2}(M^* - M)(\omega_B \times L) \cdot (\omega_B \times L) + \frac{1}{2}\omega_B \cdot II_{RB}^B \cdot \omega_B \end{aligned} \quad (\text{A.14})$$

Using the Parallel Axis Theorem relationships[224]

$$\begin{aligned}
 II_{cm} &= II_B - (M^* - M)(L^2 I - L \cdot L) \\
 II_B &= II_{cm} + (M^* - M)(L^2 I - L \cdot L) \\
 II_{RB}^B &= II_{RB}^o + (M^* - M)(L^2 I - L \cdot L)
 \end{aligned} \tag{A.15}$$

the kinetic energy of the rigid body, with the inertial dyadic referred to the center of mass, is

$$T_{RB} = \frac{1}{2}(M^* - M)\dot{z} \cdot \dot{z} + \frac{1}{2}\omega_B \cdot II_{RB}^o \cdot \omega_B - (M^* - M)[\dot{z} \cdot (\omega_B \times L)] \tag{A.16}$$

The kinetic energy of the appendage is

$$T_{app} = \frac{1}{2} \int_{app} \dot{v} \cdot \dot{v} \, dm = \frac{1}{2} \int_{app} \dot{R}_m \cdot \dot{R}_m \, dm \tag{A.17}$$

where

$$R_m = z + R + r_a + u \tag{A.18}$$

and

$$\dot{R}_m = \dot{z} + \dot{u} + \omega_B \times (R + r_a) \tag{A.19}$$

Now, expand Eq. A.17 and use II_{app}^o , the dyadic of the undeformed appendage about the center of mass.

$$\begin{aligned}
 T_{app} &= \frac{1}{2} \int_{app} \dot{R}_m \cdot \dot{R}_m \, dm \\
 &= \frac{1}{2} \int_{app} [\dot{z} + \dot{u} + \omega_B \times (R + r_a)] \cdot [\dot{z} + \dot{u} + \omega_B \times (R + r_a)] \, dm \\
 &= \frac{1}{2} M \dot{z} \cdot \dot{z} + \dot{z} \cdot \int_{app} \dot{u} \, dm + \dot{z} \cdot \omega_B \times (M(R + r_a)) + \frac{1}{2} \int_{app} \dot{u} \cdot \dot{u} \, dm \\
 &\quad + \frac{1}{2} \int_{app} [\omega_B \times (R + r_a)] \cdot [\omega_B \times (R + r_a)] \, dm \\
 &\quad + \int_{app} \dot{u} \cdot [\omega_B \times (R + r_a)] \, dm
 \end{aligned} \tag{A.20}$$

Consider the following portion of Eq. A.20.

$$\frac{1}{2} \int_{app} [\omega_B \times (R + r_a)] \cdot [\omega_B \times (R + r_a)] \, dm \tag{A.21}$$

Knowing the vector property $\vec{a} \times \vec{b} = -\vec{b} \times \vec{a}$, and the following vector analysis[222]:

$$\begin{aligned} F_1 \cdot (F_2 \times F_3) &= (F_1 \times F_2) \cdot F_3 \\ F_1 \times (F_2 \times F_3) &= (F_1 \cdot F_3)F_2 - (F_1 \cdot F_2)F_3 \end{aligned}$$

Then,

$$\begin{aligned} (a \times b) \cdot (a \times b) &= (a \times b \times a) \cdot b \\ &= [(a \cdot a)b - (a \cdot b)a] \cdot b \\ &= (a \cdot a)(b \cdot b) - (a \cdot b)(a \cdot b) \\ &= a^2b^2 - (a \cdot b)^2 \end{aligned}$$

and Eq. A.21 becomes

$$\frac{1}{2} \int_{app} \omega_B^2 (R + r_a)^2 - (\omega_B \cdot (R + r_a))^2 dm \quad (\text{A.22})$$

$$\frac{1}{2} \omega_B \int_{app} (R + r_a)^2 I - (R + r_a)(R + r_a) dm \omega_B \quad (\text{A.23})$$

The term in the integral is the inertial dyadic of the undeformed appendage about the system mass center, O (II_{Ap-u}^o). The kinetic energy of the undeformed appendage is

$$\begin{aligned} T_{Ap-u} &= \frac{1}{2} M \dot{z} \cdot \dot{z} + \dot{z} \cdot \int_{app} \dot{u} dm + \dot{z} \cdot \omega_B \times (M(R + r_a)) + \frac{1}{2} \int_{app} \dot{u} \cdot \dot{u} dm \\ &+ \int_{app} \dot{u} \cdot [\omega_B \times (R + r_a)] dm + \frac{1}{2} \omega_B \cdot II_{Ap-u}^o \cdot \omega_B \quad (\text{A.24}) \end{aligned}$$

The total system kinetic energy, including the rigid body and the flexible appendage, is

$$\begin{aligned} T_{sys} &= \frac{1}{2} (M^* - M) \dot{z} \cdot \dot{z} + \frac{1}{2} \omega_B \cdot II_{RB}^o \cdot \dot{\omega}_B - (M^* - M) [\dot{z} \cdot (\omega_B \times L)] + \frac{1}{2} M \dot{z} \cdot \dot{z} \\ &+ \dot{z} \cdot \int_{app} \dot{u} dm + \dot{z} \cdot \omega_B \times (M(R + r_a)) + \frac{1}{2} \int_{app} \dot{u} \cdot \dot{u} dm \\ &+ \int_{app} \dot{u} \cdot [\omega_B \times (R + r_a)] dm + \frac{1}{2} \omega_B \cdot II_{Ap-u}^o \cdot \omega_B \quad (\text{A.25}) \end{aligned}$$

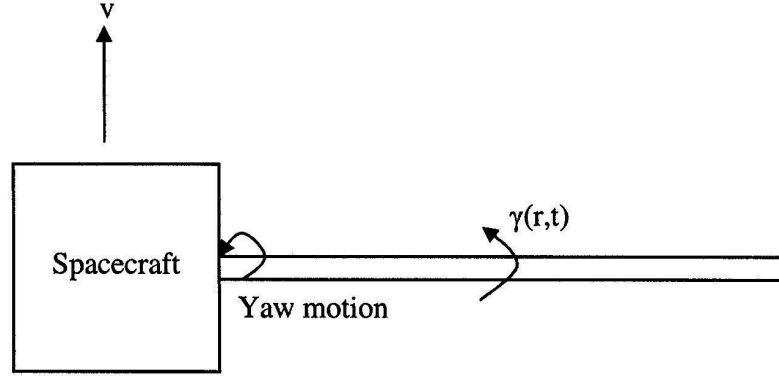


Figure A.2: Illustration of Spacecraft Yaw Producing Torsional Torque

With Eq. A.25, combine II_{RB}^o and II_{Ap-u}^o into II^* , combine the $\dot{z} \cdot \dot{z}$ terms, and the moments about the center of mass relationship from Eq. A.7.

$$\begin{aligned}
 T_{sys} = & \frac{1}{2} M \dot{z} \cdot \dot{z} + \frac{1}{2} \omega_B \cdot II^* \cdot \omega_B + \frac{1}{2} \int_{app} \dot{u} \cdot \dot{u} \, dm + \dot{z} \cdot \int_{app} \dot{u} \, dm \\
 & + \omega_B \cdot R \times \int_{app} \dot{u} \, dm + \omega_B \cdot \int_{app} (r_a \times \dot{u}) \, dm
 \end{aligned} \tag{A.26}$$

Neglecting external conservative torques such as gravity gradient affects, the potential energy of the system is due to the energy stored in the deformation of the appendage. Any elementary text on mechanics of materials calculates the strain energy of a deflected beam as[180]

$$V_{bend} = \frac{1}{2} \int_{app} EI \left(\frac{\partial^2 u}{\partial r^2} \right)^2 dr \tag{A.27}$$

The potential energy is for the case of an Euler-Bernoulli beam which is in deformation without any torsional concerns. The flexible appendage undergoing torsion needs to be included in the equations of motion of the system. This is a concern since yaw control torques will produce torsional moments along the longitudinal axis of the appendage (see Figure A.2). Roll/pitch attitude maneuvers will generate bending torques and are included in Eq. A.26 and Eq. A.27.

Let $\gamma(r, t)$ denote the angular displacement of the appendage. The angle of twist corresponding to a differential element of appendage of length dr is $\left[\frac{\partial \gamma(r, t)}{\partial r} \right] dr$. Assuming

the material properties are uniform in the appendage and the angle of twist is proportional to the torque, the potential energy of the appendage in torsion (whose ends are not supported by torsional springs capable of storing potential energy) is written as

$$V_{torsion} = \frac{1}{2} \int_{app} GJ(r) \left[\frac{\partial \gamma(r, t)}{\partial r} \right]^2 dr \quad (\text{A.28})$$

where $GJ(r)$ is the torsional rigidity and Eq. A.28 has the same structure as the potential energy of a rod in longitudinal vibration. In addition, if $I_{pmi}(r)$ is the mass polar moment of inertia per unit length, then the kinetic energy is simply

$$T_{torsion} = \frac{1}{2} \int_{app} I_{pmi}(r) \left[\frac{\partial \gamma(r, t)}{\partial t} \right]^2 dr \quad (\text{A.29})$$

A.2 Lagrangian Equations of Motion

To determine the system's equations of motion, the Lagrangian is found by subtracting the potential energy components from the kinetic energy terms as follows

$$L = T - V \quad (\text{A.30})$$

Inserting Eqs. A.26-A.29 into Eq. A.30, the system Lagrange becomes

$$\begin{aligned} L &= \frac{1}{2} M^* \dot{z} \cdot \dot{z} + \frac{1}{2} \omega_B \cdot II^* \cdot \omega_B + \frac{1}{2} \int_{app} \dot{u} \cdot \dot{u} \, dm + \dot{z} \cdot \int_{app} \dot{u} \, dm \\ &+ \omega_B \cdot R \times \int_{app} \dot{u} \, dm + \omega_B \cdot \int_{app} r \times \dot{u} \, dm + \frac{1}{2} \int_{app} I_{pmi}(r) \left[\frac{\partial \gamma(r, t)}{\partial t} \right]^2 dr \\ &- \frac{1}{2} \int_{app} EI \left(\frac{\partial^2 u}{\partial r^2} \right)^2 dr - \frac{1}{2} \int_{app} GJ(r) \left[\frac{\partial \gamma(r, t)}{\partial r} \right]^2 dr \end{aligned} \quad (\text{A.31})$$

where, referencing Figure A.3, u is the flexural displacement and r is the coordinate along the appendage length to replace r_a . Also, assume the undeformed appendage is fixed relative to the base, $\omega_B^B = \omega_B^A$, and small angle rotations, $\omega_B \approx \{\dot{\theta}\}$, $II^* \approx I^*$.

The Lagrangian can also be written in matrix form by using the following representations:

$$z = \{i\}^T \{z\}$$

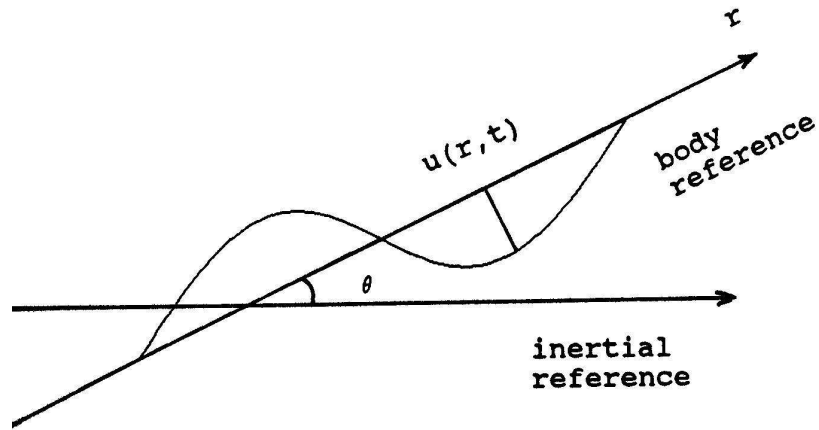


Figure A.3: Displacement of the Flexible Appendage

$$\omega_B = \{b\}^T \{\omega_B\}$$

$$u = \{a\}^T \{u\}$$

$$II^* = \{b\}^T I^* \{b\}$$

$$R = \{b\}^T \{R\}$$

$$r = \{b\}^T \{r\}$$

$$R = \begin{pmatrix} 0 & -R_3 & R_2 \\ R_3 & 0 & -R_1 \\ -R_2 & R_1 & 0 \end{pmatrix}$$

$$\tilde{r} = \begin{pmatrix} 0 & -r_3 & r_2 \\ r_3 & 0 & -r_1 \\ -r_2 & r_1 & 0 \end{pmatrix}$$

$$\tilde{\theta} = \begin{pmatrix} 0 & -\theta_3 & \theta_2 \\ \theta_3 & 0 & -\theta_1 \\ -\theta_2 & \theta_1 & 0 \end{pmatrix}$$

$$[\theta] = \{E - \tilde{\theta}\}$$

$$\begin{aligned}\frac{\partial^2 u}{\partial r^2} &= \{a\}^T \begin{pmatrix} \frac{\partial^2 u_1}{\partial r^2} \\ \frac{\partial^2 u_2}{\partial r^2} \\ \frac{\partial^2 u_3}{\partial r^2} \end{pmatrix} \\ &= \{a\}^T \{u''\}\end{aligned}$$

and the basis transformation relationships

$$\{b\} = [\theta]\{i\}$$

$$\{a\} = [c]\{b\}$$

which yields

$$\begin{aligned}L &= \frac{1}{2}M^*\{\dot{z}\}^T\{\dot{z}\} + \frac{1}{2}\{\dot{\theta}\}^T I^* \{\dot{\theta}\} + \frac{1}{2} \int_{app} \{\dot{u}\}^T \{\dot{u}\} dm + \{\dot{z}\}^T [c] \int_{app} \{\dot{u}\} dm \\ &+ \{\dot{\theta}\}^T [c] R \int_{app} \{\dot{u}\} dm + \{\dot{\theta}\}^T [c] \int_{app} \tilde{r} \{\dot{u}\} dm + \frac{1}{2} \int_{app} I_{pmi} \dot{\gamma}^2 dr \\ &- \frac{1}{2} \int_{app} EI \{u''\}^T \{u''\} dr - \frac{1}{2} \int_{app} GJ(\gamma')^2 dr\end{aligned}\quad (A.32)$$

Now, introduce the distributed coordinates

$$u(r, t) = \sum_{i=1}^n \phi^i(r) \eta^i(t) \quad (A.33)$$

where n is the number of modes used to represent the displacement and

$$[u] = [\phi]\{\eta\} \quad (A.34)$$

where $[\phi]$ is a $3 \times n$ matrix with each column corresponding to a mode shape, the assumed mode shapes are the spatial solutions of the Euler-Bernoulli partial differential equation, and $\{\eta\}$ contains n modal coordinates.

A similar representation is done for the torsional component where

$$\gamma = [\psi]\{\eta\} \quad (A.35)$$

and $[\psi]$ is a $1 \times n$ torsional mode shape matrix using the same modal coordinates, $\{\eta\}$, from Eq. A.34.

Substitute Eq. A.34 and Eq. A.35 into Eq. A.32

$$\begin{aligned}
L &= \frac{1}{2}M^*\{\dot{z}\}^T\{\dot{z}\} + \frac{1}{2}\{\dot{\theta}\}^T I^*\{\dot{\theta}\} + \frac{1}{2}\int_{app} \{[\phi]\{\dot{\eta}\}\}^T\{[\phi]\{\dot{\eta}\}\} dm \\
&+ \{\dot{z}\}^T[c]\int_{app} \{[\phi]\{\dot{\eta}\}\} dm + \{\dot{\theta}\}^T[c]R\int_{app} \{[\phi]\{\dot{\eta}\}\} dm \\
&+ \{\dot{\theta}\}^T[c]\int_{app} \tilde{r}\{[\phi]\{\dot{\eta}\}\} dm + \frac{1}{2}\int_{app} I_{pmi}\{[\psi]\{\dot{\eta}\}\}^T\{[\psi]\{\dot{\eta}\}\} dr \\
&- \frac{1}{2}\int_{app} EI\{[\phi']\{\eta\}\}^T\{[\phi']\{\eta\}\} dr \\
&- \frac{1}{2}\int_{app} GJ\{[\psi']\{\eta\}\}^T\{[\psi']\{\eta\}\} dr
\end{aligned} \tag{A.36}$$

or

$$\begin{aligned}
L &= \frac{1}{2}M^*\{\dot{z}\}^T\{\dot{z}\} + \frac{1}{2}\{\dot{\theta}\}^T I^*\{\dot{\theta}\} + \frac{1}{2}\{\dot{\eta}\}^T \int_{app} [\phi]^T[\phi] dm\{\dot{\eta}\} \\
&+ \{\dot{z}\}^T[c]\int_{app} [\phi] dm\{\dot{\eta}\} + \{\dot{\theta}\}^T[c]R\int_{app} [\phi] dm\{\dot{\eta}\} \\
&+ \{\dot{\theta}\}^T[c]\int_{app} \tilde{r}[\phi] dm\{\dot{\eta}\} + \frac{1}{2}\{\dot{\eta}\}^T \int_{app} I_{pmi}[\psi]^T[\psi] dr\{\dot{\eta}\} \\
&- \frac{1}{2}\{\eta\}^T \int_{app} EI[\phi']^T[\phi'] dr\{\eta\} \\
&- \frac{1}{2}\{\eta\}^T \int_{app} GJ[\psi']^T[\psi'] dr\{\eta\}
\end{aligned} \tag{A.37}$$

Let

$$X_1 = \int_{app} [\phi] dm \quad (3 \times n) \tag{A.38}$$

$$X_2 = \int_{app} [\phi]^T[\phi] dm \quad (n \times n) \tag{A.39}$$

$$X_3 = \int_{app} r[\phi] dm \quad (3 \times n) \tag{A.40}$$

$$X_4 = \int_{app} EI[\phi']^T[\phi'] dr \quad (n \times n) \tag{A.41}$$

$$X_5 = \int_{app} I_{pmi}[\psi]^T[\psi] dr \quad (\text{scalar}) \tag{A.42}$$

$$X_6 = \int_{app} GJ[\psi']^T[\psi'] dr \quad (\text{scalar}) \tag{A.43}$$

The Lagrangian can now be expressed as

$$\begin{aligned}
L &= \frac{1}{2}M^*\{\dot{z}\}^T\{\dot{z}\} + \frac{1}{2}\{\dot{\theta}\}^T I^*\{\dot{\theta}\} + \frac{1}{2}\{\dot{\eta}\}^T X_2\{\dot{\eta}\} + \{\dot{z}\}^T[c]X_1\{\dot{\eta}\} \\
&+ \{\dot{\theta}\}^T[c](RX_1 + X_3)\{\dot{\eta}\} + \frac{1}{2}\{\dot{\eta}\}^T X_5\{\dot{\eta}\}
\end{aligned}$$

$$- \frac{1}{2}\{\eta\}^T X_4\{\eta\} - \frac{1}{2}\{\eta\}^T X_6\{\eta\} \quad (\text{A.44})$$

The Lagrangian contains six coordinates which describe the translation and rotation of the undeformed system (rigid body motion) and n modal coordinates which describe the twist and displacement from rest of the flexible appendage relative to the rigid base. The equations of motion take the form[79]

$$\frac{d}{dt}\left(\frac{\partial L}{\partial \dot{q}_i}\right) - \frac{\partial L}{\partial q_i} = Q_i \quad (\text{A.45})$$

where Q_i are the generalized forces and the generalized variables are:

translation: z (3 position coordinates)

rotation: θ (3 rotational coordinates)

vibration: η (n modal coordinates)

The partial derivatives of the Lagrangian are:

$$\frac{\partial L}{\partial z} = 0 \quad (\text{A.46})$$

$$\frac{\partial L}{\partial \dot{z}} = M^*\{\dot{z}\} + [c]X_1\{\dot{\eta}\} \quad (\text{A.47})$$

$$\frac{\partial L}{\partial \theta} = 0 \quad (\text{A.48})$$

$$\frac{\partial L}{\partial \dot{\theta}} = I^*\{\dot{\theta}\} + [c](RX_1 + X_3)\{\dot{\eta}\} \quad (\text{A.49})$$

$$\frac{\partial L}{\partial \eta} = -X_4\{\eta\} - X_6\{\eta\} \quad (\text{A.50})$$

$$\frac{\partial L}{\partial \dot{\eta}} = X_2\{\dot{\eta}\} + X_1^T[c]^T\{\dot{z}\} + (RX_1 + X_3)^T[c]^T\{\dot{\theta}\} + X_5\{\dot{\eta}\} \quad (\text{A.51})$$

The time derivatives of the generalized momenta are:

$$\frac{d}{dt}\left(\frac{\partial L}{\partial \dot{z}}\right) = M^*\{\ddot{z}\} + [c]X_1\{\ddot{\eta}\} \quad (\text{A.52})$$

$$\frac{d}{dt}\left(\frac{\partial L}{\partial \dot{\theta}}\right) = I^*\{\ddot{\theta}\} + [c](RX_1 + X_3)\{\ddot{\eta}\} \quad (\text{A.53})$$

$$\frac{d}{dt}\left(\frac{\partial L}{\partial \dot{\eta}}\right) = X_2\{\ddot{\eta}\} + X_1^T[c]^T\{\ddot{z}\} + (RX_1 + X_3)^T[c]^T\{\ddot{\theta}\} + X_5\{\ddot{\eta}\} \quad (\text{A.54})$$

The system equations of motion are written as

$$\text{Translation: } M^*\{\ddot{z}\} + [c]X_1\{\ddot{\eta}\} = \{Q_{trans}\} \quad (\text{A.55})$$

$$\text{Rotation: } I^*\{\ddot{\theta}\} + [c](RX_1 + X_3)\{\ddot{\eta}\} = \{Q_{rot}\} \quad (\text{A.56})$$

$$\text{Vibration: } X_2\{\ddot{\eta}\} + X_5\{\ddot{\eta}\} + X_1^T[c]^T\{\ddot{z}\} + (RX_1 + X_3)^T[c]^T\{\ddot{\theta}\} + X_4\{\eta\} + X_6\{\eta\} = \{Q_{damp}\} \quad (\text{A.57})$$

where $\{Q_{trans}\}$ are the generalized translational forces acting on the system, $\{Q_{rot}\}$ are the generalized rotational forces, and $\{Q_{damp}\}$ are the generalized damping forces within the flexible appendage. An example of a translational system force would be thrusters providing station keeping forces while attitude control torques, such as those provided by off-axial thrusters or reaction wheels, are contained within the rotational forces category.

The generalized damping forces within the flexible appendage will take the form of $\{Q_{damp}\} = -c\{\dot{\eta}\}$, where the damping coefficient, c , is not to be confused with the transformation matrix, $[c]$, going from the body fixed frame to the flexible appendage frame. In fact, if the flexible appendage is not off-nominal, meaning the principal axes of the appendage line up with those of the rigid body, then the transformation matrix, $[c]$, can be assumed to equal the identity matrix and may be eliminated from the equations of motion.

Another point to consider is the dimensions of X_2 , X_4 , X_5 , and X_6 . Looking at Eq. A.57, it would seem intuitive to combine these values together. However, X_2 and X_4 are $(n \times n)$ matrices while X_5 and X_6 are scalars. The scalar values can be multiplied by the identity matrix to put them in a form which will allow the collection of similar terms in Eq. A.57.

Assuming station keeping is not a key factor in the attitude control conceptual operations of the spacecraft, and applying the above relationships, the equations of motion are rewritten as follows:

$$M^*\{\ddot{z}\} + X_1\{\ddot{\eta}\} = 0 \quad (\text{A.58})$$

$$I^*\{\ddot{\theta}\} + (RX_1 + X_3)\{\ddot{\eta}\} = \{Q_{rot}\} \quad (\text{A.59})$$

$$(X_2 + X_5)\{\ddot{\eta}\} + c\{\dot{\eta}\} + (X_4 + X_6)\{\eta\} = -X_1^T\{\ddot{z}\} - (RX_1 + X_3)^T\{\ddot{\theta}\} \quad (\text{A.60})$$

Now, Eq. A.58 is rewritten as

$$\{\ddot{z}\} = -\frac{1}{M^*}X_1\{\ddot{\eta}\} \quad (\text{A.61})$$

and is substituted into Eq. A.60 to eliminate translational effects from the vibrational equation. This results in a coupled set of rotation-vibration equations.

$$\begin{aligned} I^*\{\ddot{\theta}\} + (RX_1 + X_3)\{\ddot{\eta}\} &= \{Q_{rot}\} \\ (X_2 + X_5 - \frac{1}{M^*}X_1^T X_1)\{\ddot{\eta}\} + c\{\dot{\eta}\} + (X_4 + X_6)\{\eta\} &= -(RX_1 + X_3)^T\{\ddot{\theta}\} \end{aligned} \quad (\text{A.62})$$

The theoretical derivation can be furthered by noticing the rotation/vibration coupling terms in each of the two equations are the transpose of each other. Let

$$P = (RX_1 + X_3) \quad (\text{A.63})$$

where P has dimensions $(3 \times n)$.

Inserting Eq. A.63 into Eq. A.59 and solving for $\ddot{\theta}$ yields

$$\ddot{\theta} = (I^*)^{-1}\{Q_{rot}\} - (I^*)^{-1}P\{\ddot{\eta}\} \quad (\text{A.64})$$

Now, insert Eq. A.64 into the right hand side of Eq. A.62.

$$\begin{aligned} &= -P^T\{\ddot{\theta}\} \\ &= -P^T[(I^*)^{-1}\{Q_{rot}\} - (I^*)^{-1}P\{\ddot{\eta}\}] \\ &= -P^T(I^*)^{-1}\{Q_{rot}\} + P^T(I^*)^{-1}P\{\ddot{\eta}\} \end{aligned} \quad (\text{A.65})$$

to finally arrive at the equation of motion describing how the flexible appendage responds to attitude control torques.

$$(X_2 + X_5 - \frac{1}{M^*}X_1^T X_1 - P^T(I^*)^{-1}P)\{\ddot{\eta}\} + C\{\dot{\eta}\} + (X_4 + X_6)\{\eta\} = -P^T(I^*)^{-1}\{Q_{rot}\} \quad (\text{A.66})$$

where I^* is the nonsingular system inertia matrix and C is the $(n \times n)$ damping matrix. Note, the equation of motion can be represented as the classical dynamic model

$$M\{\ddot{\eta}\} + C\{\dot{\eta}\} + K\{\eta\} = F \quad (\text{A.67})$$

if

$$\begin{aligned} M &= (X_2 + X_5 - \frac{1}{M^*} X_1^T X_1 - P^T (I^*)^{-1} P) \\ K &= (X_4 + X_6) \\ F &= -P^T (I^*)^{-1} \{Q_{rot}\} \end{aligned} \quad (\text{A.68})$$

Appendix B

Gravity Gradient Stabilization

The center of gravity is often times not in the same location as the center of mass for a large object orbiting about a planet. The differing locations will result in a torque applied to the object as a result of differing gravitational strength. A simple solution to overcome this applied torque in a gravity gradient field is to attach a cable to the satellite. A mass is attached to the end of the cable pointing either toward or away from the earth. The cable is slowly let out until a stable configuration is achieved. The concept of gravity gradient control is discussed in several sources[80], [90], [159], [176], [238], and[240].

B.1 Gravitational Field

Newton's Law of Universal Gravitation states:

The force of gravity between two bodies is directly proportional to the product of their two masses and inversely proportional to the square of the distance between them[186].

Thus, the gravitational potential energy (V) is found with

$$V = -\frac{GMm}{R} \quad (\text{B.1})$$

where $G = 6.6726 \times 10^{-11} \text{ m}^3/\text{kgsec}^2$, M is the mass of the primary body, m is the mass of the orbiting body, and R is the distance separating the two masses. If the satellite is

in an Earth orbit, then $M = 5.9737 \times 10^{24} \text{ kg}$ and the gravitational parameter for Earth becomes $\mu = GM = 3.9860 \times 10^{14} \text{ m}^3/\text{sec}^2$. Substituting the gravitational parameter of Earth into Eq. B.1 yields

$$V = -\frac{\mu m}{R} \quad (\text{B.2})$$

The gravitational force field is the gradient of the gravitational potential and the gravitational acceleration acting on mass m is defined as:

$$\vec{a}_g = \frac{\nabla_\alpha V}{m} \quad (\text{B.3})$$

where

$$\nabla_\alpha = \hat{b}_1 \frac{\partial}{\partial b_1} + \hat{b}_2 \frac{\partial}{\partial b_2} + \hat{b}_3 \frac{\partial}{\partial b_3} \quad (\text{B.4})$$

in terms of the body fixed coordinates shown in Figure B.1.

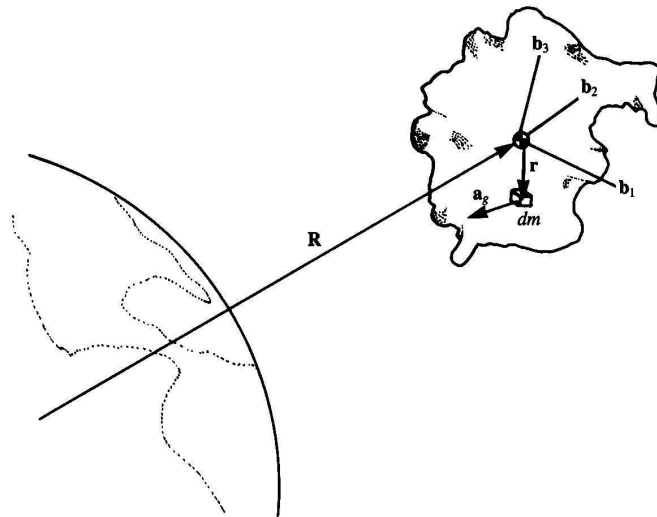


Figure B.1: Gravity Gradient Torques on a Near-Earth Satellite[240]

In a cartesian coordinate frame, the components of the gravitational field are

$$\Gamma_{\alpha\beta} = \nabla_\alpha \nabla_\beta \frac{V}{m}$$

$$\Gamma_{\alpha\beta} = \frac{1}{m} \begin{pmatrix} \frac{\partial^2 V}{\partial e_1^2} & \frac{\partial^2 V}{\partial e_1 \partial e_2} & \frac{\partial^2 V}{\partial e_1 \partial e_3} \\ \frac{\partial^2 V}{\partial e_1 \partial e_2} & \frac{\partial^2 V}{\partial e_2^2} & \frac{\partial^2 V}{\partial e_2 \partial e_3} \\ \frac{\partial^2 V}{\partial e_1 \partial e_3} & \frac{\partial^2 V}{\partial e_2 \partial e_3} & \frac{\partial^2 V}{\partial e_3^2} \end{pmatrix} \quad (\text{B.5})$$

$\Gamma_{\alpha\beta}$ is the gravitational acceleration gradient causing an acceleration in the α direction on an object displaced in the β direction ($\alpha, \beta = b_1, b_2, b_3$). The acceleration in the b_1 direction is

$$a_1 = \Gamma_{11}e_1 + \Gamma_{12}e_2 + \Gamma_{13}e_3 \quad (\text{B.6})$$

If the body fixed reference frame is located at the center of mass of the satellite while a vector, \vec{R}_o , points from the origin of the primary body to the center of gravity of the satellite, the gravitational acceleration in an inertial frame can be expressed as follows:

$$\begin{aligned} \vec{a}_g &= -GM \frac{\vec{R}_0}{R_0^3} \\ &= -\mu \frac{(\vec{R} + \vec{r})}{R_0^3} \\ &= -\mu \frac{(\vec{R} + \vec{r})}{[(\vec{R} + \vec{r}) \cdot (\vec{R} + \vec{r})]^{\frac{3}{2}}} \\ &= -\mu \frac{(\vec{R} + \vec{r})}{R^3} \left[1 + \left(\frac{r}{R}\right)^2 + \frac{2\vec{R} \cdot \vec{r}}{R^2} \right]^{-\frac{3}{2}} \\ &= -\frac{\mu}{R^3} [\vec{R} + \vec{r} - 3\frac{\vec{R} \cdot \vec{r}}{R^2} \vec{R}] + \text{higher order terms} \end{aligned} \quad (\text{B.7})$$

Therefore, if

$$\vec{R} = R\hat{b}_3 \quad (\text{B.8})$$

and

$$\vec{r} = r_1\hat{b}_1 + r_2\hat{b}_2 + r_3\hat{b}_3 \quad (\text{B.9})$$

then

$$\vec{a}_g \approx -\frac{\mu}{R^3} [r_1\hat{b}_1 + r_2\hat{b}_2 + (R - 2r_3)\hat{b}_3] \quad (\text{B.10})$$

Substituting Eq. B.10 into Eq. B.3 results in the following:

$$\Gamma_{11} = -\frac{\mu}{R^3} \quad (\text{B.11})$$

$$\Gamma_{22} = -\frac{\mu}{R^3} \quad (\text{B.12})$$

$$\Gamma_{33} = \frac{2\mu}{R^3} \quad (\text{B.13})$$

and putting the gradient of the gravitational field into matrix form yields

$$\Gamma = \frac{GM}{R^3} \begin{pmatrix} -1 & 0 & 0 \\ 0 & -1 & 0 \\ 0 & 0 & 2 \end{pmatrix} \quad (\text{B.14})$$

B.2 Inertial Gradient Field

If the reference frame is rotating with an angular velocity $\vec{\omega}$, then an inertial acceleration field is developed. The gradients from the inertial field are added to the gravitational gradients to obtain the total gradient.

The general expression for the apparent acceleration of a point in a rotating frame is

$$\ddot{\vec{r}}' = \vec{a} - [\vec{a}_0 + \vec{\omega}x(\vec{\omega}x\vec{r}) + \dot{\vec{\omega}}x\vec{r} + 2\vec{\omega}x\dot{\vec{r}}'] \quad (\text{B.15})$$

Only terms involving \vec{r} have gradients which can be added to the gravitational gradients in Eq. B.14. Let

$$\begin{aligned} \vec{A} &= -[\vec{\omega}x(\vec{\omega}x\vec{r}) + \dot{\vec{\omega}}x\vec{r}] \\ &= \omega^2\vec{r} - \vec{\omega}(\vec{\omega} \cdot \vec{r}) + \vec{r}x\dot{\vec{\omega}} \\ &= A_1\hat{b}_1 + A_2\hat{b}_2 + A_3\hat{b}_3 \end{aligned} \quad (\text{B.16})$$

where

$$A_1 = r_2\dot{\omega}_3 - r_3\dot{\omega}_2 + (\omega_2^2 + \omega_3^2)r_1 - \omega_1\omega_2r_2 - \omega_1\omega_3r_3 \quad (\text{B.17})$$

$$A_2 = r_3\dot{\omega}_1 - r_1\dot{\omega}_3 + (\omega_3^2 + \omega_1^2)r_2 - \omega_2\omega_3r_3 - \omega_2\omega_1r_1 \quad (\text{B.18})$$

$$A_3 = r_1\dot{\omega}_2 - r_2\dot{\omega}_1 + (\omega_1^2 + \omega_2^2)r_3 - \omega_3\omega_1r_1 - \omega_3\omega_2r_2 \quad (\text{B.19})$$

and

$$\vec{\omega} = \omega_1\hat{b}_1 + \omega_2\hat{b}_2 + \omega_3\hat{b}_3 \quad (\text{B.20})$$

After taking the partial derivatives of \vec{A} and substituting them into Eq. B.14, the gradient matrix becomes

$$G_{\alpha\beta} = \begin{pmatrix} (\Gamma_{11} + \omega_2^2 + \omega_3^2) & (\dot{\omega}_3 - \omega_1\omega_2) & -(\dot{\omega}_2 + \omega_1\omega_3) \\ -(\dot{\omega}_3 + \omega_1\omega_2) & (\Gamma_{22} + \omega_1^2 + \omega_3^2) & (\dot{\omega}_1 - \omega_2\omega_3) \\ (\dot{\omega}_2 - \omega_1\omega_3) & -(\dot{\omega}_1 + \omega_2\omega_3) & (\Gamma_{33} + \omega_1^2 + \omega_2^2) \end{pmatrix} \quad (\text{B.21})$$

If a satellite is orbiting the Earth on a circular path, then its angular velocity is

$$\omega_o^2 = \frac{\mu}{R^3} \quad (\text{B.22})$$

If the body reference frame is orientated such that \hat{b}_1 is aligned in the orbit normal direction, then $\omega_1 = \omega_o$ and $\omega_2 = \omega_3 = 0$. Inserting these angular velocity components into Eq. B.21, and recalling Eq. B.14, the gradient field for a circular orbit becomes

$$G_{\alpha\beta} = \omega_o^2 \begin{pmatrix} -1 & 0 & 0 \\ 0 & 0 & 0 \\ 0 & 0 & 3 \end{pmatrix} \quad (\text{B.23})$$

The above equation shows that for a satellite with a flexible boom deployed, it will experience a compressive load in the orbit normal direction while in tension along the local vertical direction. Thus, a deployed boom will produce a stable configuration either when the boom is zenith or nadir pointing.

B.3 Gravity Gradient Torque

A gravitational gradient torque acting on an orbiting body is expressed as

$$\vec{T}^{(g)} = \int (\vec{r}x\vec{a}_g)dm \quad (\text{B.24})$$

Inserting Eq. B.7 into Eq. B.24 yields

$$\vec{T}^{(g)} \approx \frac{3\mu}{R^3} \int (\vec{r}x\frac{\vec{R} \cdot \vec{r}}{R^2}\vec{R})dm \quad (\text{B.25})$$

Letting $\vec{R} = R\hat{E}_1$, where \hat{E}_1 is the unit vector pointing in the radial direction from the primary body, Eq. B.25 is integrated as follows:

$$\begin{aligned}
\vec{T}^{(g)} &= \frac{3\mu}{R^3} \int \frac{(\vec{R} \cdot \vec{r})\vec{r}x\vec{R}}{R^2} dm \\
&= \frac{3\mu}{R^3} \hat{E}_1 \cdot \int \vec{r}\vec{r} dm x \hat{E}_1 \\
&= \frac{3\mu}{R^3} \hat{E}_1 x \int (\bar{E}r^2 - \vec{r}\vec{r}) dm \cdot \hat{E}_1 \\
&= \frac{3\mu}{R^3} \hat{E}_1 x \bar{I} \cdot \hat{E}_1
\end{aligned} \tag{B.26}$$

where $\bar{E} = \hat{E}_1\hat{E}_1 + \hat{E}_2\hat{E}_2 + \hat{E}_3\hat{E}_3$ is a unit dyadic and the inertia dyadic about the body's center of mass is

$$\bar{I} = \int (\bar{E}r^2 - \vec{r}\vec{r}) dm \tag{B.27}$$

The gravity gradient with respect to the body reference frame b_α ($\alpha = 1, 2, 3$) becomes

$$\begin{aligned}
\vec{T}^{(g)} &= K \hat{E}_1 x \bar{I} \cdot \hat{E}_1 \\
&= K a_{\alpha 1} \hat{b}_\alpha x I_{\alpha\beta} \hat{b}_\alpha \hat{b}_\beta \cdot a_{\alpha 1} \hat{b}_\alpha
\end{aligned} \tag{B.28}$$

where

$$\begin{aligned}
\hat{E}_1 &= a_{\alpha 1} \hat{b}_\alpha = a_{11} \hat{b}_1 + a_{21} \hat{b}_2 + a_{31} \hat{b}_3 \\
\bar{I} &= I_{\alpha\beta} \hat{b}_\alpha \hat{b}_\beta (\alpha, \beta = 1, 2, 3) \\
K &= \frac{3\mu}{R^3}
\end{aligned}$$

and $a_{\alpha 1}$ are the direction cosines between the \hat{E}_1 and \hat{b}_α unit vectors.

The body components of torque are found when the scalar form of Eq. B.28 is written as

$$\begin{aligned}
T_\lambda^{(g)} &= \vec{T}^{(g)} \cdot \hat{b}_\lambda (\lambda = 1, 2, 3) \\
&= K a_{\alpha 1} a_{\beta 1} I_{\lambda\beta} \varepsilon_{\alpha\gamma\lambda}
\end{aligned} \tag{B.29}$$

where the three dimensional permutation tensor is

$$\varepsilon_{\alpha\gamma\lambda} = (\hat{b}_\alpha \times \hat{b}_\gamma) \cdot \hat{b}_\lambda \quad (\alpha, \beta, \gamma, \lambda = 1, 2, 3) \quad (\text{B.30})$$

For the principal body axes $I_{\gamma\beta} = 0$ for $\gamma \neq \beta$. The torque components become

$$\begin{aligned} T_1^{(g)} &= K(I_{33} - I_{22})a_{21}a_{31} \\ T_2^{(g)} &= K(I_{11} - I_{33})a_{11}a_{31} \\ T_3^{(g)} &= K(I_{22} - I_{11})a_{11}a_{21} \end{aligned} \quad (\text{B.31})$$

where the $a_{\alpha\beta}$ terms are still the direction cosines (i.e. $\hat{b}_\alpha = a_{\alpha\beta}\hat{E}_\beta$).

B.4 Equations of Motion

Euler's equation of motion for a satellite in a circular orbit with orbital angular velocity, ω_s , is

$$\dot{\vec{h}} + \vec{\omega}_s \times \vec{h} = \vec{T}^{(g)} \quad (\text{B.32})$$

where

$$\begin{aligned} \vec{h} &= \omega_1 I_1 \hat{b}_1 + \omega_2 I_2 \hat{b}_2 + \omega_3 I_3 \hat{b}_3 \\ \vec{T}^{(g)} &= T_1^{(g)} \hat{b}_1 + T_2^{(g)} \hat{b}_2 + T_3^{(g)} \hat{b}_3 \end{aligned}$$

Three sequential rotations θ_1 about the \hat{b}_1 axis, θ_2 about the \hat{b}_2 axis, and θ_3 about the \hat{b}_3 axis are used to describe the orientation of the satellite's principal axes with respect to the orbiting reference frame. The body reference frame is expressed in terms of the fixed reference frame as follows:

$$\begin{pmatrix} \hat{b}_1 \\ \hat{b}_2 \\ \hat{b}_3 \end{pmatrix} = R(\theta_3)R(\theta_2)R(\theta_1) \begin{pmatrix} \hat{E}_1 \\ \hat{E}_2 \\ \hat{E}_3 \end{pmatrix} \quad (\text{B.33})$$

where

$$R(\theta_1) = \begin{pmatrix} 1 & 0 & 0 \\ 0 & c\theta_1 & s\theta_1 \\ 0 & -s\theta_1 & c\theta_1 \end{pmatrix} \quad (\text{B.34})$$

$$R(\theta_2) = \begin{pmatrix} c\theta_2 & 0 & -s\theta_2 \\ 0 & 1 & 0 \\ s\theta_2 & 0 & c\theta_2 \end{pmatrix} \quad (\text{B.35})$$

$$R(\theta_3) = \begin{pmatrix} c\theta_3 & s\theta_3 & 0 \\ -s\theta_3 & c\theta_3 & 0 \\ 0 & 0 & 1 \end{pmatrix} \quad (\text{B.36})$$

and

$$\begin{aligned} R_{123} &= R(\theta_3)R(\theta_2)R(\theta_1) \\ &= \begin{pmatrix} c\theta_2 c\theta_3 & c\theta_3 s\theta_1 s\theta_2 + c\theta_1 s\theta_3 & -c\theta_1 c\theta_3 s\theta_2 + s\theta_1 s\theta_3 \\ -c\theta_2 s\theta_3 & -s\theta_1 s\theta_2 s\theta_3 + c\theta_1 c\theta_3 & c\theta_1 s\theta_2 s\theta_3 + s\theta_1 c\theta_3 \\ s\theta_2 & -c\theta_2 s\theta_1 & c\theta_1 c\theta_2 \end{pmatrix} \end{aligned} \quad (\text{B.37})$$

The expanded form of the body components of the satellite angular velocity, $\vec{\omega}_s$,

is

$$\begin{aligned} \omega_1 &= \dot{\theta}_1 + \omega_0(c\theta_3 s\theta_1 s\theta_2 + c\theta_1 s\theta_3) \\ \omega_2 &= \dot{\theta}_2 + \omega_0(c\theta_1 c\theta_3 - s\theta_1 s\theta_2 s\theta_3) \\ \omega_3 &= \dot{\theta}_3 + \omega_0(-s\theta_1 c\theta_2) \end{aligned} \quad (\text{B.38})$$

with $\omega_0 = \frac{\mu}{R^3}$. Linearizing yields

$$\begin{aligned} \omega_1 &= \dot{\theta}_1 + \omega_0 \theta_3 \\ \omega_2 &= \dot{\theta}_2 + \omega_0 \\ \omega_3 &= \dot{\theta}_3 - \omega_0 \theta_1 \end{aligned} \quad (\text{B.39})$$

The component equations in scalar form are

$$\begin{aligned}
T_1^{(g)} &= I_1\dot{\omega}_1 + \omega_2\omega_3(I_3 - I_2) \\
T_2^{(g)} &= I_2\dot{\omega}_2 + \omega_1\omega_3(I_1 - I_3) \\
T_3^{(g)} &= I_3\dot{\omega}_3 + \omega_1\omega_2(I_2 - I_1)
\end{aligned} \tag{B.40}$$

Taking the derivative of Eq. B.39 and substituting into Eq. B.40 produces

$$\begin{aligned}
T_1^{(g)} &= I_1(\ddot{\theta}_1 + \omega_0\dot{\theta}_3) + (\dot{\theta}_2 + \omega_0)(\dot{\theta}_3 - \omega_0\theta_1)(I_3 - I_2) \\
T_2^{(g)} &= I_2\ddot{\theta}_2 + (\dot{\theta}_1 + \omega_0\theta_3)(\dot{\theta}_3 - \omega_0\theta_1)(I_1 - I_3) \\
T_3^{(g)} &= I_3(\ddot{\theta}_3 - \omega_0\dot{\theta}_1) + (\dot{\theta}_1 + \omega_0\theta_3)(\dot{\theta}_2 + \omega_0)(I_2 - I_1)
\end{aligned} \tag{B.41}$$

Recall the body components of the gravity gradient torque, $T_1^{(g)}$, $T_2^{(g)}$, and $T_3^{(g)}$, shown in Eq. B.31. Using small angle approximations, the torque components are now expressed as

$$\begin{pmatrix} T_1^{(g)} \\ T_2^{(g)} \\ T_3^{(g)} \end{pmatrix} \approx 3\omega_0^2 \begin{pmatrix} 0 \\ (I_1 - I_3)\theta_2 \\ (I_1 - I_2)\theta_3 \end{pmatrix} \tag{B.42}$$

Inserting these torques into Eqs. B.41, the linearized equations of motion for small angular deviations become

$$0 = I_1(\ddot{\theta}_1 + \omega_0\dot{\theta}_3) + (I_2 - I_3)(\omega_0^2\theta_1 - \omega_0\dot{\theta}_3) \tag{B.43}$$

$$0 = I_2\ddot{\theta}_2 + 3\omega_0^2(I_3 - I_1)\theta_2 \tag{B.44}$$

$$0 = I_3(\ddot{\theta}_3 - \omega_0\dot{\theta}_1) + (I_2 - I_1)(4\omega_0^2\theta_3 + \omega_0\dot{\theta}_1) \tag{B.45}$$

In addition, the gravity gradient restoring torques resulting from small angular deviations are obtained by neglecting the small $\dot{\theta}$ coupling terms.

$$\begin{aligned}
T_1 &= -\omega_0^2(I_2 - I_3)\theta_1 \\
T_2 &= -3\omega_0^2(I_3 - I_1)\theta_2 \\
T_3 &= -4\omega_0^2(I_2 - I_1)\theta_3
\end{aligned} \tag{B.46}$$

note, the restoring torques vanish for a symmetrical satellite.

B.5 Stability Considerations

The derivations provided in the previous section were for a yaw (θ_1), pitch (θ_2), roll (θ_3) configuration. However, FalconSAT-3 uses a roll (θ_1), pitch (θ_2), yaw (θ_3) convention. To avoid confusion between research results presented in this document and those found by the FalconSAT-3 design teams, Eqs. B.43-B.45, the linearized equations of motion of a rigid body in a circular orbit (roll, pitch, and yaw, respectively) are as follows:

$$I_1(\ddot{\theta}_1 - \omega_0\dot{\theta}_3) + (I_2 - I_1)(4\omega_0^2\theta_1 + \omega_0\dot{\theta}_3) = 0 \quad (\text{B.47})$$

$$I_2\ddot{\theta}_2 + 3\omega_0^2(I_1 - I_3)\theta_2 = 0 \quad (\text{B.48})$$

$$I_3(\ddot{\theta}_3 + \omega_0\dot{\theta}_1) + (I_2 - I_1)(\omega_0^2\theta_3 - \omega_0\dot{\theta}_1) = 0 \quad (\text{B.49})$$

Because the pitch-axis equation, Eq. B.48, is decoupled from the roll/yaw equations, Eq. B.47 and Eq. B.49, (i.e. there are no θ_1 or θ_3 terms) consider the characteristic equation of the pitch axis given by

$$s^2 + 3\omega_0^2\frac{I_1 - I_3}{I_2} = 0 \quad (\text{B.50})$$

If $I_1 > I_3$, then the characteristic roots are pure imaginary numbers and the pitch equation is a simple harmonic oscillator. If $I_1 < I_3$, then one of the characteristic roots is a positive real number and the pitch equation is unstable. For an unstable configuration, the satellite will swing away from the equilibrium configuration when disturbed. Therefore, it is required that $I_1 > I_3$ for pitch stability.

For roll/yaw stability analysis, Eq. B.47 and Eq. B.49 are rewritten as

$$\begin{aligned} \ddot{\theta}_1 + (k_1 - 1)\omega_0\dot{\theta}_3 + 4\omega_0^2k_1\theta_1 &= 0 \\ \ddot{\theta}_3 + (1 - k_3)\omega_0\dot{\theta}_1 + \omega_0^2k_3\theta_3 &= 0 \end{aligned} \quad (\text{B.51})$$

where

$$\begin{aligned} k_1 &= \frac{I_2 - I_3}{I_1} \\ k_2 &= \frac{I_2 - I_1}{I_3} \end{aligned}$$

Eqs. B.51 can be combined into one coupled roll/yaw system equation as

$$\begin{pmatrix} 1 & 0 \\ 0 & 1 \end{pmatrix} \begin{pmatrix} \ddot{\theta}_1 \\ \ddot{\theta}_3 \end{pmatrix} + \begin{pmatrix} 0 & \omega_0(k_1 - 1) \\ \omega_0(1 - k_3) & 0 \end{pmatrix} \begin{pmatrix} \dot{\theta}_1 \\ \dot{\theta}_3 \end{pmatrix} + \begin{pmatrix} 4\omega_0^2 k_1 & 0 \\ 0 & \omega_0^2 k_3 \end{pmatrix} \begin{pmatrix} \theta_1 \\ \theta_3 \end{pmatrix} = \begin{pmatrix} 0 \\ 0 \end{pmatrix} \quad (\text{B.52})$$

The characteristic equation of Eq. B.52 becomes

$$\begin{vmatrix} s^2 + 4\omega_0^2 k_1 & s\omega_0(k_1 - 1) \\ s\omega_0(1 - k_3) & s^2 + \omega_0^2 k_3 \end{vmatrix} = 0 \quad (\text{B.53})$$

or

$$s^4 + (1 + 3k_1 + k_1 k_3)\omega_0^2 s^2 + 4k_1 k_3 \omega_0^4 = 0 \quad (\text{B.54})$$

The roots of the coupled roll/yaw system characteristic equation become pure imaginary numbers if and only if

$$\begin{aligned} k_1 k_3 &> 0 \\ 1 + 3k_1 + k_1 k_3 &> 0 \\ (1 + 3k_1 + k_1 k_3)^2 - 16k_1 k_3 &> 0 \end{aligned} \quad (\text{B.55})$$

The requirements in Eqs. B.55, combined with the pitch stability requirement of $I_1 > I_3$, govern the complete stability of the gravity gradient satellite equilibria. This stability result is illustrated using a stability diagram in the (k_1, k_3) plane as shown in Figure B.2.

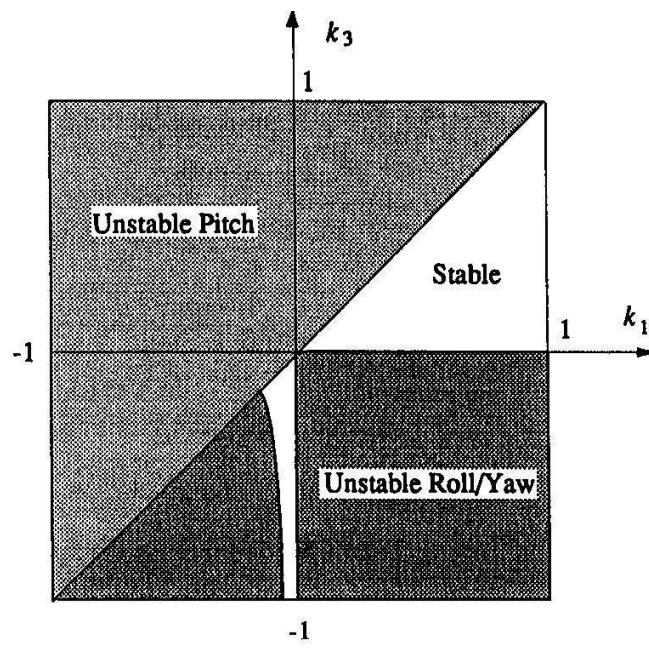


Figure B.2: Gravity Gradient Spacecraft Stability Regions

Appendix C

Rotational Dynamics

C.1 Rotational Kinematics

When studying the equations of motion of an object one must understand both kinetics and kinematics. Kinetics is the study of the forces acting on a body while kinematics describes the motion of that body. This section will concern itself with the theory of rotational kinematics. Kinetics will be discussed in Section C.2. "The subject of rotational kinematics is somewhat mathematical in nature because it does not involve any forces associated with motion" [238]. The three mathematical approaches to identifying rotational motion are direction cosines, Euler angles, and quaternions.

C.1.1 Direction Cosines

The first mathematical method of describing rotational kinematics is direction cosines. In a rigid body there exists a body reference frame A. This frame consists of a right-hand set of three orthogonal unit vectors $\{\vec{a}_1, \vec{a}_2, \vec{a}_3\}$. Another reference frame B will contain a different set of three right-handed orthogonal unit vectors $\{\vec{b}_1, \vec{b}_2, \vec{b}_3\}$. The dot product law is used to describe one reference frame in terms of the other.

$$\vec{a} \cdot \vec{b} = |a||b| \cos \angle \vec{a}\vec{b} \quad (\text{C.1})$$

Using the dot product B can now be expressed in terms of A as follows:

$$\vec{b}_1 = C_{11}\vec{a}_1 + C_{12}\vec{a}_2 + C_{13}\vec{a}_3$$

$$\begin{aligned}
\vec{b}_2 &= C_{21}\vec{a}_1 + C_{22}\vec{a}_2 + C_{23}\vec{a}_3 \\
\vec{b}_3 &= C_{31}\vec{a}_1 + C_{32}\vec{a}_2 + C_{33}\vec{a}_3
\end{aligned} \tag{C.2}$$

where $C_{ij} \equiv \vec{b}_i \cdot \vec{a}_j$ is the cosine of the angle between \vec{b}_i and \vec{a}_j and C_{ij} is called the direction cosine.

An equivalent way of expressing the directional cosines is in matrix form.

$$\begin{pmatrix} \vec{b}_1 \\ \vec{b}_2 \\ \vec{b}_3 \end{pmatrix} = \begin{pmatrix} C_{11} & C_{12} & C_{13} \\ C_{21} & C_{22} & C_{23} \\ C_{31} & C_{32} & C_{33} \end{pmatrix} \begin{pmatrix} \vec{a}_1 \\ \vec{a}_2 \\ \vec{a}_3 \end{pmatrix} \tag{C.3}$$

The direction cosine matrix is also called the rotation matrix or the coordinate transformation matrix [2].

The kinematical equations of Poisson describe the functional relationships of the direction cosines and their rates [44].

$$\begin{aligned}
\dot{C}_{11} &= C_{12}\omega_3 - C_{13}\omega_2 \\
\dot{C}_{12} &= C_{13}\omega_1 - C_{11}\omega_3 \\
\dot{C}_{13} &= C_{11}\omega_2 - C_{12}\omega_1 \\
\dot{C}_{21} &= C_{22}\omega_3 - C_{23}\omega_2 \\
\dot{C}_{22} &= C_{23}\omega_1 - C_{21}\omega_3 \\
\dot{C}_{23} &= C_{21}\omega_2 - C_{22}\omega_1 \\
\dot{C}_{31} &= C_{32}\omega_3 - C_{33}\omega_2 \\
\dot{C}_{32} &= C_{33}\omega_1 - C_{31}\omega_3 \\
\dot{C}_{33} &= C_{31}\omega_2 - C_{32}\omega_1
\end{aligned} \tag{C.4}$$

The direction cosines are easy to calculate but do require integrating 9 equations to solve rotational kinematics. Also, the direction cosines are not intuitive since the values are not expressed as angles.

C.1.2 Euler Angles

A more intuitive way of looking at rotational kinematics is with Euler angles. These angles are easier to visualize than direction cosines. A perfect example of Euler angles is the yaw, pitch, and roll of an aircraft. Euler angles involve rotating about the three axes of the body as shown in Figure C.1.

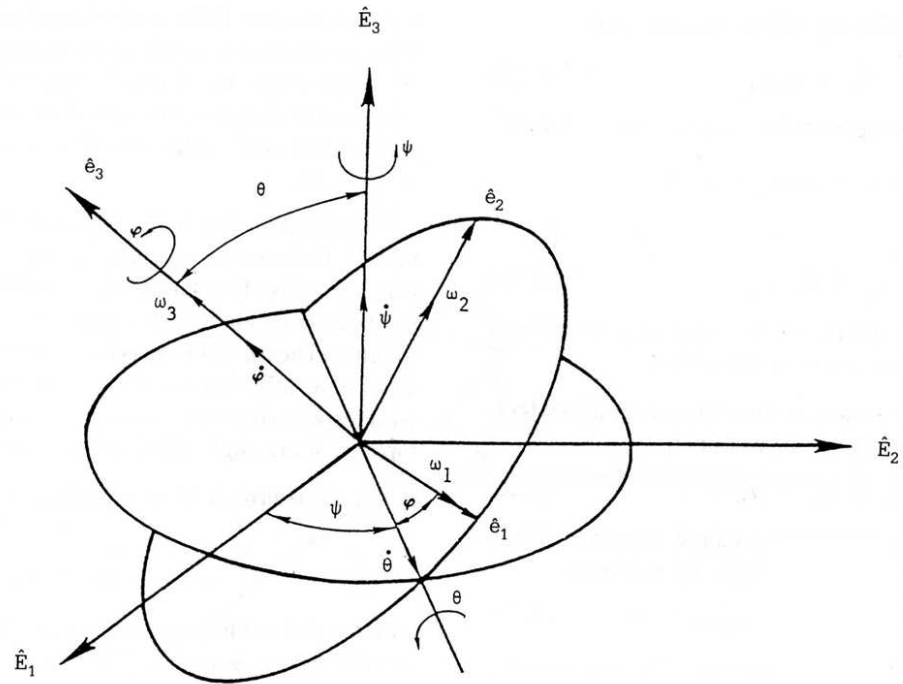


Figure C.1: Classical Euler rotations of a rigid body [44]

For each rotation about an axis, a rotational matrix is calculated. Consider a rotation of a body axis \hat{e} with respect to a reference frame \hat{E} as shown in Figure C.2. The components of \hat{E} along the \hat{e} directions are calculated as

$$\begin{aligned}
 \hat{e}_1 &= \hat{E}_1 \\
 \hat{e}_2 &= \hat{E}_2 \cos \theta_1 + \hat{E}_3 \sin \theta_1 \\
 \hat{e}_3 &= -\hat{E}_2 \sin \theta_1 + \hat{E}_3 \cos \theta_1
 \end{aligned} \tag{C.5}$$

or in matrix form as

$$\begin{pmatrix} \hat{e}_1 \\ \hat{e}_2 \\ \hat{e}_3 \end{pmatrix} = \begin{pmatrix} 1 & 0 & 0 \\ 0 & c\theta_1 & s\theta_1 \\ 0 & -s\theta_1 & c\theta_1 \end{pmatrix} \begin{pmatrix} \hat{E}_1 \\ \hat{E}_2 \\ \hat{E}_3 \end{pmatrix} \quad (\text{C.6})$$

where $c\theta$ and $s\theta$ represent $\cos \theta$ and $\sin \theta$.

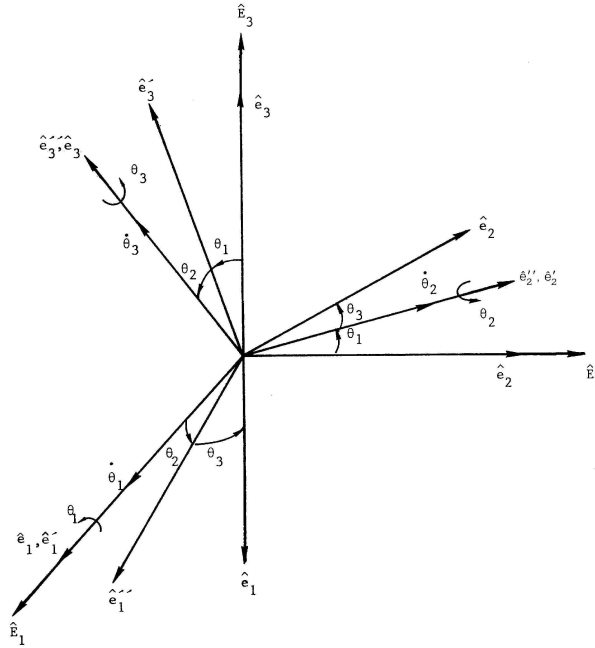


Figure C.2: Sequential orthogonal rotations of the \hat{e} reference frame about the \hat{E} reference frame [44]

A rotation about each axis can be represented as

$$\begin{pmatrix} \hat{e}'_1 \\ \hat{e}'_2 \\ \hat{e}'_3 \end{pmatrix} = R(\theta_1) \begin{pmatrix} \hat{E}_1 \\ \hat{E}_2 \\ \hat{E}_3 \end{pmatrix} \quad (\text{C.7})$$

$$\begin{pmatrix} \hat{e}''_1 \\ \hat{e}''_2 \\ \hat{e}''_3 \end{pmatrix} = R(\theta_2) \begin{pmatrix} \hat{e}'_1 \\ \hat{e}'_2 \\ \hat{e}'_3 \end{pmatrix} \quad (\text{C.8})$$

$$\begin{pmatrix} \hat{e}_1 \\ \hat{e}_2 \\ \hat{e}_3 \end{pmatrix} = R(\theta_3) \begin{pmatrix} \hat{e}_1'' \\ \hat{e}_2'' \\ \hat{e}_3'' \end{pmatrix} \quad (\text{C.9})$$

where

$$R(\theta_1) = \begin{pmatrix} 1 & 0 & 0 \\ 0 & c\theta_1 & s\theta_1 \\ 0 & -s\theta_1 & c\theta_1 \end{pmatrix} \quad (\text{C.10})$$

$$R(\theta_2) = \begin{pmatrix} c\theta_2 & 0 & -s\theta_2 \\ 0 & 1 & 0 \\ s\theta_2 & 0 & c\theta_2 \end{pmatrix} \quad (\text{C.11})$$

$$R(\theta_3) = \begin{pmatrix} c\theta_3 & s\theta_3 & 0 \\ -s\theta_3 & c\theta_3 & 0 \\ 0 & 0 & 1 \end{pmatrix} \quad (\text{C.12})$$

Referring again to Figure C.1, assume the body is undergoing a rotation first about the \hat{e}_1 axis followed by a rotation about \hat{e}_2 and then \hat{e}_3 . The body reference frame is expressed in terms of the fixed reference frame as follows:

$$\begin{pmatrix} \hat{e}_1 \\ \hat{e}_2 \\ \hat{e}_3 \end{pmatrix} = R(\theta_3)R(\theta_2)R(\theta_1) \begin{pmatrix} \hat{E}_1 \\ \hat{E}_2 \\ \hat{E}_3 \end{pmatrix} \quad (\text{C.13})$$

or

$$R_{123} = R(\theta_3)R(\theta_2)R(\theta_1)$$

$$= \begin{pmatrix} c\theta_2 c\theta_3 & c\theta_3 s\theta_1 s\theta_2 + c\theta_1 s\theta_3 & -c\theta_1 c\theta_3 s\theta_2 + s\theta_1 s\theta_3 \\ -c\theta_2 s\theta_3 & -s\theta_1 s\theta_2 s\theta_3 + c\theta_1 c\theta_3 & c\theta_1 s\theta_2 s\theta_3 + s\theta_1 c\theta_3 \\ s\theta_2 & -c\theta_2 s\theta_1 & c\theta_1 c\theta_2 \end{pmatrix} \quad (\text{C.14})$$

The angular velocities for this rotation sequence are

$$\begin{aligned} \omega_1 &= \dot{\theta} \cos \phi + \dot{\psi} \sin \theta \sin \phi \\ \omega_2 &= \dot{\psi} \sin \theta \cos \phi - \dot{\theta} \sin \phi \\ \omega_3 &= \dot{\phi} + \dot{\psi} \cos \theta \end{aligned} \quad (\text{C.15})$$

Solving for $\dot{\phi}$, $\dot{\theta}$, $\dot{\psi}$ yields

$$\begin{pmatrix} \dot{\psi} \\ \dot{\phi} \\ \dot{\theta} \end{pmatrix} = \frac{1}{\sin \theta} \begin{pmatrix} \sin \phi & \cos \phi & 0 \\ -\sin \phi \cos \theta & -\cos \phi \cos \theta & \sin \theta \\ \cos \phi \sin \theta & -\sin \phi \sin \theta & 0 \end{pmatrix} \begin{pmatrix} \omega_1 \\ \omega_2 \\ \omega_3 \end{pmatrix} \quad (\text{C.16})$$

These three equations appear easy to integrate but trigonometric functions require greater computational time than addition and multiplication. Although Euler angles have fewer equations to integrate than direction cosines, a larger amount of processing time is used to calculate the angular velocities. The only concern is the singularity in Eq. C.16 when θ equals 0° . For a gravity gradient stabilized satellite, this singularity becomes a concern. To avoid the singularity in pitch, a roll-pitch-yaw (1-3-2) rotation sequence is used. This rotation sequence yields

$$\begin{pmatrix} \dot{\psi} \\ \dot{\phi} \\ \dot{\theta} \end{pmatrix} = \frac{1}{\cos \theta} \begin{pmatrix} \cos \theta & -\cos \psi \sin \theta & \sin \psi \sin \theta \\ 0 & \cos \psi & -\sin \psi \\ 0 & \sin \psi \cos \theta & \cos \psi \cos \theta \end{pmatrix} \begin{pmatrix} \omega_1 \\ \omega_2 \\ \omega_3 \end{pmatrix} \quad (\text{C.17})$$

Now the singularity occurs when the pitch angle equals 90° and gravity gradient dynamics of the satellite will prevent this singularity from occurring.

C.1.3 Quaternions

The third mathematical approach to identifying rotational motion is using quaternions. Instead of the trigonometric functions of Euler angles, quaternions use algebraic relations. This provides quicker computations and also eliminates the possibility of a singularity appearing. An Euler axis, also known as a principal axis, is an axis that is fixed in the body frame and is stationary in the inertial frame. This axis is special because any combination of rigid body rotation is described as a single rotation about the Euler axis. The eigenaxis vector $\vec{e} = (e_1, e_2, e_3)$ is simply the direction cosines of the Euler axis relative to both the body and inertial reference frames.

The quaternions, Euler parameters, are then defined as

$$\begin{aligned} q_1 &= e_1 \sin(\theta/2) \\ q_2 &= e_2 \sin(\theta/2) \\ q_3 &= e_3 \sin(\theta/2) \\ q_4 &= \cos(\theta/2) \end{aligned} \tag{C.18}$$

where θ is the rotation angle about the Euler axis. After applying trigonometric identities the rotation matrix becomes

$$R = \begin{pmatrix} 1 - 2(q_2^2 + q_3^2) & 2(q_1q_2 + q_3q_4) & 2(q_1q_3 - q_2q_4) \\ 2(q_1q_2 - q_3q_4) & 1 - 2(q_1^2 + q_3^2) & 2(q_2q_3 + q_1q_4) \\ 2(q_1q_3 + q_2q_4) & 2(q_2q_3 - q_1q_4) & 1 - 2(q_1^2 + q_2^2) \end{pmatrix} \tag{C.19}$$

Substituting Eq. C.19 into Eqs. C.4 and solving for angular velocity we obtain

$$\begin{aligned} \omega_1 &= 2(\dot{q}_1q_4 + \dot{q}_2q_3 - \dot{q}_3q_2 - \dot{q}_4q_1) \\ \omega_2 &= 2(\dot{q}_2q_4 + \dot{q}_3q_1 - \dot{q}_1q_3 - \dot{q}_4q_2) \\ \omega_3 &= 2(\dot{q}_3q_4 + \dot{q}_1q_2 - \dot{q}_2q_1 - \dot{q}_4q_3) \end{aligned} \tag{C.20}$$

Applying a constraint equation such that

$$q_1^2 + q_2^2 + q_3^2 + q_4^2 = 1 \quad (\text{C.21})$$

and differentiating it

$$0 = 2(\dot{q}_1 q_1 + \dot{q}_2 q_2 + \dot{q}_3 q_3 + \dot{q}_4 q_4) \quad (\text{C.22})$$

We can now combine Eqs. C.20 and Eq. C.22 into matrix form as follows:

$$\begin{pmatrix} \omega_1 \\ \omega_2 \\ \omega_3 \\ 0 \end{pmatrix} = 2 \begin{pmatrix} q_4 & q_3 & -q_2 & -q_1 \\ -q_3 & q_4 & q_1 & -q_2 \\ q_2 & -q_1 & q_4 & -q_3 \\ q_1 & q_2 & q_3 & q_4 \end{pmatrix} \begin{pmatrix} \dot{q}_1 \\ \dot{q}_2 \\ \dot{q}_3 \\ \dot{q}_4 \end{pmatrix} \quad (\text{C.23})$$

Rearranging Eq. C.23 results in the kinematic differential equations for quaternions as

$$\begin{pmatrix} \dot{q}_1 \\ \dot{q}_2 \\ \dot{q}_3 \\ \dot{q}_4 \end{pmatrix} = \frac{1}{2} \begin{pmatrix} q_4 & -q_3 & q_2 & q_1 \\ q_3 & q_4 & -q_1 & q_2 \\ -q_2 & q_1 & q_4 & q_3 \\ -q_1 & -q_2 & -q_3 & q_4 \end{pmatrix} \begin{pmatrix} \omega_1 \\ \omega_2 \\ \omega_3 \\ 0 \end{pmatrix} \quad (\text{C.24})$$

or

$$\begin{pmatrix} \dot{q}_1 \\ \dot{q}_2 \\ \dot{q}_3 \\ \dot{q}_4 \end{pmatrix} = \frac{1}{2} \begin{pmatrix} 0 & \omega_3 & -\omega_2 & \omega_1 \\ -\omega_3 & 0 & \omega_1 & \omega_2 \\ \omega_2 & -\omega_1 & 0 & \omega_3 \\ -\omega_1 & -\omega_2 & -\omega_3 & 0 \end{pmatrix} \begin{pmatrix} q_1 \\ q_2 \\ q_3 \\ q_4 \end{pmatrix} \quad (\text{C.25})$$

As a result of the fewer number of equations to integrate compared to direction cosines, and the absence of singularities and trigonometric functions, modern spacecraft orientation is now commonly described in terms of quaternions [238].

C.2 Rigid Body Dynamics

Kinematic differential equations are useful for integrating the motion of a satellite. An understanding of kinetics is required to study how this satellite reacts to forces acting

upon it. This section will first discuss the properties of angular momentum, moments of inertia, and how moments will affect the equations of motion. The section concludes with a discussion on stability requirements for both linear and nonlinear systems.

C.2.1 Kinetics

Just as a moving body has translational momentum comprised of its velocity and mass, a rotating body will also have rotational momentum. This rotational momentum is referred to as angular momentum. Similar to its counterpart, angular momentum is comprised of angular velocity, ω , and inertia, I . Thus the total angular momentum is expressed as

$$\vec{H} = I\vec{\omega} \quad (\text{C.26})$$

Both \vec{H} and $\vec{\omega}$ are 3×1 vectors so I is a 3×3 matrix known as the inertia matrix.

A rigid body does not necessarily have to possess uniform density distribution. It's density can vary with position relative to the system's center of mass. The moment of inertia matrix contains all of the information of the mass distribution within a rigid body [240].

$$I = \begin{pmatrix} \int (y^2 + z^2)dm & - \int xydm & - \int xzdm \\ - \int xydm & \int (x^2 + z^2)dm & - \int yzdm \\ - \int xzdm & - \int yzdm & \int (x^2 + y^2)dm \end{pmatrix} \quad (\text{C.27})$$

This inertia matrix only needs to be recalculated if the mass distribution alters from its original configuration.

The kinetic relation between moments and angular momentum is

$$M = \dot{H} \quad (\text{C.28})$$

Using a body fixed reference frame Eq. C.28 becomes

$$M = \frac{d}{dt}H + \omega \times H \quad (\text{C.29})$$

Applying the matrix form of the cross product yields

$$M = I\dot{\omega} + \omega^x I \omega \quad (\text{C.30})$$

where ω^x is a scew-symmetric matrix of the form

$$\omega^x = \begin{pmatrix} 0 & -\omega_3 & \omega_2 \\ \omega_3 & 0 & -\omega_1 \\ -\omega_2 & \omega_1 & 0 \end{pmatrix} \quad (\text{C.31})$$

To further simplify the equations of motion, assume a principal axis frame. The inertia matrix becomes a diagonal matrix

$$J = \begin{pmatrix} J_1 & 0 & 0 \\ 0 & J_2 & 0 \\ 0 & 0 & J_3 \end{pmatrix} \quad (\text{C.32})$$

and Eq. C.30 becomes

$$\begin{pmatrix} M_1 \\ M_2 \\ M_3 \end{pmatrix} = \begin{pmatrix} J_1 & 0 & 0 \\ 0 & J_2 & 0 \\ 0 & 0 & J_3 \end{pmatrix} \begin{pmatrix} \dot{\omega}_1 \\ \dot{\omega}_2 \\ \dot{\omega}_3 \end{pmatrix} + \begin{pmatrix} 0 & -\omega_3 & \omega_2 \\ \omega_3 & 0 & -\omega_1 \\ -\omega_2 & \omega_1 & 0 \end{pmatrix} \begin{pmatrix} J_1 & 0 & 0 \\ 0 & J_2 & 0 \\ 0 & 0 & J_3 \end{pmatrix} \begin{pmatrix} \omega_1 \\ \omega_2 \\ \omega_3 \end{pmatrix} \quad (\text{C.33})$$

which reduces to Euler's rotational equations of motion for a rigid body.

$$\begin{aligned} M_1 &= J_1 \dot{\omega}_1 - (J_2 - J_3) \omega_2 \omega_3 \\ M_2 &= J_2 \dot{\omega}_2 - (J_3 - J_1) \omega_1 \omega_3 \\ M_3 &= J_3 \dot{\omega}_3 - (J_1 - J_2) \omega_1 \omega_2 \end{aligned} \quad (\text{C.34})$$

These three equations are coupled, nonlinear ordinary differential equations. The rotational motion of a rigid body can be completely described when Euler's rotational equations of motion are combined with the kinematic differential equations from Section C.1.

C.2.2 Stability

Stability is a major concern with satellite control theory. An unstable satellite may drift away from its operational orbital path, disrupt communications, or waste excessive fuel and reduce its mission effectiveness. An object near an equilibrium point is considered stable when small disturbances result in small changes. To understand stability about an equilibrium point consider a pendulum. Two equilibrium points exist. One point occurs when the pendulum is pointing straight down and the other point when the pendulum is pointing straight up. At both equilibrium points the pendulum will remain motionless if no external forces are applied. However, only one of these points are stable. A small disturbance applied to the pendulum while pointing down will cause it to oscillate slightly about its equilibrium point. This configuration is considered stable. A small disturbance applied to the pendulum while it is pointing up will cause a large change in its orientation. This point is unstable.

Current theory supports two concepts of stability. The first concept deals with Lagrange stability. Lagrange stability applies when small disturbances result in bounded changes. Liapunov stability occurs when an object resting at an equilibrium point experiences small disturbances and only small changes are detected. Now consider the pendulum example previously mentioned. When the pendulum is pointing downward it is considered to be both Liapunov and Lagrange stable. When the pendulum is pointing straight up, any small change will result in a drastic change in location. Thus, this point is Liapunov unstable. But the angle of the pendulum is bounded (i.e. it may oscillate slightly about the equilibrium position) so the system is considered Lagrange stable. From this it is apparent that a Liapunov stable system is also Lagrange stable but a Lagrange stable system is not necessarily Liapunov stable.

To test if a linear system is considered stable a concept from control theory is applied. "A linear system is said to be stable if and only if the roots of its characteristic

equation have negative real parts" [44]. This is the same as saying that the real part of the eigenvalues of the system are only negative. A zero root is considered asymptotically unstable. A system is asymptotically stable if changes from an equilibrium point result in returning to the same equilibrium point.

Liapunov developed two theorems to determine if a nonlinear system is stable. The first theorem states that a nonlinear system is asymptotically stable in a region near an equilibrium point if and only if its linearized approximation is asymptotically stable. The second theorem states if a positive definite function can be found such that its derivative is negative definite the nonlinear system is stable [2]. This function is often referred to as the Liapunov function. For a more indepth discussion of stability and methods to determining a Liapunov function refer to [44], pages 113-126.

Appendix D

FalconSAT-3

At the same time CTD was conducting tests on the CoilAble boom, the United States Air Force Academy (USAFA) was beginning the design phase for their fourth satellite, FalconSAT-3. The Academy's Space Systems Research Center (SSRC) supports the Department of Defense (DoD) Defense Planning Guide mandate to "establish and sustain a cadre of space professionals" by providing an opportunity for AFA cadets to "learn space by doing space" within a safe, supervised environment. This allows the cadets to gain real-world, practical experience working with small satellite and launch systems. Students in the fields of astronautics, physics, math, computer science, and management are supervised by members of AFA faculty and contractor support in the research areas of systems engineering, sounding rocket systems, and micro/nanosat systems.

The FalconSAT-3 spacecraft is a 0.46m cube weighing approximately 50 kg. A solid model drawing of the current spacecraft is shown in Figure D.1. The spacecraft is manifested for launch aboard an Atlas V Evolved Expendable Launch Vehicle (EELV) in October, 2006[207]. While deployed at an altitude of 560km and an inclination of 35.4°, the spacecraft is designed to provide an on-orbit platform that supports three DoD experiments: the Flat Plasma Spectrometer (FLAPS), the Plasma Local Anomalous Noise Environment (PLANE), and the Micro Propulsion Attitude Control System (MPACS).

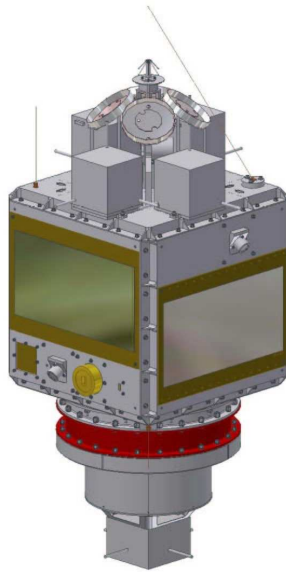


Figure D.1: A Solid Model Drawing of FalconSAT-3

The objective of the FLAPS experiment is to characterize the effects of non-Maxwellian charged particle distributions on formation, propagation, and decay of ionospheric plasma bubbles[208]. Successful completion of this objective will support the validation of the plasma bubble and radio wave scintillation nowcasting and forecasting system associated with DoD's Communication/Navigation Outage Forecasting System (C/NOFS). The FLAPS experiment will make fine resolution (10%) measurements of ionospheric plasma spectra differential in energy and angle and could support simultaneous multi-point in situ measurements of a single plasma bubble structure with another satellite. FLAPS requires FalconSAT-3 to provide $\pm 5^\circ$ attitude control in the ram direction (2-axis) with attitude knowledge of $\pm 1^\circ$ for post processing of the data.

The PLANE experiment's objective is to characterize the plasma turbulence in the space environment surrounding a satellite[209]. PLANE is designed to distinguish the turbulence in the ambient environment (global effects) from variations in the plasma population co-moving with the satellite (local effects). PLANE is also capable of quantifying plasma perturbations caused by active systems on the satellite, such as a firing propulsion system. The experiment does not require state vector data for real time operations. However, data post processing requirements call for $\pm 20^\circ$ pointing in the ram direction (2-axis), a rate of change in the pitch and yaw axis of less than 2 deg/sec, and attitude knowledge of $\pm 3^\circ$.

The MPACS thruster is based on the micro pulsed plasma thruster (mPPT) developed at Air Force Research Lab's Propulsion Directorate over the last several years[210]. A three-electrode version of the mPPT was developed by Busek for advanced engineering development on the FalconSAT-3 flight (see Figure D.2). Flight heritage of the Micro Propulsion Attitude Control System (MPACS) thruster is to be established on FalconSAT-3 in the hopes of demonstrating that the thruster can be used as an effective actuator as part of a microsatellite ADCS[211]. The experiment's objective is to operate MPACS as part of the FalconSAT-3 ADCS for 100 cumulative hours. Data

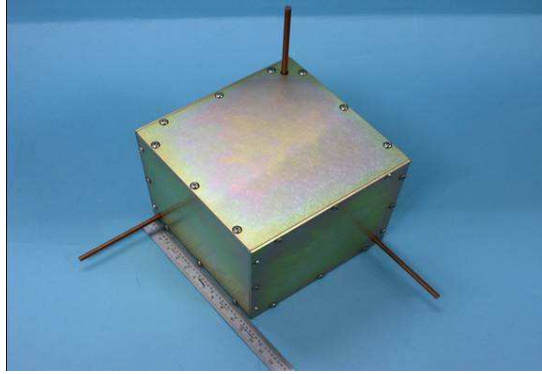


Figure D.2: 3-Axis MPACS Cluster

concerning the beginning and end of life performance characteristics, as well as detection of any adverse operational interactions between MPACS and the satellite, need to be quantified. To demonstrate attitude stabilization functions, four 3-axis clusters are mounted on the nadir plate of the satellite (Figure D.3) and one 2-axis cluster is placed on the tip mass of the gravity gradient boom (Figure D.4)[205].

The attitude determination requirements imposed by the MPACS experiment are nebulous at best. The calculated moments of inertia of FalconSAT-3 with an operationally deployed boom are shown in Table D.1. The FalconSAT-3 ADCS design team are conducting simulation efforts to determine the impact the approximately $100 \mu/N$ of thrust produced by MPACS will have on effectively controlling the satellite.

FalconSAT-3 is the USAFA's first attempt at designing a 3-axis stabilized and controlled spacecraft. Aware of the power and volume limitations inherent with small satellites, the ADCS team is utilizing both active and passive actuators in the design. Attitude sensors on the spacecraft consist of four Space Quest model SS-256 (2-axis) sun sensors and one Billingsley TFM100G2 Fluxgate Magnetometer. Three Space Quest magnatorque rods (5.0 Am^2) provide active control while CTD is developing an EMC gravity gradient boom for passive control. The EMC longerons will be both the primary deployment mechanism and the principal structural members of the boom. Al-

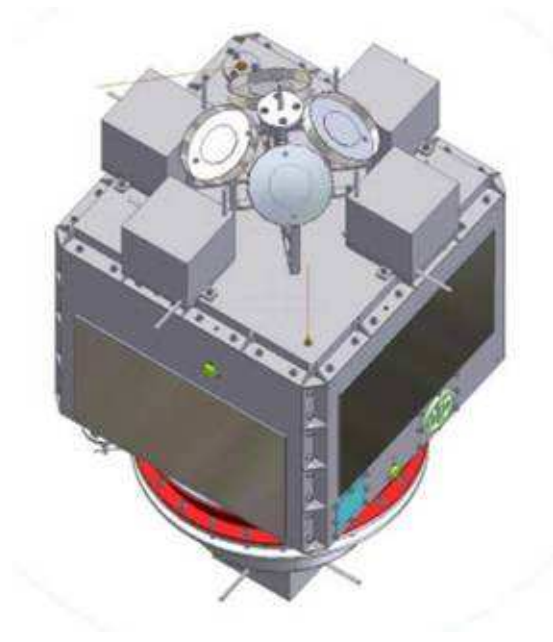


Figure D.3: Four MPACS Clusters on the Nadir Plate of FalconSAT-3



Figure D.4: A 2-Axis MPACS Cluster Attached to the EMC Boom

Table D.1: Moments of Inertia with Deployed Boom Configuration

MOI	kg-m ²	lbm-in ²	lbf-ft-s ²	lbf-in-s ²
I_{xx}	67.40	23.0E4	49.72	596.60
I_{yy}	67.45	23.1E4	49.74	596.98
I_{zz}	1.31	4.468E3	0.96	11.57

though the application of composite materials has the potential to reduce weight and improve performance, the cost is experiencing increased deflection and vibration within the structure[241]. With the flexible characteristics of the boom (1.5 Hz bending frequency and 1.7 Hz torsional frequency) there is great concern of the impact this flexible structure will have on the control of a small satellite.